Universidad Nacional Autónoma de México

Posgrado en Ciencias Físicas

EFECTOS DE LA ESTRUCTURA DE LA ATMÓSFERA EN LA DETECCIÓN DESDE EL ESPACIO DE CHUBASCOS ATMOSFÉRICOS ORIGINADOS POR RAYOS CÓSMICOS DE ENERGÍAS EXTREMAS

T E S I S

QUE PARA OBTENER EL TÍTULO DE:
MAESTRO EN CIENCIAS (FÍSICA)
PRESENTA:

ALEJANDRO DANIEL GUZMÁN CABRERA

DIRECTOR DE TESIS: DR. GUSTAVO ADOLFO MEDINA-TANCO

MIEMBRO DEL COMITÉ TUTORAL: DR. JOSÉ FRANCISO VALDÉS GALICIA
MIEMBRO DEL COMITÉ TUTORAL: DR. JUAN CARLOS D'OLIVO SAEZ

México, D.F.

2011

Contents

Resumen en castellano **ix**

Summary **1**

1 Introduction **3**
1.1 State of the Art . . . 3
1.1.1 Cosmic rays . . . 3
1.1.2 Acceleration and propagation of cosmic rays . . . 5
1.1.3 Extensive Air Showers(EAS) . . . 9
1.1.4 Shower Simulations . . . 10
1.2 JEM-EUSO . . . 14
1.2.1 Mission overview & Observation principle . . . 14
1.2.2 Scientific objectives . . . 16
1.2.3 Optics and Focal Surface subsystems . . . 20
1.2.4 Atmospheric Monitoring Subsystem . . . 22

2 Space borne EECR experiments: Challenges in EAS observation. **27**
2.1 Present work's motivation and main objectives . . . 27
2.1.1 Cloud studies . . . 28

3 Atmospheric features relevant to EAS's detection from space **31**
3.1 The Atmosphere . . . 31
3.1.1 Composition . . . 31
3.1.2 Aerosols . . . 36
3.1.3 Scattering . . . 38
3.1.4 UV phenomena . . . 40
3.2 Satellite data . . . 43
3.2.1 MERIS . . . 43
3.2.2 CALIPSO . . . 50

4 Earth's cloud coverage and its implications in exposure. **57**
4.1 Statistical studies . . . 60
4.1.1 Cloud coverage effect in different scenarios . . . 60
4.1.2 Clouds' τ distribution . . . 62
4.1.3 Hadron and photon discrimination. . . . 65

5 Clouds' vertical structure and its effects over EAS reconstruction **67**
5.1 False-positive & false-negative detection simulation. 67
5.2 Cloud attenuation of the EAS. 70
5.3 Thin Clouds & and altitudes uncertainties of τ determination. 75

6 Contributions to the JEM-EUSO mission **81**
6.1 CALIPSO data analysis and mission requirements constrains 81

7 Outlook and Conclusions **87**
7.1 Cloud effects in novel space born experiments 87
7.2 Main results in the JEM-EUSO mission's framework 88

A CALIPSO's Lidar Cloud Profile Record **89**

B HDF and CALIPSO data **91**

C Header Files in C++ **93**
C.1 Line of sight determination 93
C.2 Tau calculations 96

Bibliography **98**

List of Figures

1.1 The spectrum of Cosmic Rays. EECR reside at the highest energy of this enormous spectrum.[Biermann & Sigl 2001] 4
1.2 Magnetic Field and size of some possible accelerating sites. Diagonal lines correspond to Fe nuclei at 10^{20}eV (green) and protons at 10^{20}eV and 10^{21}eV (red dashed and solid lines) from equation 1.2. All objects below aforesaid lines are cannot accelerate these particles to such energies. (rec. [Supanitsky 2007] 6
1.3 Attenuation lengths of proton, iron, and gamma-ray primaries due to interactions with the cosmic radiation background.[Nagano & Watson 2000] 8
1.4 Energy spectra of EECRs observed by Auger [Pierre Auger Collaboration 2008], HiRes [HiRes 2004], AGASA [Yoshida et al. 1995] and Telescoper Array [Telescope Array 2009]. The energy scale is shifted by +17% for Auger, and by –17% for AGASA . The vertical axis is multiplied by E^3 to enhance the structure of the spectrum. 8
1.5 Schematic view of an EAS. At ground level the electromagnetic component is the most abundant, followed by the muonic component. [Supanitsky 2007] 10
1.6 Energy deposition as a function of slant depth for a typical shower simulated using CONEX. Energy is 10^{20}eV and zenith angle is 60° 14
1.7 Artistic depiction of JEM-EUSO's operational principle. UV light produced by the EAS, originated by the extreme energy particle, is captured from space, allowing an unprecedented instantaneous exposure. 15
1.8 Artistic comparison of both "normal" and "tilted" modes, instantaneous areas. . . . 16
1.9 Deflection scenario for protons at energies of $10^{20}eV$. Blue dots are "circular " regions of 2.5° diameter, where protons entered the galactic Halo. The red dots represent the perceived direction of arrival of such regions afeter being deflected through the galactic magnetic field.(rec. [Medina-Tanco 2009] 17
1.10 Anisotropy seen by Auger. [PAO Anisotropy 2007] 18
1.11 Schematic view of EAS initiated by extreme energy neutrinos. Neutrinos at $\sim 10^{20}$ eV deeply penetrates the atmosphere and may initiate EAS near the surface of the Earth. 19
1.12 (a) Schematic view of cosmogenic neutrino production as a result of the GZK mechanism. (b)Heavier nuclei can also produce neutrinos. Both processes leave their particular imprint in the neutrino background. 20
1.13 Focal surface detector and its structure. [JEM-EUSO Collaboration] 21
1.14 Artistic depiction of JEMEUSO summarizing the optics and focal surface layout. . 22
1.15 Atmospheric monitoring subsystem. 23

3.1 Temperature profile of the Standard atmosphere (modified from [Ahrens 2000]). . . . 32
3.2 Pressure dependence of the profile of the Standard Atmosphere (modified from [Ahrens 2000]). . . . 33
3.3 Atmospheric absorption of the electromagnetic spectrum. . . . 36
3.4 CALIPSO measurements of avearage aerosol optical depth in the visible/infrared in the cloud-free conditions in December-January-Ferbruary 2007 (left) and June-July-August 2007 (right). From [Hongbin et al. 2010]. . . . 37
3.5 Usual cloud classification. From [ISCCP]. . . . 37
3.6 Fluorescence spectra of air in the UV region. Atmospheric transmission is shown as a dashed line. Modified from [Bunner 1967] . . . 40
3.7 Examples of UV intensity recorded at night side of the Earth by TATIANA satellite. Peaks occur when the satellite crosses Mexico City (α) and Houston (β) and Los Angeles (γ) in the bottom panel (from [Garipov 2005]). . . . 40
3.8 Transient Luminous Events. . . . 42
3.9 MERIS measuring window in the electro magnetic spectrum. Emission lines for some atmospheric and organic components are shown . . . 44
3.10 MERIS's spectral bands ($\Delta\lambda < 10nm$). . . . 44
3.11 MERIS coverage of 1 complete day acquired data. . . . 45
3.12 Depiction of MERIS observation principle. . . . 46
3.13 Depiction of MERIS data flow. . . . 48
3.14 Illustration of the principle of the cloud top pressure detection using absorption of solar radiation due to well mixed atmospheric gases. Ancillary data (theoretical and measured) are then used in combination to estimate cloud's top height. . . . 49
3.15 Artist conception of CALIPSO's measurements while flying along the *Afternoon train*. 50
3.16 CALIPSO's ground tracks from one whole day of data acquisition. . . . 51
3.17 CALIOP measuring principle. The time domain backscattered signal is transformed into atmospheric features with distinct vertical structure. . . . 52
3.18 Lidar Level 2 Cloud Profile data product structure . . . 54
3.19 Production Pathway for Level 2 Cloud Profile data products. . . . 55

4.1 Orbital elements illustration. (modified from [Bruening]) . . . 58
4.2 Latitude distribution of the ISS ($\frac{\Delta lat}{\Delta t}$). . . . 59
4.3 Histograms for X_max of our simulated showers. Protons are shown in red and gammas in blue. . . . 60
4.4 A JEM-EUSO's FoV superposed over a "cloudy portion" MERIS data near Papua New Guinea in the south Pacific ocean. In contrast there are almost no clouds outside the FoV for this example. . . . 61
4.5 Fraction of lost events due to the presence of clouds . . . 62
4.6 Earth coverage of clouds with different values of τ and their respective heights a.s.l in [km] . . . 63
4.7 One of the many test carried out to establish a more clear connection between cloud temperature and optical thickness. Although no clear relationship can be inferred for this 2 variables, this kind of information would help fill in the "look up" tables needed for a a correct interpretation of the infrared camera data. . . . 64
4.8 Aitoff projection of the sky . Color code indicates the value of X_{max} for γ-showers injected with an spectral index of 2.7. . . . 64

4.9 Aitoff projection of the sky . Color code indicates the probability to discern between a hadron initiated shower and a photon initiated shower. 65

5.1 Depiction of the false positive false negative tests. 68
5.2 False positive false negative studies for different uncertainties (see text). 69
5.3 Depiction of our insertion of different showers inside CALIPSO's *curtain files.* . . . 70
5.4 Depiction of τ calculation for different lines of sight. The cell color ilustrates the expected value of $\alpha(\vec{x})$. Purple trace represents the EAS. 71
5.5 A "zoom out" of the example called the cloudy region(This "zoom out" can accommodate 2 FoV) 73
5.6 Example "cloudy" region and its effects in shower reconstrucion. Black lines represent the expected unattenuated signal. Blue lines represent the actual detected signal, and green lines represent the value of τ integrated along the line of sight. 74
5.7 Uncertainty in the spatial determination of the extinction coefficent for a sample region. 75
5.8 Example region fulfilling our *thin cloud region* criteria 76
5.9 Example of the effect of shifting the values of $\alpha(\vec{x})$ in the number of photons arriving at JEM-EUSO's pupil, for a shower with $\theta = 75°$ and log(E/eV)=20, in a *thin cloud* region. 77
5.10 Reconstructed values of X_{max} for different cloud conditions(see text) 78
5.11 Amount of photons arriving at the detector's pupil (normalized to clear-sky condition) for different cloud conditions(see text) 79

6.1 Illustration of the 2 different modes for operating the lidar. In mode 1 the lidar probing points are kept the same inside the FoV regardless of the EAS. 82
6.2 Autocorrelation of cloud's optical thickness as a function of distance, calculated upwardly from the ground upto different altitudes. 82
6.3 Depiction of the attitude uncertainty problem. The precision of actual line of sight of the lidar measurement is expected to have an error of $\pm 1.5°$. 83
6.4 Scattered plot of $\Delta\tau$ vs the actual viewing angle, for no tilting and tilting angle of 40°. 83
6.5 Scattered plot of $\tau_{detected}$ vs τ_{real}, for no tilting and tilting angle of 40°. As it can be seen the tilted phase of the JEM-EUSO mission will increase the false positive scenario (see chapter 5). 84
6.6 Distribution of $\Delta\tau$ in (logarithmic scale) for no tilting and tilting angle of 40°. . . . 85

Resumen en castellano

Desde su descubrimiento a principios del siglo XX, la radiación ionizante proveniente del espacio exterior o rayos cósmicos como los bautizó Millikan en 1925, ha fascinado la mente de los científicos. El furor por entender la totalidad de las partículas más elementales demostró ser un campo fructífero en la Física, el cual hoy en día gracias a la maduración de técnicas experimentales en el proceso de detección, está expandiendo su campo "natural" de estudio al entrar en el reino de la astrofísica. Mientras algunas de las energías de este tipo de radiación pueden ser entendidas e inclusive reproducidas en los aceleradores más poderosos de hoy en día, las energías más altas (p.ej. 10^{20}eV) de rayos cósmicos aún asombran y confunden a los físicos. Por un lado, infundir a partículas elementales tales energías simplemente está fuera de las capacidades de la tecnología humana actual.Por otro lado, no es claro que tipo de procesos naturales pueden acelerar a partículas de este modo. Por ende los rayos cósmicos con energías en el exceso de $10^{19}eV$ han sido apropiadamente llamados Rayos Cósmicos Extremadamente Energéticos (EECR por sus siglas en inglés *Extreme Energy Cosmic Rays*) .

La física de las astropartículas es un campo nuevo e interesante, disponible principalmente por el hecho de que los ECCR de hecho son partículas masivas provenientes de otras regiones del universo, que debido a sus energías extremas, sufren desviaciones casi despreciables en su trayectoria. Este "canal de partículas" de la astronomía no está disponible para energías menores debido a la propagación dispersiva de las partículas cargadas en campos magnéticos galácticos e intergalácticos. Sin embargo, una nueva complicación aparece mientras uno incrementa la energía de las partículas: el flujo disminuye como ley de potencia con un índice ~ 2.7. De este modo las energías por debajo de 10^{18}eV, se vuelven extremadamente difíciles de observar experimentalmente. Con el advenimiento de futuros experimentos situados en el espacio, tales como el Extreme Universe Space Observatory on Japanese Experiment Module (JEM-EUSO), este último contratiempo es superado a través del uso de enormes porciones de la atmósfera como detector. Por primera vez en la historia, científicos serán capaces de estudiar más a detalle el fenómeno del EECR con las estadísticas más altas jamás alcanzadas. El principio de observación de misiones

espaciales como JEM-EUSO es la llamada técnica de "fluorescencia". A medida que el EECR entra a la atmósfera, desencadena lo que es conocido como Chubasco Aéreo Extensivo (Extensive Air Shower, EAS). Este EAS consiste en un gran número de partículas secundarias, creadas como consecuencia de las interacciones del EECR con la atmósfera superior. Estas partículas secundarias producen luz fluorescente al ir depositando energía en las moléculas atmosféricas. Esta luz fluorescente es emitida isotrópicamente y por lo tanto aumenta las probabilidades de detectarlas. A cambio de esta ventaja, muchas complicaciones surgen como consecuencia de la utilización de grandes porciones de la atmósfera debido a sus inherentes inhomogeneidades . Cualquier detector espacial de EAS debe combinar las técnicas de detección de luz de fluorescencia con una monitorización precisa de las condiciones atmosféricas. Esto debe llevarse a cabo, inclusive durante el desarrollo individual de cada EAS. Esta meticulosa monitorización de las condiciones atmosféricas es la clave para una medición precisa de las propiedades de EECR, tales como energía o dirección de arribo. En el presente trabajo enfocamos nuestra atención en la estructura de las nubes y su influencia directa en muchos parámetros de crucial importancia para una misión como JEM-EUSO. Distinguimos y dirigimos nuestra atención principalmente en tres diferentes aspectos de la estructura de las nubes concernientes a la observación de EAS desde el espacio:

- Exposición y modificaciones del ciclo de trabajo debidas a la cobertura de las nubes.
- Efectos de reconstrucción debidos a diferentes factores de atenuación como consecuencia de la presencia de nubes a lo largo del seguimiento atmosférico de los chubascos.
- Incertidumbres en la línea de visión, y sus implicaciones en la correcta evaluación de propiedades ópticas de las nubes.

Finalmente verificamos algunas de las restricciones actuales de diseño y los requerimientos de JEM-EUSO, bajo la luz de esto nuevos estudios.

Summary

Since their discovery in the early twentieth century, the ionizing radiation that came from outer space, or *cosmic rays* as baptized by Millikan in 1925, has been fascinated the minds of scientists. The rush to understand the utter most elementary particles proved to be a fruitful ground in physics and nowadays, thanks to the maturing of experimental techniques in the detection process, it is expanding its "natural" field of study by entering the astrophysics realm. Whilst some of this radiation's energies can be understood and even reproduced in today's most powerful particle accelerators, the highest measured energies (i.e. $\sim 10^{20}$eV) of cosmic rays still amaze and puzzle physicists. It is simply beyond current capabilities of mankind's technology to infuse elementary particles with such energies. Therefore cosmic rays with energies in the excess of 10^{19}eV have been properly named *Extreme Energy Cosmic Rays (EECR).*

Astroparticle physics is a new and interesting field , available mainly because of the fact that EECR are actually massive particles incoming from other regions of the Universe which suffer almost negligible deviations in their path, due to their extreme energies.Therefore this "particle channel" of astronomy is not available for lower energies, due to the dispersive propagation of charged particles in the galactic and intergalactic magnetic fields, . But a mayor complication arises as one increases the energy of the particle: the flux decreases as a power law with index ~ 2.7. Thus for energies above 10^{18}eV the flux decreases dramatically to the order of one particle per square kilometer per century. With the forthcoming of space borne experiments, such as the Extreme Universe Space Observatory on Japanese Experiment Module **(JEM-EUSO)**, this last setback will be overturned by using huge portions of the atmosphere as a detector. For the first time in history scientists will be able to study in more detail this EECR phenomena with the highest statistics ever achievable.

JEM-EUSO's principle of observation is the so called "fluorescence" technique. As an EECR enters the atmosphere it triggers what is known as Extensive Air Shower (EAS). This EAS consists of a myriad of secondary particles created by the inter-

action of the EECR with the upper atmosphere. This secondary particles produce fluorescent light as they deposit their energy within the atmospheric molecules. This fluorescent light is emitted isotropically hence improving the probabilities of detecting it, but many complications arise as a consequence of using large portions of the atmosphere, because of these portions' inherent inhomogeneous properties. Any space borne EAS fluorescence detector shall combine the EAS detection techniques with an accurate monitoring of the atmospheric conditions throughout each individual EAS's development. This thorough monitoring of the atmospheric conditions is key to an accurate measurement of the EECR properties, such as, energy or arrival direction.

In the present work we focus our attention in the structure of clouds, and its direct influence on many parameters of crucial importance for a mission such as JEM-EUSO.

We distinguish and focus our attention on mainly three different aspects of cloud structure regarding EAS observation from space:

- Exposure and duty cycle modifications due to cloud coverage.
- Reconstruction effects due to different attenuation factors as a consequence of cloud presence along the EAS atmospheric track.
- Uncertainties in the line of sight, and their implications in cloud optical properties correct assessment.

Finally we verify some of the current design constrains and requirements of JEM-EUSO, under the light of this new studies.

Chapter 1

Introduction

1.1 State of the Art

1.1.1 Cosmic rays

Cosmic rays were first accounted for as a "radiation of great penetrating power" by Victor Hess and Werner Kohlhörster [Hess 1912] [Kohlhörster 1913] in the early 1900's. This pioneering work was followed by Bruno Rossi's and Pierre Auger's experiments in the end of 1930's [Auger 1939]. These researchers concluded that extensive particle showers were generated by high energy primary particles that interact with air molecules high in the atmosphere, yielding showers of electrons, photons, and muons that reach ground level through a series of subsequent processes.

Much more is known about cosmic rays nowadays. They consist mainly of nuclei with a large kinetic energy [Biermann & Sigl 2001]. As can be seen in figure 1.1, the flux of cosmic rays, expressed as the differential intensity expands for more than 11 orders of magnitude in energy, and for the most of this huge interval it can be fitted quite nicely with a power law (Eq 1.1), with an index $\alpha \approx 2.7$:

$$\frac{\mathrm{d}N}{\mathrm{d}E} \propto E^{-\alpha} \tag{1.1}$$

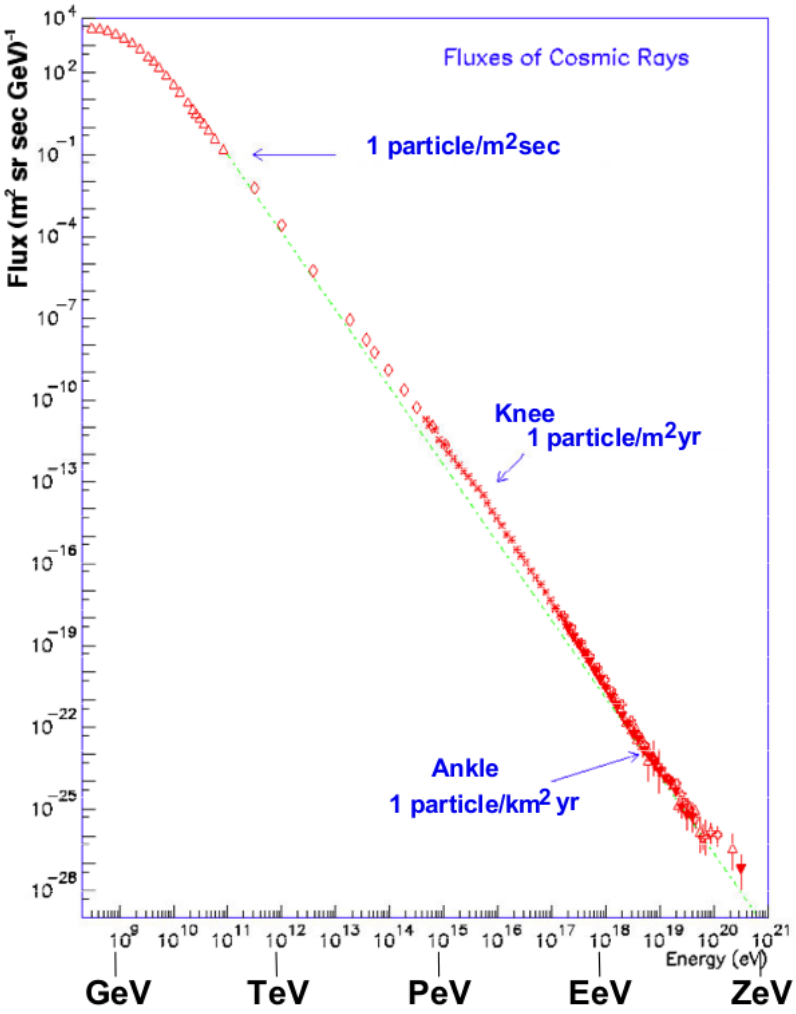

Figure 1.1: The spectrum of Cosmic Rays. EECR reside at the highest energy of this enormous spectrum.[Biermann & Sigl 2001]

Nevertheless the cosmic ray spectrum exhibits some explicit features that deviate from this overall behavior. A general picture can be sketched as follows:

At the lowest energies of the spectrum ($E < 3 \times 10^{11}$eV), cosmic rays are associated with solar flares and solar wind induced phenomena. For higher but lower than $\times 10^{15}$eV, energies the first order Fermi mechanism at shock waves of supernovae remnants inside the Milky Way can account for the measured spectrum[Biermann & Sigl 2001].

At energies $\sim 3\times10^{15}$eV there is a steepening of the spectrum and the spectral index raises a bit ($\alpha \approx 3$); this is known as the first knee. For energies $\sim 4 \times 10^{17}$eV the steepening increases even higher ($\alpha \approx 3.3$) but it goes back to 2.7, at what is known as the ankle for energies $\sim 5 \times 10^{17}$eV.
This features are to be understood, as a collection of contributions of different astrophysical objects with different accelerating mechanisms at specific energies. Nevertheless some possible explanations about the cause of this features have been around for some time.
The second knee could be the end of the galactic component in the cosmic ray flux or, also, possibly it could be the accumulation of pair production due to proton interaction with the cosmic microwave background.
On the other hand the ankle could also be an indication of the same process of transition between intergalactic and extragalactic components ,or perhaps the result of diffusive propagation of extragalactic nuclei throughout our galaxy's magnetic fields[Medina Tanco 2001] [Medina-Tanco 1999].

1.1.2 Acceleration and propagation of cosmic rays

There are several possible mechanisms that could in principle accelerate EECR. The *b*ottom -up mechanisms relay on "conventional " accelerating of charged particles in the presence of electromagnetic fields. Although this magnetic fields may not arise as a consequence of conventional phenomena.

Commonly accepted accelerating mechanisms are the Fermi mechanisms, proposed by Fermi in 1949[Fermi 1949], which are based on stochastic acceleration in magnetized plasma clouds where a shock wave is transversing it. This shock wave creates 2 different magnetic domains separated by the wave front. As previously stated, particles gain energy going back and forth through this two different domains. Allegedly , this kind of shock waves are present in hot lobes of radio galaxies or in supernovae remnants.
For example, the active galactic nuclei (AGN) eject plasma jets due to the strong magnetic fields produced in the region near the accretion disk. This induces a shock wave which travel through the jet region up to to its terminal region [Biermann & Sigl 2001]
.

Another kind of accelerating regions are neutron stars. The rapid spinning of this higly compact and magnetized stars can produce electric fields with strengths capable of accelerating particles to energies of 10^{20}eV [Berezinsky et al. 1990]. Although this mechanism can rapidly account for the EECR energy, still it has the major disadvantage of having great energy losses in the immediate vicinity of the accelerating region, due to interactions with the highly ionized medium.

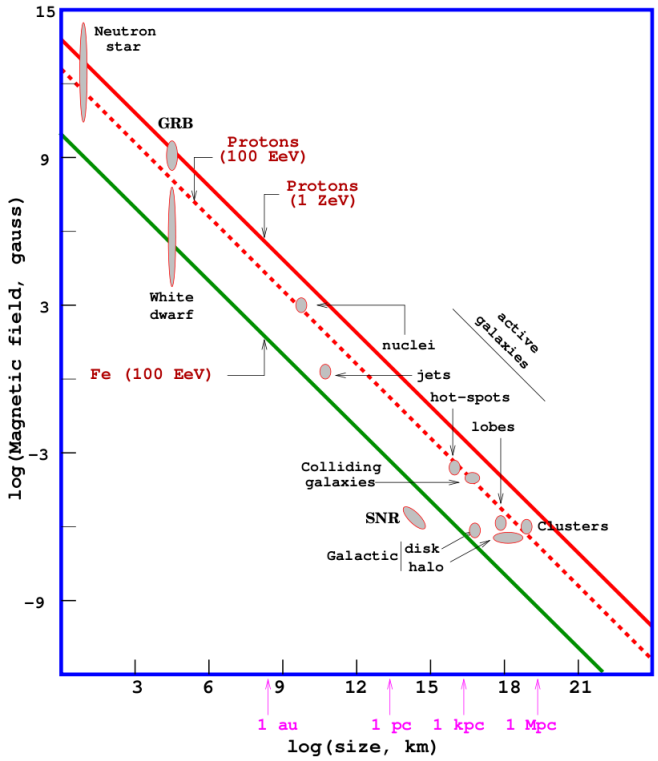

Figure 1.2: Magnetic Field and size of some possible accelerating sites. Diagonal lines correspond to Fe nuclei at 10^{20}eV (green) and protons at 10^{20}eV and 10^{21}eV (red dashed and solid lines) from equation 1.2. All objects below aforesaid lines are cannot accelerate these particles to such energies. (rec. [Supanitsky 2007]

Details of each particular mechanism (Fermi first order, second order) may be different, as this acceleration takes place in distinct astrophysical objects with suitable conditions. Nevertheless a pervading restriction arises to this suitable conditions: the gyro magnetic radius (r_g) of the particle must be contained in the astrophysical object. Regardless of the acceleration mechanisms, this regions have a related proper size (R_{object}), thus [Hillas 1984]:

$$r_g = \frac{E}{2c\beta ZeB} < R_{object}$$

should be expected. This results yields a limit to the accelerators' proper size for a

given energy E_{max}:

$$E_{max} = 2c\beta ZeBL_{object} \approx \beta Z \left(\frac{B}{\mu G}\right)\left(\frac{R_{object}}{kpc}\right) 10^{18} eV \tag{1.2}$$

Greisen-Zatpsepin Kuz'min cut-off mechanism

For any cosmic ray propagating from its accelerating source there are certain energy losses as a consequence of the interaction with the cosmic microwave background. At energies E$\sim 10^{18}$eV the prevailing process for energy loss is pair production:

$$p + \gamma_{2.7K} \rightarrow p + e^+ + e^-$$

In the early 1960's Greisen,Zatpsepin and Kuz'min, [Greisen 1966][Zatsepin & Ku'smin 1966] lead by the discovery of the cosmic microwave background, analyzed the energy losses of cosmic rays with energies above 5×10^{19}eV due to production of pions in the following process:

$$\begin{aligned} p + \gamma_{2.7K} \rightarrow \Delta^+ &\rightarrow n + \pi^+ \\ &\rightarrow p + \pi^0 \end{aligned}$$

In the case of the primary being a a heavy nucleon, the process is photo disintegration and pair production:

$$\begin{aligned} A + \gamma_{2.7K} &\rightarrow (A-1) + N) \\ &\rightarrow (A-2) + 2N \\ &\rightarrow A + e^+ + e^- \end{aligned}$$

This kind of processes strips 20% of the primary's original energy each 6 MPc, from the observers frame of reference. Therefore assuming an homogeneous distribution of the sources, the flux should have a very drastic cut-off at these energies. At present times the debate over whether this GZK cut-off has already been seen by experiments like the Pierre Auger Observatory or HiRes, is still going on. There is some evidence of an abrupt fall of the flux in this energy region, but it is still unclear if this is the celebrated GZK cut-off or just the energy limit of the cosmic accelerators [Medina Tanco 2001].

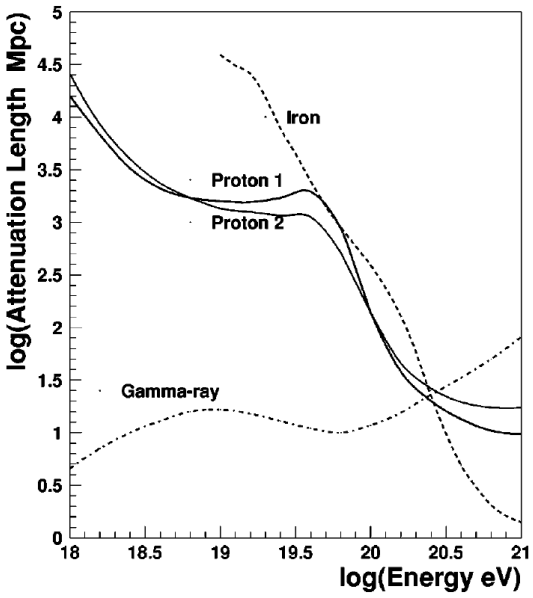

Figure 1.3: Attenuation lengths of proton, iron, and gamma-ray primaries due to interactions with the cosmic radiation background.[Nagano & Watson 2000]

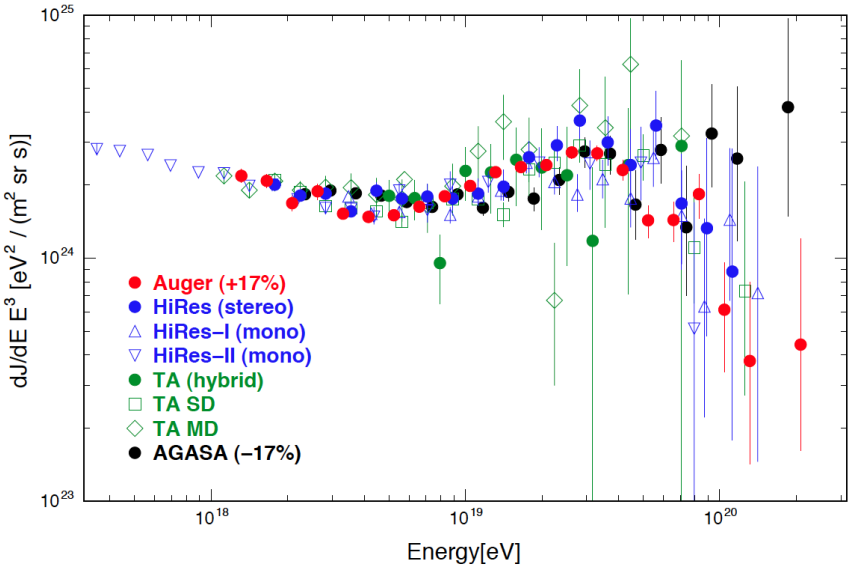

Figure 1.4: Energy spectra of EECRs observed by Auger [Pierre Auger Collaboration 2008], HiRes [HiRes 2004], AGASA [Yoshida et al. 1995] and Telescoper Array [Telescope Array 2009]. The energy scale is shifted by +17% for Auger, and by –17% for AGASA . The vertical axis is multiplied by E^3 to enhance the structure of the spectrum.

1.1.3 Extensive Air Showers(EAS)

Hadronic Interactions

As observed by Auger and his collaborators [Auger 1939] primary cosmic rays may trigger a shower of secondary particles after they interact with the upper regions of the atmosphere.In this showers, if the primary is a nucleon(proton or neutron) (N) the shower initiates with an hadronic interaction:

$$N + A_{air} \rightarrow A'_{air} + N + m(\pi^+ + \pi^- + \pi^0) \tag{1.3}$$

where A is an air nucleus, A' is the same nucleus in an excited state and m is the number of pions produced. If the primary is a nucleus a similar equation may be written, but in this case both nuclei will be in an excited state after the interaction. Part of the primary's energy lost in the form of secondary particles(mostly baryons, π and K mesons). This secondary particles constitute the extensive air shower (EAS). The EAS has three components: electromagnetic, muonic and hadronic(Fig. 1.5. The fraction of energy that is lost in the first interaction is called the *inelasticity* of the interaction. The number of secondary particles is called the *multiplicity*. The secondary particles acquire some momenta in the transverse direction to primary's incident trajectory, hence the expression "shower lateral" profile.The secondary mesons are bound to decay , although they may interact further with the atmosphere. The principal decay mechanisms are:

$$\begin{aligned}
\pi^0 &\rightarrow \gamma + \gamma \\
\pi^+ &\rightarrow \mu^+ + \nu \\
\pi^- &\rightarrow \mu^- + \bar{\nu} \\
K^\pm &\rightarrow \mu^\pm + \nu
\end{aligned}$$

.

Pion decay is responsible for the electromagnetic shower, which in turn is responsible for 90 % of the primary's energy dissipation in the atmosphere.

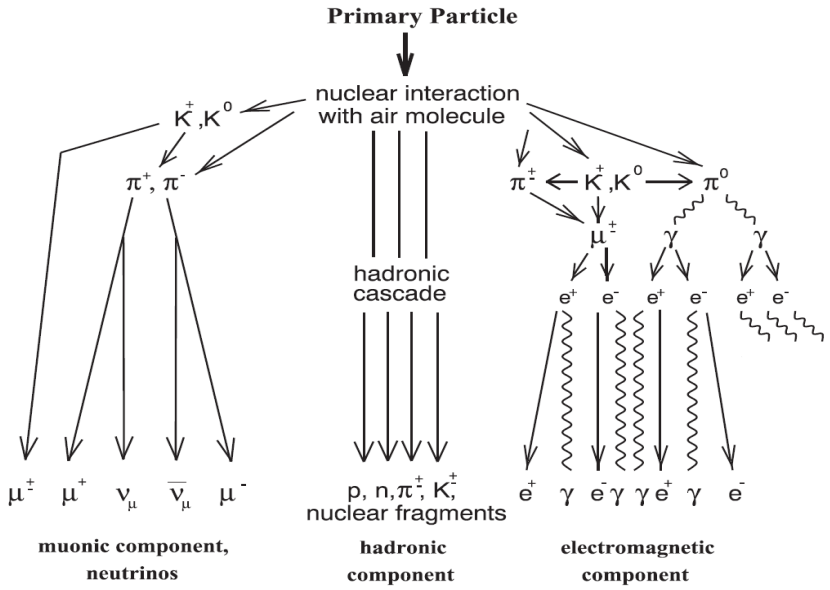

Figure 1.5: Schematic view of an EAS. At ground level the electromagnetic component is the most abundant, followed by the muonic component. [Supanitsky 2007]

1.1.4 Shower Simulations

Monte Carlo (MC) simulation of (EAS) is the most common method to calculate detailed theoretical predictions needed for interpreting experimental data. Some examples are AIRES [Sciutto 1997] and CORSIKA [Pierog & Heck 2011]. The biggest uncertainty in computer simulations of the showers comes from the hadronic interaction models used in the simulations. There are several models for the hadronic interaction (i.e QGSJET,DPMJET and NEXUS based on Gribov -Regge theory and Sibyll based on Quantum Chromodynamics).

However, for primary particles of very high energy, straight-forward MC simulation is not a viable option because of the unreasonably large computing time required. Despite of this fact, the most basic observable parameters depend on a small set of characteristics of the air-hadron interaction; for example X_{max} depends highly on the dispersion cross section, multiplicity and the inelasticity.

An alternative simulating procedure is to describe EAS development numerically, based on the solution of the corresponding cascade equations. Combining this with an explicit MC simulation of the most high-energy part of an air shower allows one

to obtain accurate results both for average EAS characteristics and for their fluctuation. This is essentially the backbone of CONEX [Bergmann 2007], which is the code used in the present work.

CONEX calculation scheme consists of two main stages: an explicit MC simulation of the cascade for particles with energies above some chosen threshold E_{thr} (being a free parameter of the scheme) and a solution of nuclear-electro-magnetic cascade equations for sub-cascades of smaller energies. The MC treatment of the e/m cascade is realized by means of the EGS4 code, supplemented by an account of the Landau-Pomeranchuk-Migdal effect [Landau et al. 1953] for UHE electrons,positrons and photons.

The hadronic integro-differential equations are given by [Bossard et al. 2001]:

$$\begin{aligned}\frac{\partial h_a(E,X)|_T}{\partial X} = &-\frac{h_a(E,X)|_T}{\lambda_a(E)} - h_a(E,X)|_T \frac{\frac{\mathrm{d}L}{\mathrm{d}X}|_T}{\tau_a(E)c} + \frac{\partial}{\partial E}\left(\beta_a^{ion}(E) h_a(E,X)|_T\right) \\ &+ \sum_d \int_E^{E_{max}} dE' h_d(E',X)|_T \left[\frac{W_{d\to a}(E',E)}{\lambda_d(E')} + D_{d\to a}(E',E)\frac{\frac{\mathrm{d}L}{\mathrm{d}X}|_T}{\tau_d(E)c}\right] \\ &+ S_a^{had}(E,X)|_T\end{aligned} \tag{1.4}$$

In this last expression:

- $h_a(E,X)|_T$ is the differential energy spectra of type a hadronic particles, along a straight line trajectory (indicated by T).
- $\frac{h_a(E,X)|_T}{\lambda_a(E)}$ represents the decrease of hadrons type a due to interactions with air nuclei, introducing the corresponding mean free path λ_a.
- $\beta_a^{ion}(E) = -\frac{\mathrm{d}E_a}{\mathrm{d}X}$ is the ionization energy loss per depth unit.
- $h_a(E,X)|_T \frac{\frac{\mathrm{d}L}{\mathrm{d}X}|_T}{\tau_a(E)c}$ describes particle decay. With τ_a being the life time of the hadron a in the laboratory system.
- $$\sum_d \int_E^{E_{max}} dE' h_d(E',X)|_T \left[\frac{W_{d\to a}(E',E)}{\lambda_d(E')} + D_{d\to a}(E',E)\frac{\frac{\mathrm{d}L}{\mathrm{d}X}|_T}{\tau_d(E)c}\right]$$
  represents the production of a particles as a byproduct of interactions and decays of higher energy parents of type d .

- $S_a^{had}(E,X)|_T$ represents the source term. Defines the initial conditions and is determined during the MC simulation of above-threshold particle cascading.

For the electromagnetic component of the shower . The corresponding equations[Gaisser 2002] are given by:

$$\begin{aligned}\frac{\partial l_{e^\pm}(E,X)}{\partial X} &= -\sigma_{e^\pm}(E) l_{e^\pm}(E,X) + \frac{\partial}{\partial E}\left(\beta^{ion}_{e^\pm}(E) l_{e^\pm}(E,X)\right) \\ &+ \int_E^{E_{max}} dE' l_{e^\pm}(E',X) W_{e^\pm \to e^\pm}(E',E) \\ &+ \int_E^{E_{max}} dE' l_{e^\mp}(E',X) W_{e^\mp \to e^\pm}(E',E) \\ &+ \int_E^{E_{max}} dE' l_{\gamma}(E',X) W_{\gamma \to e^\pm}(E',E) \\ &+ S^{e/m}_{e^\pm}(E,X)\end{aligned} \tag{1.5}$$

, for electrons and positrons; and for photons we have:

$$\begin{aligned}\frac{\partial l_{\gamma}(E,X)}{\partial X} &= -\sigma_{\gamma}(E) l_{\gamma}(E,X) + \frac{\partial}{\partial E}\left(\beta^{ion}_{\gamma}(E) l_{\gamma}(E,X)\right) \\ &+ \int_E^{E_{max}} dE' l_{\gamma}(E',X) W_{\gamma \to \gamma}(E',E) \\ &+ \int_E^{E_{max}} dE' l_{e^-}(E',X) W_{e^- \to \gamma}(E',E) \\ &+ \int_E^{E_{max}} dE' l_{e^+}(E',X) W_{e^+ \to \gamma}(E',E) \\ &+ S^{e/m}_{\gamma}(E,X)\end{aligned} \tag{1.6}$$

For this set of equations most of the terms resemble those just explained for eq. 1.4; $l_{e^\pm,\gamma}(E,X)$ are the the energy spectra of electrons, positrons, and photons respectively at depth X. $\sigma_{e^\pm,\gamma}(E,X)$ are the interaction cross sections (in units mass/area), while $W_{d\to a}$ are the corresponding differential energy spectra of secondary particles. This last two terms take into account bremsstrahlung, Møller scattering(electron-electron scattering), Bhabha scattering(electron-positron scattering), Compton effect, photonuclear, annihilation and pair production processes. As before a term for energy losses is introduced as well as the source term $S^{e/m}_{\gamma}(E,X)$.

One starts with the primary particle of given energy, direction and initial position in the atmosphere. For a hadron as primary particle, one simulates the hadronic cascade explicitly, recording all secondary particles at a number of pre-chosen depth levels and energy intervals, until all produced secondaries have an energy lower than the threshold E_{thr} . The levels are defined with respect to the projected depth X, i.e. the slant depth for the particle position projected to the initial shower axis (shower trajectory). In case of the primary particle being a photon or an electron, the simulation process starts with the calculation of possible interactions with the geomagnetic field using a PRESHOWER routine (this accounts for the geomagnetic pair production and bremsstrahlung). Each step's output becomes an input for the next stage of the the simulation.

All sub-threshold hadrons/muons and electromagnetic particles are filled into energy-depth tables that form the "source terms" for the cascade equations. Meanwhile the above-threshold electromagnetic particles are used for simulating the electromagnetic particle cascade in a similar way, with this electromagnetic cascade sub-threshold secondary particles being added to the electromagnetic source terms of the whole scheme.

In the next step the hadronic cascade at energies below E_{thr} is calculated numerically for the first depth level using the corresponding cascade equations and initial conditions specified by the source terms. As the result, one obtains discretized energy spectra of hadrons of different types at the next depth level. All sub-threshold electromagnetic particles produced at this stage are added to the electromagnetic source term. Then sub-threshold electromagnetic cascades are calculated by solving the corresponding electromagnetic cascade equations for the given initial conditions.

Hadrons due to photonuclear interaction and pair-produced muons that are generated in the numerical solution of the electromagnetic cascade Eqs. 1.5 and 1.6 are added to the hadronic source (Eq. 1.4) term of the next slant depth level. This procedure is repeated for the following depth levels, each time using the hadronic and electromagnetic source terms of the previous level. Till a maximun slant depth is finally reached (another free parameter of the scheme, usually set to $2000 g/cm^2$).

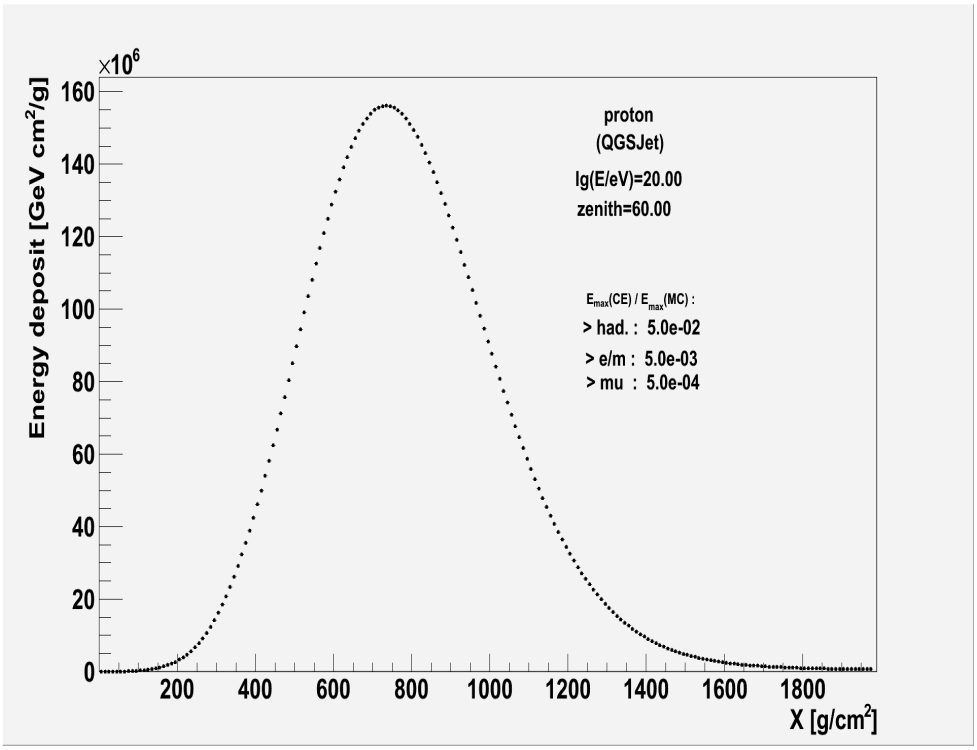

Figure 1.6: Energy deposition as a function of slant depth for a typical shower simulated using CONEX. Energy is 10^{20}eV and zenith angle is 60° .

1.2 JEM-EUSO

1.2.1 Mission overview & Observation principle

In order to observe EECR, it is clear from section 1.1.1, that ground based experiments, such as the *Pierre Auger Observatory* (PAO), and HiRes, fail to have enough exposure to the lowest flux of the CR spectrum and thus, the highest energies of the aforesaid spectrum.

To address this issue a new type of observatory is currently being developed, the Extreme Universe Space Observatory on Japanese Experiment Module (JEM-ESUO)[JEM-EUSO Collaboration]. Under the current design considerations, JEM-EUSO in turn could initiate a new field of astronomy and astrophysics using the extreme energy particle channel, by achieving more than $10^5 km^2 sr yr$ above energies of 7×10^{19} during its first three years of operation.

JEM-EUSO is a super wield field telescope which uses the whole Earth as a detector, to observe transient luminous phenomena taking place in the atmosphere caused by particles and waves coming from Space. This remote-sensing instrument on-board the International Space Station (ISS), orbits around the Earth approximately every 90 minutes at an altitude between 300km and 400 km.

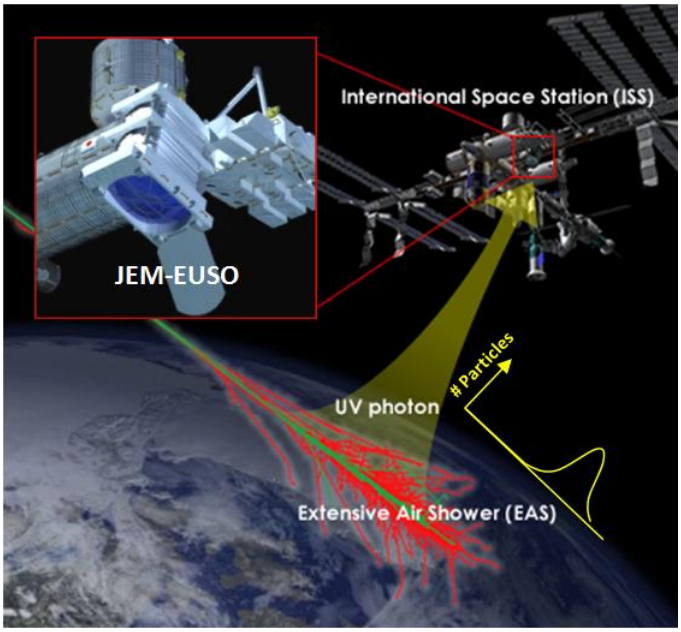

Figure 1.7: Artistic depiction of JEM-EUSO's operational principle. UV light produced by the EAS, originated by the extreme energy particle, is captured from space, allowing an unprecedented instantaneous exposure.

JEM-EUSO's telescope captures the moving track of the fluorescent Ultra Violet photons, with the aid of its super wide($\pm 30°$) Field-of-View(FoV), with optics composed by Fresnel lenses. It shall be able of recording the track of an EAS with a time resolution of $2.5\mu s$ and a spatial resolution of 0.75 km in nadir mode. JEM-EUSO's first few years of operation will be devoted to observe the lower energy region in the "nadir mode" and then later to observe high energy regions in the "tilted mode". This is due to an increase in the effective area by tilting the telescope off-nadir. In this "tilted" mode, the threshold energy gets higher since the mean distance from the EAS core to the detector, as well as the atmospheric absorption and dispersion both increase.

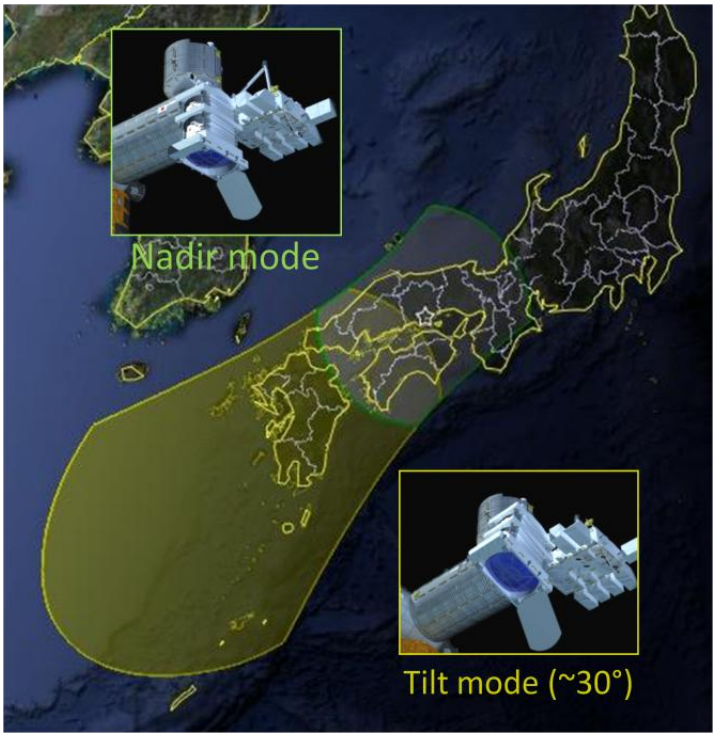

Figure 1.8: Artistic comparison of both "normal" and "tilted" modes, instantaneous areas.

The JEM-EUSO telescope can reconstruct the incoming direction of the EECRs with accuracy better than a few degrees. Its observational aperture of the ground area is a circle with 250 km radius, and its atmospheric volume above it is $\sim$ 1 Tera-ton or more(JEM-EUSO has a 60° FoV). The instantaneous aperture of JEM-EUSO is larger than the PAO by a factor ranging from 65 to 280, depending on its observation mode.

1.2.2 Scientific objectives

Opening the window to the "particle" channel in astronomy JEM-EUSO will be able to address many basic problems of fundamental physics and high-energy astrophysics. Overall, JEM-EUSO's data will shed light on the origin of the EECRs, on the sources that are producing them, on the propagation environment from the source to the Earth and, possibly, on the particle physics mechanisms at energies well beyond the ones achievable in man-made accelerators. Moreover, exploratory objectives such as constraining the Galactic and extragalactic magnetic fields, the detection of extreme energy neutrinos and gamma rays, the verification of special relativity at extremely

large Lorentz factors, the examination of possible quantum gravity effects at extreme energies, and the systematic surveillance of atmospheric phenomena, complete the scenario of the JEM-EUSO science goals[Medina-Tanco et al. 2009].

Astronomy and Astrophysics

As previously stated JEM-EUSO's design will allow more tha $10^5 km^2 sryr$ above 5×10^{19}eV which in turn should, under current uncertainties, amount upto 500-800 events above 5.5×10^{19}eV. This expected amount of events should allow for the identification of individual sources by high-statistics arrival direction analysis; moreover, it should allow the measurement of the energy spectra from such sources, which in turn will provide constrains to emission mechanisms.

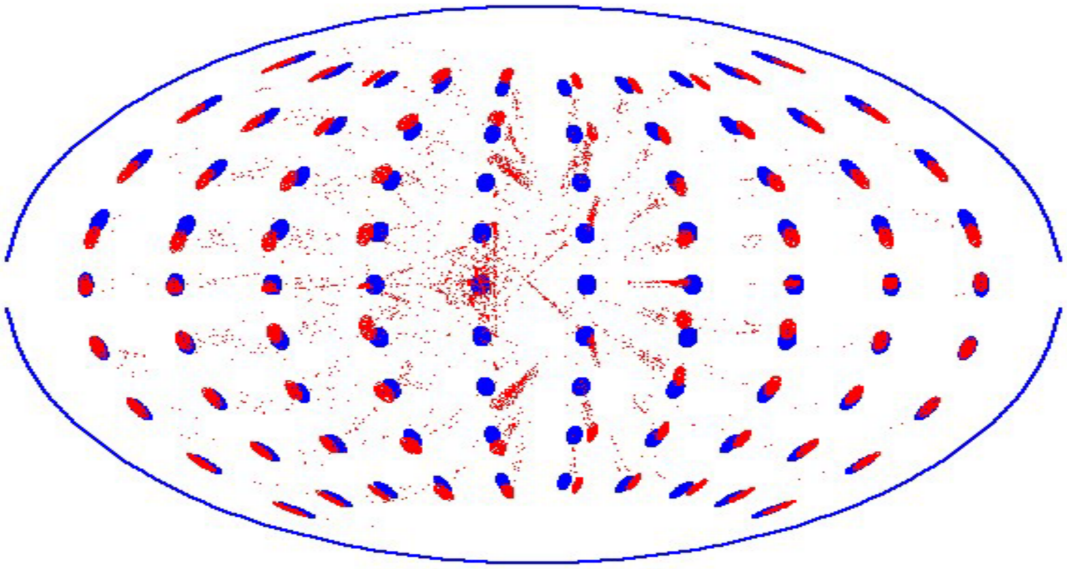

Figure 1.9: Deflection scenario for protons at energies of $10^{20} eV$. Blue dots are "circular " regions of 2.5° diameter, where protons entered the galactic Halo. The red dots represent the perceived direction of arrival of such regions afeter being deflected through the galactic magnetic field.(rec. [Medina-Tanco 2009]

Identification of sources. Point source and global anisotropy analysis.

This is one of two of the most fundamental scientific objectives of the JEM-EUSO mission. In order to verify the origins of the EECR, JEM-EUSO will rely on its

unprecedented exposure to achieve a high-statistics arrival direction analysis. This arrival direction must take into account the intervening magnetic fields , and is performed in two different approaches: point source and global anisotropy analysis.

The point source analysis seeks for small-scale clustering of events. This kind of clustering has already been reported by AGASA, HiRes and the PAO around Active Galactic Nuclei (AGN) [Yoshida et al. 1995] [Abbasi,Abu-Zayyad,Amann 2004], [PAO Anisotropy 2007]. Furthermore, this cross correlation was reported by the PAO for EECR in energies in the excess of 6×10^{19}; if this anisotropy signal is true, JEM-EUSO should identify several dozen clusters with tenths of events associated to each of them. This will allow to correlate the sources with known astronomical object, allowing for source's distance determination, and a much more clear spectral analysis.

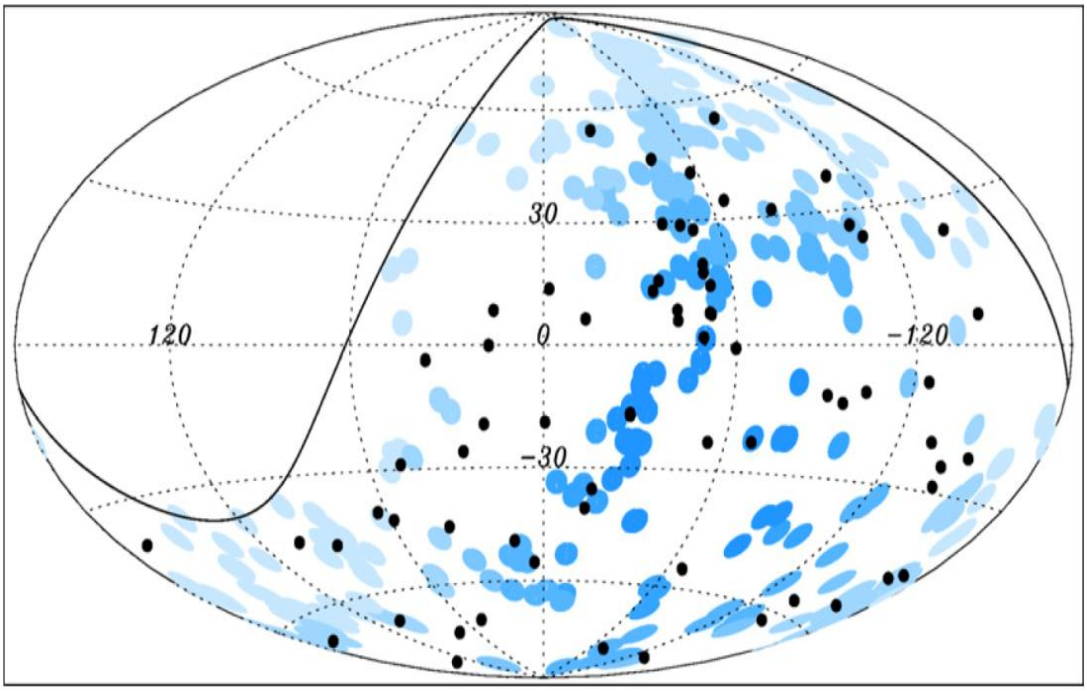

Figure 1.10: Anisotropy seen by Auger. [PAO Anisotropy 2007]

Exploratory Objectives

Regarding the Cosmic Neutrino Background, JEM-EUSO could pioneer in their measurement of the relic neutrinos, which are nearly as abundant as the relic photons,

and could provide a new window to earlier times when the universe was just 1 s old. A recently proposed possibility for detecting relic neutrinos from the Big Bang indirectly is based on so-called Z-bursts resulting from the resonant annihilation of ultrahigh-energy cosmic neutrinos with relic neutrinos into Z bosons. On resonance, the corresponding cross-section is enhanced by several orders of magnitude. Such resonance energies are, for neutrino masses in the 4×10^{20}eV range. It has been argued recently that ultrahigh-energy cosmic rays above the predicted GZK cut-off are mainly protons from Z-bursts [Wieler 1982]. This would possibly solve one of the outstanding problems of ultrahigh energy cosmic ray physics the observation of cosmic rays with energies above the GZK cut-off in an elegant and economical way without invoking new physics beyond the Standard Model, other than neutrino masses.

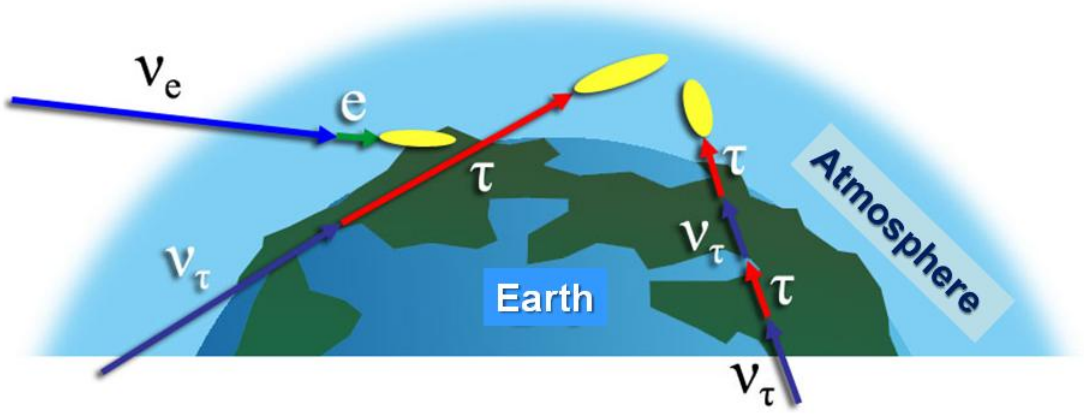

Figure 1.11: Schematic view of EAS initiated by extreme energy neutrinos. Neutrinos at $\sim 10^{20}$ eV deeply penetrates the atmosphere and may initiate EAS near the surface of the Earth.

Ultrahigh-energy neutrinos produced at cosmological distances can reach our cosmological neighborhood unattenuated and their resonant annihilation with relic neutrinos could result in the observed cosmic rays of the highest energies. If indeed these trans GZK cosmic rays are produced via Z-bursts, then the energy spectrum of the highest-energy cosmic rays would depend critically on neutrino mass. From a comparison of the predicted spectrum with the observed one, the required mass of the heaviest neutrino can therefore be inferred.

JEM-EUSO will explore the Z-burst model and aim at the indirect detection of the CNB. If the detection of ZeV neutrinos is achieved in this way, then the key discriminator of models is whether such neutrinos are correlated with the super-cluster. This kind of neutrino anisotropy measurement [Tiffenberg 2009] will constraint the

Z-burst model and create an opportunity to estimate the absolute mass of neutrinos.

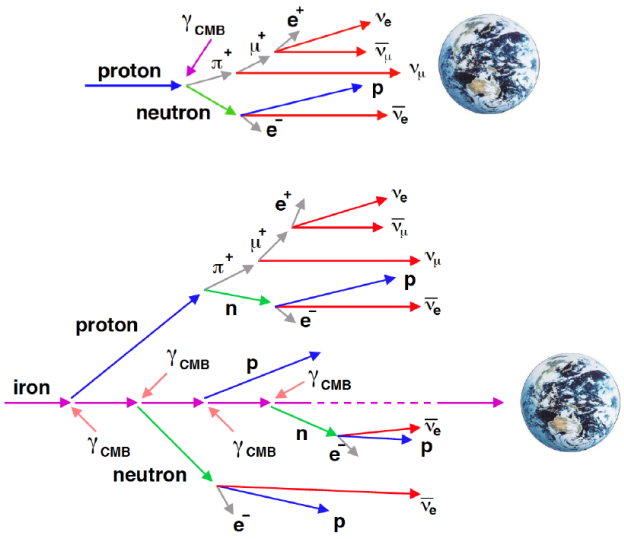

Figure 1.12: (a) Schematic view of cosmogenic neutrino production as a result of the GZK mechanism. (b)Heavier nuclei can also produce neutrinos. Both processes leave their particular imprint in the neutrino background.

1.2.3 Optics and Focal Surface subsystems

The study introduced an innovative design based on a refractive system made of two curved double-sided Fresnel lenses in PolyMethyl Methacrylate (PMMA) material (Mitsubishi Rayon Co., Ltd. product). Since then, many improvements have been made, dealing with the design and therefore the optical performances, based on: a) further studies of better performing materials, and b) the addition of an intermediate lens with a circularly symmetric diffractive surface from one side and a Fresnel surface on the other one, working as a sort of field lens and used to compensate for some of the chromatic aberration. For the JEM- EUSO OM, two versions of the same philosophy are being presented: a baseline and an advanced design. The JEM-EUSO Baseline optics uses a PMMA material more suitable for the near UV (PMMA-000 grade). The JEM-EUSO Advanced option presents changes in the materials‘ choice with respect to the Baseline; the front curved double-sided Fresnel lenses is in CYTOP material (AGC Co., Ltd. product), while the PMMA-000 is maintained for the middle and back lenses. Consequently, the optimization of the design gives parameters for the three lenses different than those for the Baseline.

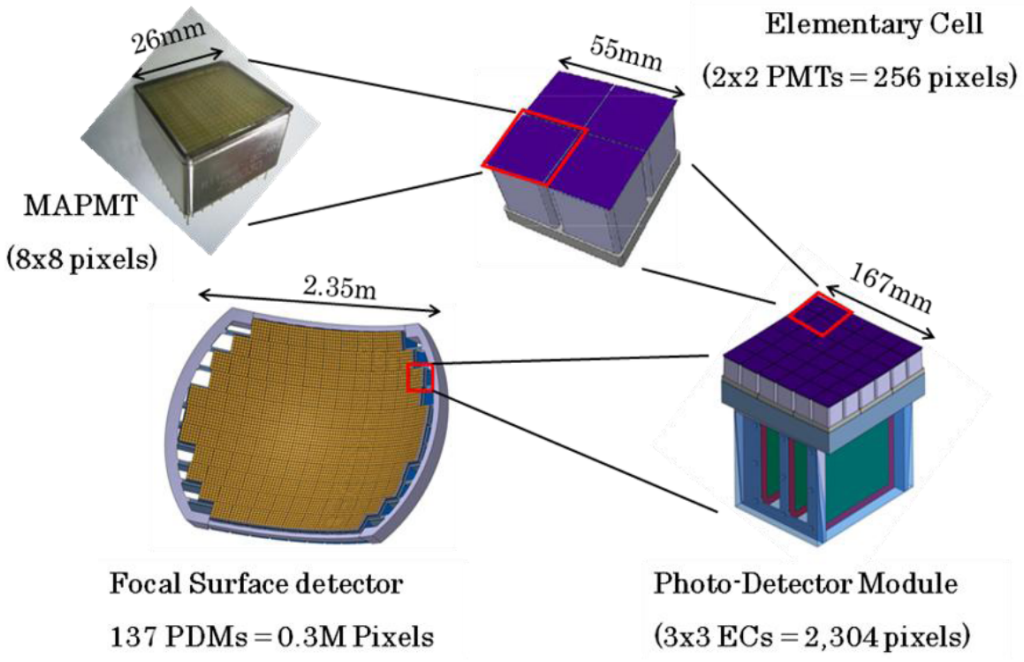

Figure 1.13: Focal surface detector and its structure. [JEM-EUSO Collaboration]

The Focal Surface (FS) of JEM-EUSO has a curved surface of about 2.35 m in diameter, and it is covered with more than 5,000 Multi-Anode PhotoMultiplier Tubes, MAPMTs, (Hamamatsu R11265-M64). The FS detector consists of Photo-Detector Modules (PDMs), each of which consists of 9 Elementary Cells (ECs) arranged in an array of 33. About 1,233 ECs, corresponding to about 137 PDMs, are arranged on the whole FS (see Fig. 1.13).

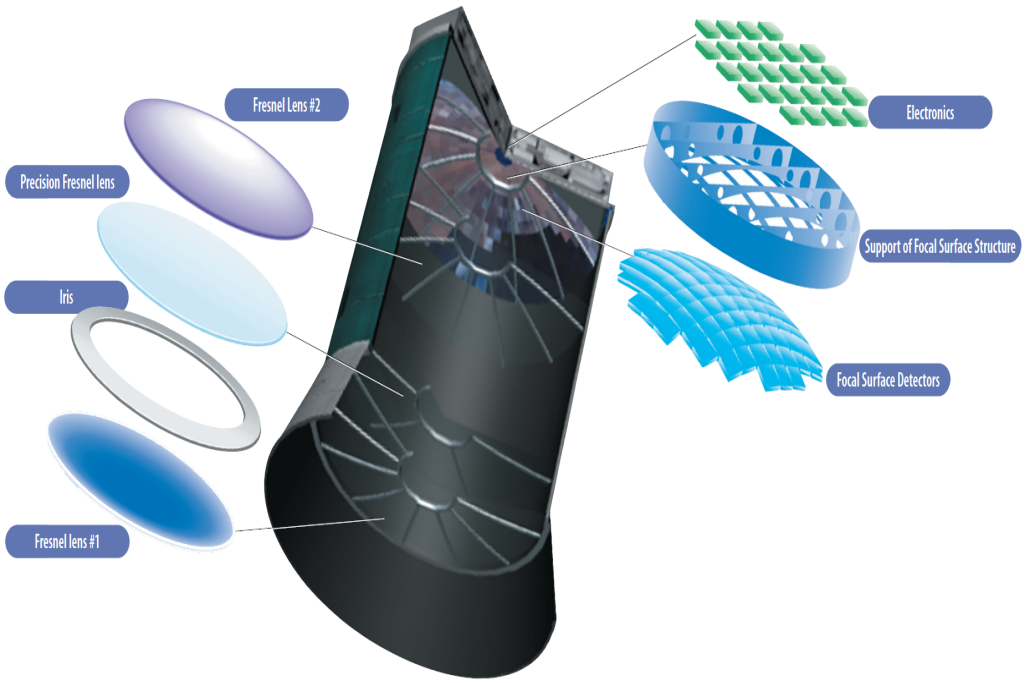

Figure 1.14: Artistic depiction of JEMEUSO summarizing the optics and focal surface layout.

1.2.4 Atmospheric Monitoring Subsystem

The aim of the Atmospheric Monitoring (AM) system is to observe the condition of the atmosphere in the field of view of the JEM-EUSO main telescope. The strength of the fluorescent light and Cherenkov light emitted from EAS and their transmission process depend on the transparency of the atmosphere, the cloud coverage and the height of cloud top. In case of events above 10^{20} eV, the existence of the cloud can be directly derived by the analysis of the EAS signals detected by the JEM-EUSO main telescope. Nevertheless, the detailed monitoring of the cloud coverage by a proper AM system is important to estimate the effective observing time with a high accuracy and to increase the confidence level in the events just above the energy threshold of the telescope. The JEM-EUSO mission, therefore, has its own Atmospheric Monitoring subsystem as far as the impact onto mass and power budget is insignificant. The Atmospheric Monitoring consists of:

- Infrared camera
- LIDAR
- Analysis of slow data detected by the JEM-EUSO telescope.

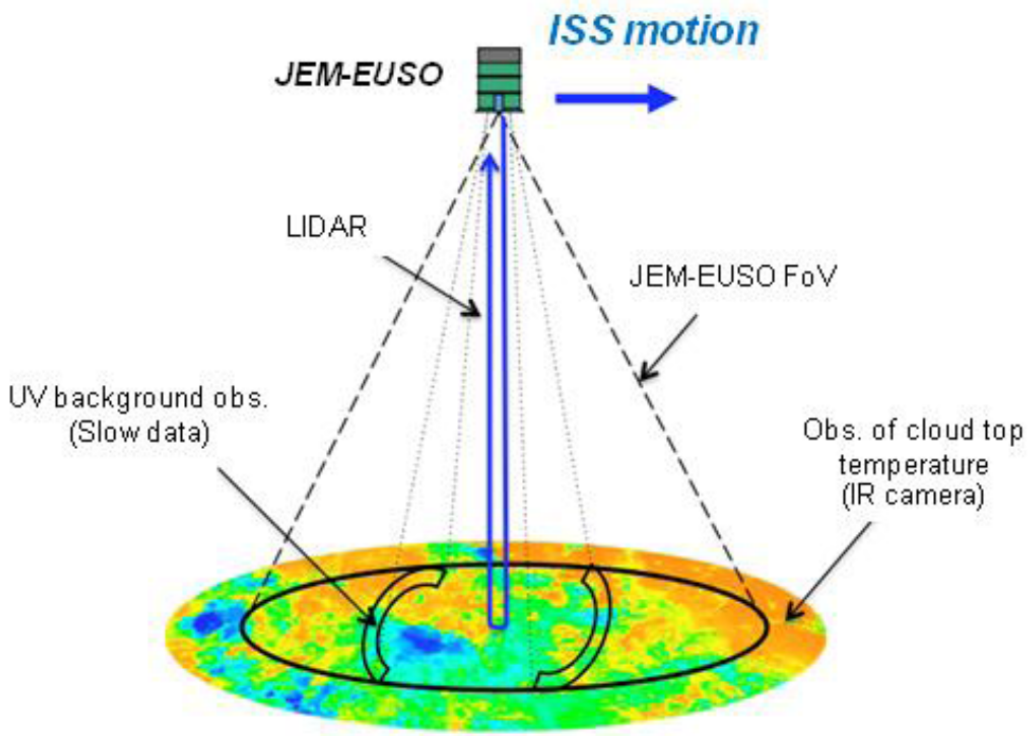

Figure 1.15: Atmospheric monitoring subsystem.

Infrared camera

The Infrared (IR) camera is an infrared imaging system used to detect the presence of clouds and to obtain the cloud top altitude during the observation period of the JEM-EUSO main telescope. Since the measurement shall be performed at night, the cloud top height shall be based on cloud IR emission. The radiance observed is basically related to the target temperature and emissivity and, in this particular case, it can be used to get an estimate of how high clouds are

The current baseline of the IR camera consists of a refractive optics made of germanium and zinc selenide and an uncooled microbolometer array detector. Interferometer filters limit the wavelength band to 10-12 μm.

Table 1.1: IR Camera Current requirements

Parameter	**Requirement**
Measurement temperature range	$200 \div 300$ K (accuracy of 3 K)
Wavelength	2 bands$10 \div 12\mu$m plus one for calibration
Angular Resolution	0.25°
Number of pixels	320×340

LIght Detetion and Raging (LIDAR)

The purpose of Lidar is to carry out ranging measurements at several positions in the field of view of JEM-EUSO so to achieve the determination of the cloud-top altitude with high accuracy. The direct observation data of the cloud-top altitude obtained by Lidar serves as calibration data for what obtained by the IR camera. The ranging resolution of Lidar is 30 m; from data by both IR camera and Lidar, the 3-dimensional cloud distribution and cloud-top altitude are determined. The Lidar system of JEM-EUSO is composed of transmission and receiving systems. The transmission system comprises a Nd:YAG laser and a pointing mechanism for the irradiation beam. The third harmonic ($\lambda = 355$ nm) of the Nd:YAG laser is used. The JEM-EUSO telescope itself is used for the receiving system of Lidar. Four photo-detectors are placed on the focal surface to measure the backscattered light, so that there is a visual field in the laser irradiation direction from Lidar. Because the wavelength of the laser from Lidar is in the range of $\lambda = 330 \div 400$ nm, which is the range of atmospheric fluorescence and Cherenkov light, the focal surface detector (the MAPMTs) of JEM-EUSO can also be used as a Lidar receiver unit.

In particular, the cloud top height and cloud coverage are obtained by the infrared images and by the Lidar data which are used in the estimation of the effective observational volume and in the reconstruction of the event (more on this will be discussed in chapter 3).

Table 1.2: Specifications for the JEM-EUSO Lidar

Parameter	**Requirement**
Wavelength	355 nm
Repetition rate	50Hz
Pulse width	$5 \div 15$ns
Pulse energy	20 mJ/pulse
Beam divergence	0.1 mrad
Detector	MAPMT(JEM-EUSO)
Range resolution	30 m

Requirements derived from the scientific objectives for the AM Subsystem

The required precision of the measurement of the extinction coefficient $\alpha(\vec{x}, \lambda)$, and molecular backscatter $\beta(\vec{x}, \lambda, \theta)$ could be derived from the requirements on the precision of determination of the EECR energy and precision of determination of the depth of the EAS maximum, namely[Garino et al. 2011]:

- Energy accuracy of $\pm 30\%$
- Precision of X_{max} of $\pm 120 g/cm^2\%$

Two desired requirements for the Atmospheric Monitor System (AM) determined by the required precision of the measurement of EECR energy and determination of the depth of the EAS maximum are:

1. To measure the vertical structure of the cloud and aerosol layers with resolution better than ~ 500 m in the atmosphere region around triggered EAS events.
2. To measure the optical depthτ profile from the telescope to the location of the EAS events with an accuracy better than $\Delta\tau \leq 0.15$

Chapter 2

Space borne EECR experiments: Challenges in EAS observation.

2.1 Present work's motivation and main objectives

EAS experiments using Fluorescent Detectors (FD) have two main constituents. The first one is a UV-radiation detector. This part must have an optical mechanism to allow the collection of the scarce fluorescent light. In experiments such as PAO or JEM-EUSO the latter consists of sate of the art telescopes with a focal surface tiled with photomultiplier tubes (PMT).

The second constituent of a FD detector is the Earth's atmosphere. This very important element of the detector lacks of precise human control. Therefore, atmospheric monitoring systems are implemented to provide thorough knowledge of the measuring conditions.

Ground based FD detectors have paved the way for the development of suitable techniques to probe the atmosphere. With the forthcoming of space-borne FDs, modifications to these techniques will arise.

One of the most important differences between ground-based (GB) and space-borne (SB) atmospheric observations is the time scale involved. While in GB experiments there is a smooth variation of the atmospheric conditions, in a SB experiment there is an abrupt change due to the spacecraft movement along its orbit.

For example, transitions between a cloudy sky and a clear sky may take minutes even hours, in a GB experiment. But in a SB experiment, the scoped portion of the atmosphere will change every tenths of seconds, causing the detector to experience all possible weather conditions inside its field of view.

Another difference between GB and SB atmospheric observations is the clearly distinct geometrical configuration involved. While GB observations favor vertical

showers, SB detectors will benefit from horizontal ones. In GB detectors the longitudinal profile of vertical showers are better observed, since this geometry favors the recollection of the fluorescent light by a nearby FD.

On the other hand, SB detectors benefit more from horizontal showers. In these showers, tracks are better distributed along the FD's focal surface. Therefore, providing more information about the showers. Also, low thick clouds which could very well impede a measurement of a EAS developing at a higher altitude. In this scenario, a SB detector es still able to detect the fluorescence signal.

It is also worth mentioning the difference in latitude exposure between GB and SB experiments. Due to the night-only duty cycle, FDs take one year to sample the whole sky. Furthermore GB experiments have relative exposure to astrophysical objects fixed by their geographical coordinates. SB detectors will add another component to this issue: the clouds' latitude distribution. Seasonal variations will play an important role in the way astrophysical sources map onto the sky at Earth. All of these issues lead us to the main objective of the present work.

2.1.1 Cloud studies

As just mentioned, cloud distribution throughout the atmosphere will leave a strong imprint in the scientific results of any SB detector. Therefore, from the author's point of view, the following issues deserve a proper analysis:

Cloud coverage

The portion of the sky occupied by clouds has seasonal variations. These seasonal variations have a strong geographical dependence. Deserts, oceans, forests, cities, etc. will all become the background of a SB detector. This different landscapes have their distinct associated atmospheric conditions. Moreover, the amount of cloud coverage of the whole portion of the Earth's atmosphere observed by the SB detector will average depending in the orbital characteristics of the spacecraft.

Regarding the design of suitable atmospheric monitoring systems for a SB detector, one may ask how precise should this monitoring be. The answer to this question has several constrictions due to the limited mass and power budget available in a SB detector. Statistical studies about the correlation lengths of the structure of clouds may hold some answers to this particular issue.

Vertical Structure

Information about the vertical structure of clouds, if available, will improve the performance of a FD in space. The intrinsic atmospheric variations along the longitudinal development of the EAS affect the intensity and propagation of the fluorescent

photons produced. The vertical structure of clouds may or may not allow these photons to reach a SB detector. Since the cloud-optical-properties variations must be taken into account when interpreting the signal in the FD detectors, geometrically accurate simulations should be used to address these questions. Of course, factors such as average cloud top height, optical thickness's vertical variations must be included in these simulations. Furthermore, statistical studies of the amount and altitude of thin clouds covering the Earth's surface, and their effects on EAS reconstructions.

The **optical thickness (τ)** of the medium surrounding the EAS core is responsible for the attenuation of the fluorescent signal. Each point along the longitudinal profile of the shower defines a specific line of sight up to the detector. If this lines of sight go through clouds or aerosols, the strength of the fluorescence signal will diminish. This effect must be realized prior to the reconstruction of the event's signal. Failing to do so may lead to errors in the interpretation of the acquired data.

The main objective of the present work is to address the issues mentioned above. To do so, the use of space-borne atmospheric probing will be necessary. Using this measurements we can emulate the expected information that will be retrieved by the Atmospheric Monitoring Subsystems. Furthermore, this data provide a big enough timespan to properly estimate the average values of the relevant atmospheric conditions. Most of the previous work on similar observations,the so called "Earth Science Observations" (see chapter 3), are focused on climatology and biology. This bias, sometimes neglects the UV part of the spectrum, which is the scope of FD. Nevertheless the information acquired has proven to be of great use in our studies.

The present work aims to perform **EECR-oriented studies of atmospheric conditions** .The JEM-EUSO mission is of special interest for the present work, but results derived here could be applied to other EEECR experiments.The results of this studies have direct consequences in the astrophysical contents of any given SB mission. Some factors that depend, to some extent, in this studies are:

- Energy reconstruction. The presence of clouds may affect the trigger efficiency and the reconstructed energy in any given SB detector. This should not be forgotten when calculating the general flux of cosmic rays. The spectrum inferred must not contain biases due to cloud's tempering with the measurements.

- Primary identification. Clouds' presence along the longitudinal development of an EAS may temper with a proper reconstruction of the aforesaid EAS. Optically thin clouds may broaden the FD signal, modifying the perceived position of the shower maximum. This will ultimately mislead the detector's composition studies of the EECR.

- Arrival direction estimation. As previously stated, the vertical structure of

clouds may sometimes prove useful for a EAS reconstruction. In some cases, a thick cloud may serve as an impact point marker for the EAS core. The Cerenkov peak associated with the EAS's impact point, is very valuable to reconstruct the incoming direction of the EAS's primary. Therefore, low optically thick clouds will enhance the arrival direction estimation.

- Exposure and Duty Cycle. The portion of the sky that is covered by clouds with suitable altitude and optical thickness values, have an obvious effect on EAS observations. But we must not forget that the geographical correlation of clouds affects the relative exposure with astrophysical objects. An hypothetical source could be masked or enhanced by the cloud content in its line of sight towards the earth.

Finally, some of the current design constrains and requirements of the JEM-EUSO mission, can be seen under the light of this studies. We hope we can shed some light on some of the remaining issues that have to be tackled to assure the mission's success.

- Lidar operating mode. There are basically two different approaches to the lidar's operating mode in JEM-EUSO. The *fixed scan* mode and the *targeting* mode The fixed scan mode will probe the atmosphere in fixed positions inside JEM-EUSO's field of view. Together with the infrared camera, this mode hopes to be able to derive enough information of the atmospheric conditions, without targeting in each EAS direction. The technological advantages of this simpler mode have to be compared with the possibility of failing to detect important atmospheric features. We will study the correlation lengths of the clouds' optical properties to asses this possibility.
- Attitude uncertainty. There is an inherent attitude uncertainty as a consequence of real-time attitude uncertainty of the ISS+telescope system and the finite pointing time of the LIDAR. Depending on final design parameters, this has the potential to impact the information retrieved by JEM-EUSO's lidar due to probing a slightly shifted line of sight. In the present work, we will study the uncertainty in optical depth measurements as a consequence of the attitude uncertainty.

Chapter 3

Atmospheric features relevant to EAS's detection from space

3.1 The Atmosphere

3.1.1 Composition

The earth's atmosphere is a thin, gaseous envelope comprised mostly of nitrogen (N_2) and oxygen (O_2), with small amounts of other gases, such as water vapor (H_2O) and carbon dioxide (CO_2). Nested in the atmosphere are clouds of liquid water and ice crystals. Although our atmosphere extends upward for many hundreds of kilometers, almost 99 percent of the atmosphere lies within a mere 30 km of the Earth's surface. There is no definite upper limit to the atmosphere; rather, it becomes thinner and thinner, eventually merging with the interstellar medium. We will now proceed with our general overview of the atmospheric features that are relevant for the present work.The Earth's atmosphere has 90% of its mass below $\approx$ 18 km above mean sea level, and only 1% of its mass above $\approx$ 32km [Ahrens 2000]. Its composition is:

Table 3.1: Atmospheric composition (dry air)

Permanent gases		Variable gases	
Gas	Percent (by Volume)	Gas(and particles)	Percent (by Volume)
Nitrogen	78.08	Water Vapor	0-4
Oxygen	20.95	Carbon Dioxide	0.037
Argon	0.93	Methane	0.00017
Neon	0.0018	Nitrous oxide	0.00003
Helium	0.0005	Ozone (Stratospheric)	0.000004
Hydrogen	0.00006	Particles (dust,soot,etc.)	0.000001
Xenon	0.000009	Chlorofluorocarbons (CFCs)	0.0000002

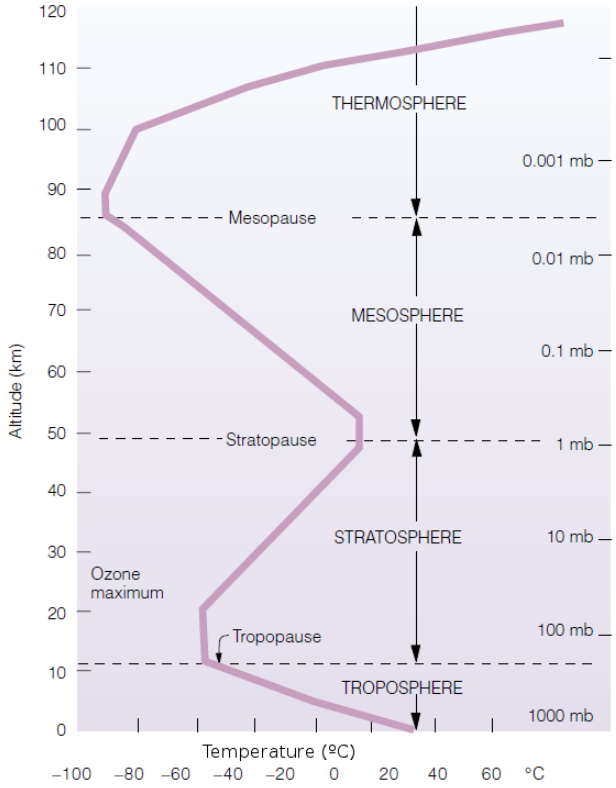

Figure 3.1: Temperature profile of the Standard atmosphere (modified from [Ahrens 2000]).

US Standard atmosphere

The principal atmospheric model used in ESAF [Naumov et al. 2010] and in CONEX [Bergmann 2007], therefore relevant for the present work, is the "Standard Atmosphere". This is a hypothetical vertical distribution of atmospheric properties which, by international agreement, is roughly representative of year-round, mid-latitude conditions. Typical usages include altimeter calibrations and aircraft design and performance calculations. It should be recognized that actual conditions may vary considerably from this standard.

The most recent definition from this model is the "US Standard Atmosphere, 1976" developed jointly by NASA, and the United States Air Force . It is an idealized, steady state representation of the earth's atmosphere from the surface to 1000 km, as it is assumed to exist during a period of moderate solar activity. The 1976 model

is identical with the earlier 1962 standard up to 51 km, and with the International Civil Aviation Organization (ICAO) standard up to 32 km.

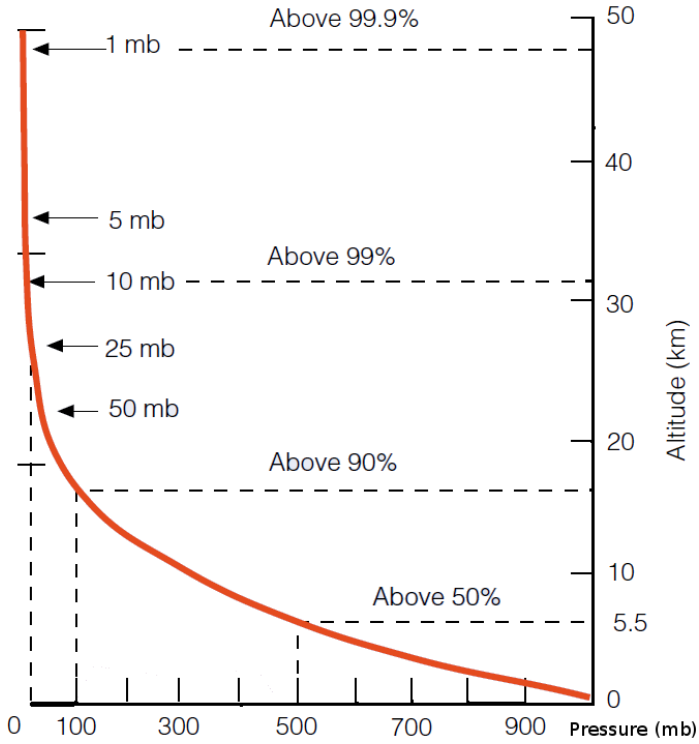

Figure 3.2: Pressure dependence of the profile of the Standard Atmosphere (modified from [Ahrens 2000]).

Up to 86 km, the model assumes a constant mean molecular weight, and comprises of a series of six layers, each defined by a linear temperature gradient (lapse rate); the assumption of linearity conveniently avoids the need for numerical integration in the computation of properties. The bottom layer, with a negative lapse rate, represents the earth's troposphere, a region where most clouds form, and with generally turbulent conditions. Higher layers form part of the earth's stratosphere, where winds may be high, but turbulence is generally low.

The model is derived by assuming a constant value for g (gravitational acceleration). Strictly speaking, altitudes in this model should therefore be referred to as "geopotential altitudes" rather than "geometric altitudes" (physical height above mean sea level). The relationship between these altitudes is given by:

$$h_{geometric} = h_{geopotential} \times \frac{R_{earth}}{R_{earth} - h_{geopotential}}$$

where $R_{earth}$is the earth's effective radius. The difference is small, with geometric altitude and geopotential altitude differing from by less than 0.5% at 30 km (100,000 ft).

The standard is defined in terms of the International System of Units (SI). The air is assumed to be dry and to obey the perfect gas law and hydrostatic equation, which, taken together, relate temperature, pressure and density with geopotential altitude.

It should also be noted that since the standard atmosphere model does not include humidity, and since water has a lower molecular weight than air, its presence produces a lower density. Under extreme circumstances, this can amount to as much as a 3% reduction, but typically is less than 1% and may be neglected.

There are 2 basic ideas behind this model. The first one is to describe the atmosphere like an ideal gas:

$$p = \rho R T$$

Where p is the pressure, ρ is the density, R is the universal gas constant and T is the temperature.

The second basic idea is that each layer has its specific lapse rate(λ):

$$T = T_n + (h - h_n)\lambda_n$$

Layer base geopotential altitude [km]	Lapse rate [$\frac{K}{km}$]
0	-6.5
11	0 (isothermal)
20	1.0 (inversion)
32	2.8 (inversion)
47	0 (isothermal)
51	-2.8
71	-2.0 (isothermal)

Combinig this 2 basic ideas, and as a consequence of hydrostatic equilibrium ($\frac{\mathrm{d}p}{\mathrm{d}h} = -g\rho$), we arrive specific state variable equations, defined for layer $n+1$:

$$\frac{dp}{p} = -\frac{g}{\lambda_n}\frac{dT}{T}$$

$$\implies \frac{p}{p_n} = \left(1 + \frac{(h - h_n)\lambda_n}{T_n}\right)^{-\frac{g}{\lambda_n R}}$$

This last expression reduces to:

$$\frac{p}{p_n} = e^{\frac{(h-h_n)g}{RT_n}}$$

for the case of isothermal layers.

As previously stated 1.2, space borne EECR experiments will detect the fluorescence light produced in the UV band in the range of 330—400 nm by the de-excitation of nitrogen molecules excited by the high-energy electron component of the EAS produced by EECR. Because the particle moves superluminally in the atmosphere, Cherenkov light is also produced and may reach the telescope. The extinction of radiation due to gaseous absorption depends on the absorber mass and on the absorption coefficients within the radiation path. The measured radiance decreases if the photon path within the atmosphere increases.

Of the many influences that the atmospheric constituents have over an EAS development, we can point out [Keilhauer 2001]:

- Higher temperature at the site of pion production cause lower air density and hence higher intensities of muons at ground because of an increase in decay rates of $\pi^{\pm}$ into $\mu^{\pm}$. (*positive temperature effect*).
- The decrease in the chance of survival for any created μ, which losses energy via ionization depending on pressure and atmospheric depth. (*negative pressure effect*).
- The fluorescence technique uses the atmosphere as a calorimeter and light propagation medium, being nitrogen and oxygen the most important contributors to the development of the EAS signal.

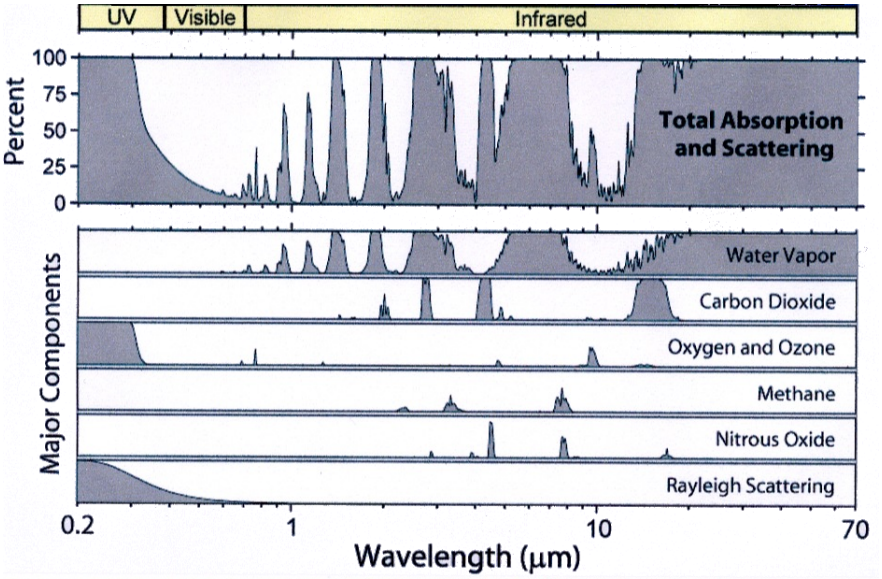

Figure 3.3: Atmospheric absorption of the electromagnetic spectrum.

3.1.2 Aerosols

Aerosols range in size from around 10 nanometers upward to around 100 micrometers. Aerosols often have serious impacts on society. They can pose a threat to public health. Tiny aerosol particles with diameters less than 2.5 μm can work their way deep into the lungs and aggravate or cause breathing problems. Aerosols can also threaten the safety of aviation by reducing visibility over heavily polluted areas. During volcanic eruptions, a major source of aerosols, planes have to be rerouted around the eruption for fear of having particles ingested into their jet engines. Aerosols even impact global climate. When present in sufficient amount and for a long enough time, aerosols can lower Earth's average temperature.

Some of the aerosol retrieval algorithms are based on the use of multiangle polarization measurements in the visible and near-infrared wavelengths from the polarization sensitive instruments. This algorithms allow retrieving the aerosol optical thickness and a parameter indicative of particle size [Waquet et al. 2009].Another approach is correlating reflected radiance for specific wavelengths with expected theoretical values. These different approaches are a consequence of the different nature and characteristics of aerosols (e.g carbon based, sulfur based, mineral based, sea spray etc.).

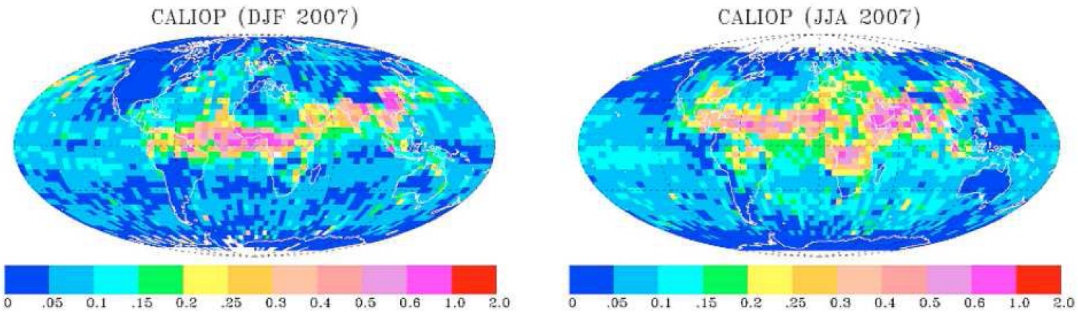

Figure 3.4: CALIPSO measurements of avearage aerosol optical depth in the visible/infrared in the cloud-free conditions in December-January-Ferbruary 2007 (left) and June-July-August 2007 (right). From [Hongbin et al. 2010].

Clouds are not treated as aerosols mainly because of historical reasons and their meteorological impact. They consist of aggregates of tiny water droplets and/or ice crystals in the atmosphere above the Earth's surface. Clouds play the uttermost important role in weather forecasting and their influence in human activities is enormous. Nevertheless, in the present work we will depart from this approach to clouds. We are interested in their optical properties only and not so much in their rainfall,convection mechanisms etc.

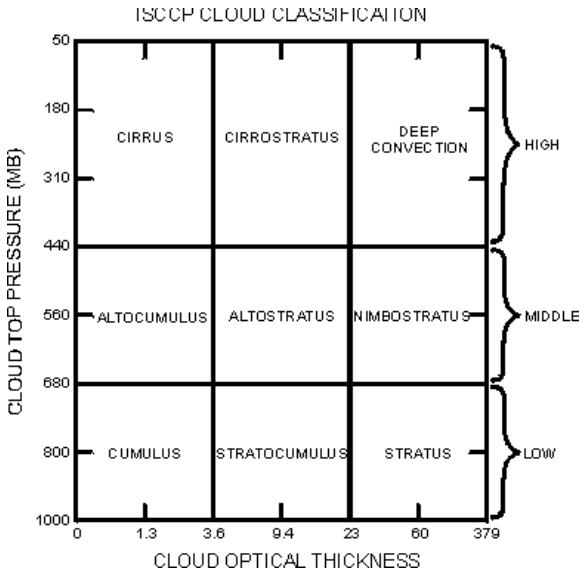

Figure 3.5: Usual cloud classification. From [ISCCP].

3.1.3 Scattering

The transmission of light through the atmosphere depends on two crucial processes: absorption and scattering. The Earth's atmosphere does not absorb directly the electromagnetic radiation under this work's scope. Uv and visible parts of the spectrum do not become perceivably absorbed in by photoelectric effect or such as they transverse the atmosphere [Penndorf 1955]. On the other hand, scattering plays a fundamental role in the EAS signal propagation through the atmosphere. We focus on two kinds of scattering:

Rayleigh Scattering

This kind of scattering deals with particles small compared to the wavelength. Which is the case of UV light and molecules.

In general if we let $u_0 = e^{-ikz+iwt}$ represent a electromagnetic wave transversing a medium (for simplicity in the z direction). Then the scattered wave is a spherical outgoing wave inversely proportional to the distance r [van de Hulst 1957]:

$$u = s(\theta, \phi)\frac{e^{-i\vec{k}\cdot\vec{r}+wt}}{i\vec{k}\cdot\vec{r}}u_0$$

Where we introduce the amplitude function (θ and ϕ being the usual spheric zenith and azimuthal angles). As a consequence we have:

$$I_{scattered} = \frac{s^2(\theta, \phi)}{k^2 r^2}I_0$$

The simplification introduced by the small size is that the particle may be considered to be placed in a homogeneous electric field $\vec{E}$.The particle's own field, caused by the polarization of the particle, modifies the electromagnetic field inside and near the particle. Then the polarization is proportional to this homogeneous field

$$\vec{p} = \eta\vec{E}$$

where η is the polarizability of the medium. The oscillating dipole radiates in all directions. The corresponding intensity for the scattered radiation (in gaussian units , time averaging the Poynting vector):

$$I = \frac{c}{2\pi}\vec{E}\cdot\vec{E}$$

For isotropic scattering the scattered field is obtained by the scattering tensor S which is proportional to $k^3\eta$ (see [van de Hulst 1957]):

$$I = \frac{(1 + cos^2\theta)k^4\eta^2}{2r^2} I_0$$
$$= \frac{I_0\eta^2}{r^2}\left(\frac{128\pi^5}{3\lambda^4}\right) \times \frac{3(1 + cos^2(\theta))}{4\pi}$$

where θ is the scattering angle, and the term in parenthesis is called the scattering cross section.

Mie Scattering

In this case the scattering particles are very large compared to the wavelength (e.g. water droplets inside clouds). Mie's theory of scattering deals with this type of scattering and has a strong dependence on the particle's geometry [van de Hulst 1957] and varies very little with wavelength.
For the special case of a mediu containing N spherical particles of radii a per unit volume (which is one of the common assumptions when dealing with clouds), the intensity of the emitted beam decreases in a distance l by a fraction $e^{\gamma l}$. Where:

$$\gamma = N\pi a^2 Q_{scat}(\lambda, m)$$

In this last equation Q_{scat} is the efficiency factor for the scattering which is a function of the wavelength and the refractive index m of the medium. Tables of Mie functions usually give this efficiency factors.

The amount of both fluorescence and Cherenkov signals reaching JEM-EUSO depends on the extinction and scattering of UV light in the atmosphere. Fraction of the signal due to the scattering in the atmosphere might be significant (tens of percent see section 1.2.4). Correct reconstruction of shower energy and of the type of the primary cosmic ray particle requires, therefore, information about absorption and scattering properties of the atmosphere. Extinction leads to the reduction of the overall intensity of the EAS signal as it propagates from the production region toward the detector. For the rest of this work we shall take the convention that the extinction is characterized by the extinction coefficient α defined as a product of the density of absorbing particles (molecules, water droplets, ice crystals, other aerosol particles) and the absorption cross-section per particle. The extinction coefficient is a function of the 3-dimensional position ($\vec{x}$) in the atmosphere and the wavelength. The reduction of the UV light intensity is by a factor

As can be seen in figure 3.6 the atmosphere absorbs below 1 % of UV radiation for wavelengths longer than 340 nm, due to the ozone contents of the upper atmosphere.

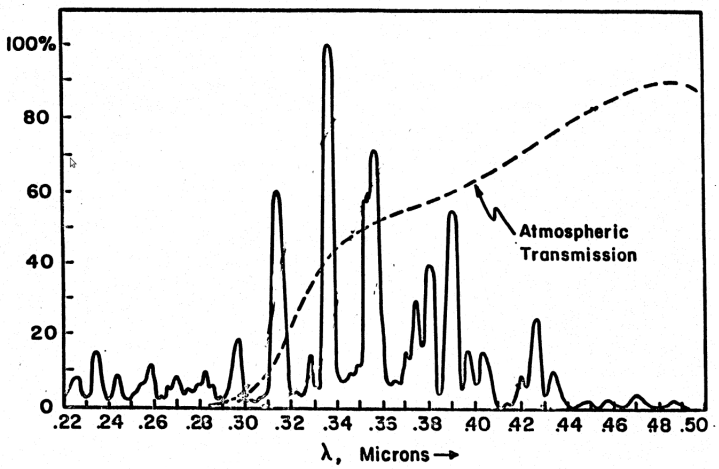

Figure 3.6: Fluorescence spectra of air in the UV region. Atmospheric transmission is shown as a dashed line. Modified from [Bunner 1967]

3.1.4 UV phenomena

Every space borne experiment will have to observe the conditions of the atmosphere in the field of view of the detector making use of a state-of-art atmospheric monitoring system. Besides from the EAS fluorescent signal, there are other significant phenomena that are worth mentioning.

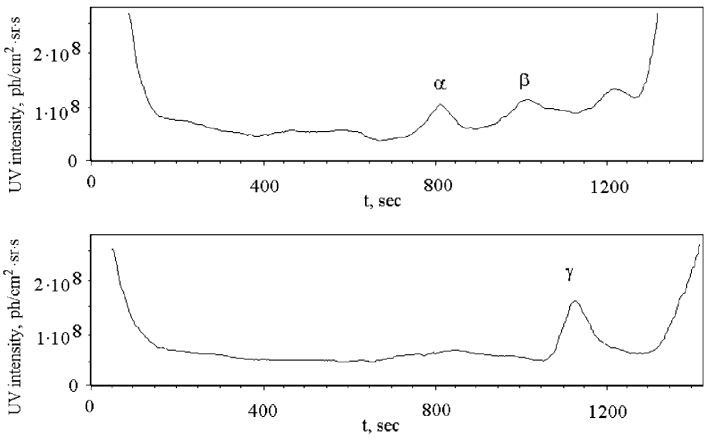

Figure 3.7: Examples of UV intensity recorded at night side of the Earth by TATIANA satellite. Peaks occur when the satellite crosses Mexico City (α) and Houston (β) and Los Angeles (γ) in the bottom panel (from [Garipov 2005]).

Nightglow and lighting

The nightglow in the wavelength band 330÷400 nm is dominated by the emission from oxygen molecules in Herzberg I band around the boundary region at an altitude of 95 km between mesosphere and thermosphere; this emission is reported to have a strong correlation with the green line (557.7 nm) of atomic oxygen [57]. The 40 km width stripes of the green emission appear to move when observed from ground ; it is believed that these stripes are produced by gravity waves formed in the troposphere and propagated to the upper atmosphere. This propagation of gravity waves may affect the transfer of energy and angular momentum to the mesosphere and thermosphere.

Lightning-emitted optical flashes and electromagnetic waves have been successfully measured by satellites. Of special interest are the Narrow Bipolar Events (NBEs)area and Cloud-to-Ground (CG) events. NBE is a discharge events that have a time constant less than 1 μ, a discharge path length of the order of 100 m, and radiation energy greater than 100 kW. It is reported that NBE is only observed at the initiation phase of the negative CG discharges. From the intensive satellite and ground-based observations it is also reported that the NBE is strongly related with the cloud-to-cloud discharges occurring at the 10 ÷ 20 km altitude. Recently is has been suggested that NBE would reasonably be explained by the runaway breakdown triggered by EAS that consists of mainly 3 MeV relativistic electrons. Thus, the wavelength of the optical emission related to NBE is not in the visible range but in the near UV range (330÷400 nm) same as EAS.

Transient Luminous Events (TLEs)

This events associated with intense energy transfers between atmospheric layers. All of them are associated with thunderstorm activity and are of electromagnetic nature. There are different types of TLEs:

Sprites

Sprites are luminous flashes, appearing at altitudes of 40-90 km, above large thunderstorm clouds. Below a bright head like region, blue tendril-like filamentary structures often extend downward to 40 km. This structure shows extremely interesting and as yet not fully explained phenomenon of merging streamers, which form bright spherical structures – the beads. Measurements of microsecond time resolution may help to explain the mechanism behind the phenomenon. Sprites usually occur in groups of a few. The duration of sprites is of the order of ms. The optical intensity of sprite clusters is comparable to a moderately bright aurora arc. The optical energy is roughly 10-50 kJ per event.

Elves

Elves are discs of light expanding at a speed close to the speed of light. They are the most common of the TLEs . Elves are initiated by an electromagnetic pulse caused by the cloud to ground discharge. They occur at altitudes of 85–95 km and their average diameter is about 200 km.

Halos

Halos are diffuse bright regions detected above the head of a sprite. They occur at altitudes of 75–85 km and have a diameter of about 100 km. Their occurrence rate is measured to be similar to that of the sprites.

Blue jets

Optical ejections from the top of the electrically most active regions of thunderstorms. Special case are the Giant Blue Jets, which can reach the ionosphere altitude. Their estimated optical energy is about 4 kJ, a total energy of about 30 MJ. Their appearance rate is much lower than that of sprites.

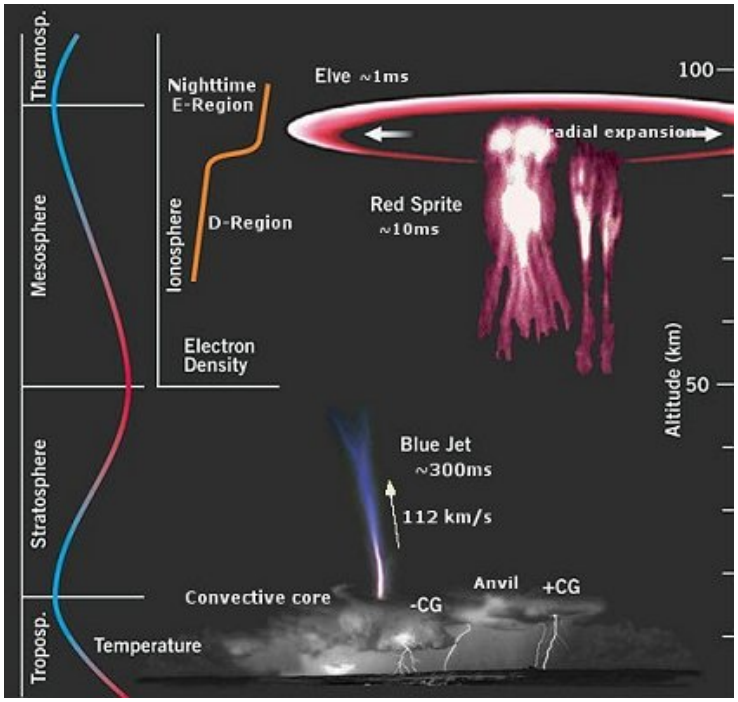

Figure 3.8: Transient Luminous Events.

3.2 Satellite data

As it is now hopefully clear, space borne measuring of atmospheric conditions will be a fundamental aid in the present work's pursue of its objectives (see chapter 2.1). We shall focus our attention on two distinct satellite missions. This two databases provide the cloud data that will be analyzed in the following chapters.

3.2.1 MERIS

Overview

The MEdium Resolution Imaging Spectrometer Instrument MERIS is a 68.5°field-of-view push-broom imaging spectrometer on board the ENVISAT satellite [MERIS PH], that measures the solar radiation reflected by the Earth, at a ground spatial resolution of 300 m, in 15 spectral bands, programmable in width and position, in the visible and near infrared wavelengths (see figure 3.9).

The primary mission of MERIS is the measurement of **sea colour** in the oceans and in coastal areas. Knowledge of sea colour can be converted into a measurement of chlorophyll pigment concentration, suspended sediment concentration and of atmospheric aerosol loads over water. For example:

- understanding the ocean carbon cycle
- understanding the thermal regime of the upper ocean
- the management of fisheries & coastal zones
- climate studies
- ocean dynamic

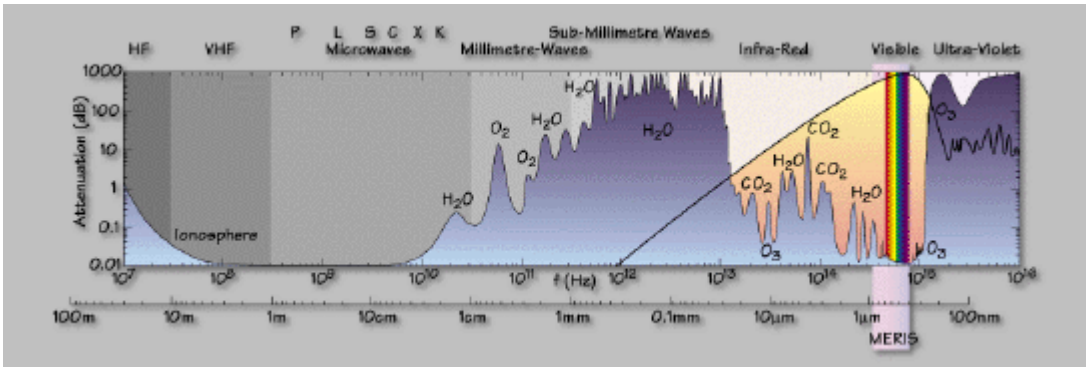

Figure 3.9: MERIS measuring window in the electro magnetic spectrum. Emission lines for some atmospheric and organic components are shown

No.	Band centre (nm)	Band width (nm)	Applications
1	412.5	10	Yellow substance and detrital pigments
2	442.5	10	Chlorophyll absorption maximum
3	490	10	Chlorophyll and other pigments
4	510	10	Suspended sediment, red tides
5	560	10	Chlorophyll absorption minimum
6	620	10	Suspended sediment
7	665	10	Chlorophyll absorption & fluorescence reference
8	681.25	7.5	Chlorophyll fluorescence peak
9	708.75	10	Fluorescence reference, atmosphere corrections
10	753.75	7.5	Vegetation, cloud, O_2 absoption band reference
11	760.625	3.75	O_2 R- branch absorption band
12	778.75	15	Atmosphere corrections
13	865	20	Atmosphere corrections
14	885	10	Vegetation, water vapour reference
15	900	10	Water vapour

Figure 3.10: MERIS's spectral bands ($\Delta\lambda < 10nm$).

MERIS is a passive imaging spectrometer, which performs simultaneously spatial and spectral imaging of the Earth, by looking in the nadir direction. The most outstanding characteristics of MERIS, detailed below, are: MERIS is a push-broom instrument.

- The InFOV is $68° + 1/0.1°$. Which equates to a swath width of 1150 km centered

around the subsatellite point (*nadir*).

- The 15 observed spectral bands are all programmable in position and width.
- Two spatial resolutions can be selected.
- On board processing can be performed on the image data.
- The polarization sensitivity of MERIS is very low. (this is important for aerosol identification).
- MERIS has a high radiometric and spectrometric performance.
- MERIS allows global coverage of the Earth in 3 days.
- It has an average altitude of 777.5 km and an orbital period of 100.2 minutes.

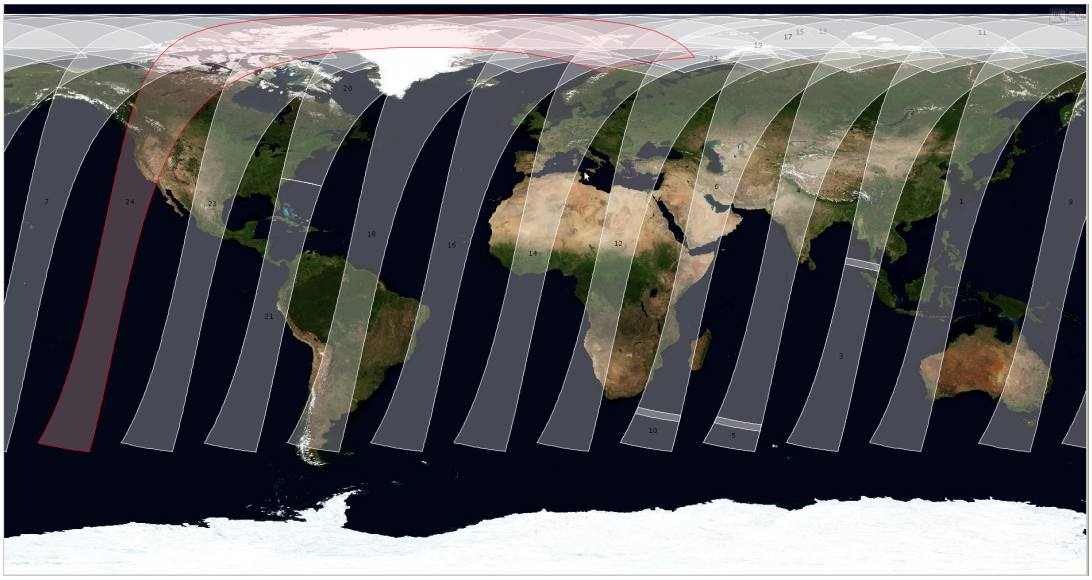

Figure 3.11: MERIS coverage of 1 complete day acquired data.

Relevant MERIS's data products & basic algorithms: Cloud's top pressure, optical thickness and albedo

The ENVISAT nomenclature of the products delivered to the public describes three types of processing levels:

- Level 1B are images resampled on a path-oriented grid, with pixel values having been calibrated to match the Top Of Atmosphere (TOA) radiance.

- Level 2 are images deriving from the level1B products, with pixel values having been processed to get geophysical mesurements.
- Level 3 are synthesis of more than one MERIS products (and possibly external data) to display geophysical measurements for a time period.

MERIS data are provided at these 3 different levels of processing and at 3 different spatial resolutions Full, Reduced and Low.

For the same image, a Full-Resolution (FR) image has 4 ×4 more points (pixels) than the same image in Reduced Resolution (RR), and an RR image has 4 ×4 more points (pixels) than the same image in Low Resolution (LR). Accordingly, a pixel in an FR image represents an area of 260 m ×290 m, in an RR image an area of 1,040 m ×1,160 m, and in LR an area of 4,160 m ×4,640 m.

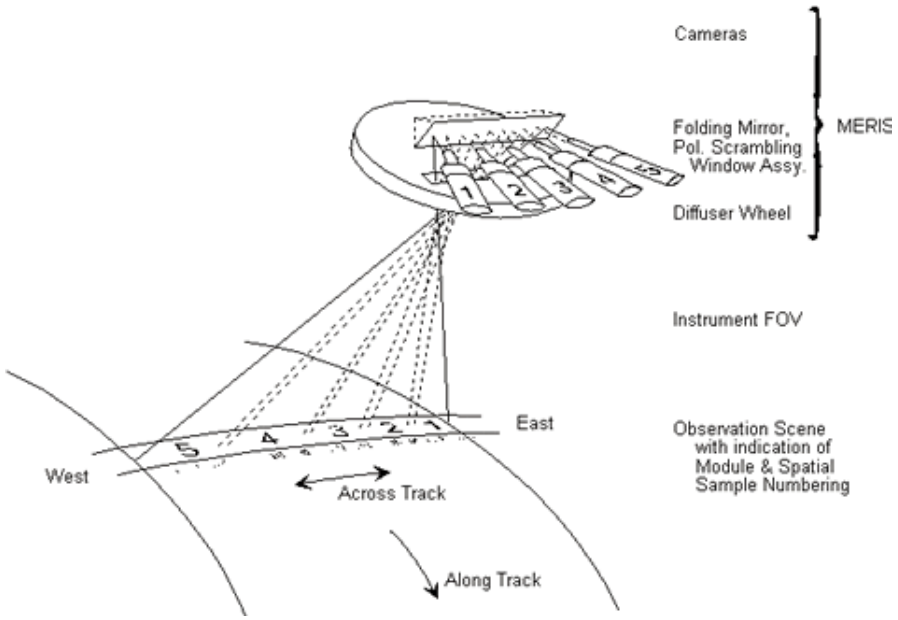

Figure 3.12: Depiction of MERIS observation principle.

For this work's purpose we focus in the MER_RRC_2P (Level 2 reduced resolution) data products which contains the extracted cloud thickness and Water Vapor (non-Meteo users). This files contain the following information per geographically specified pixel:

- Water Vapor.
- Cloud optical thickness

- Cloud types (based on the ISCCP convention, see figure 3.5).

The cloud albedo δ_c and cloud optical thickness τ are estimated from measurements of the MERIS channel centred at $\lambda = 753.75nm$. An adequate algorithm is established to transform the radiance measurements into hemispherical quantities by integration over viewing angles, since clouds do not reflect the sunlight isotropically. The algorithm suggested here accounts for the angular distribution of reflected solar radiation by radiative transfer simulations. The radiative transfer model MOMO (Matrix Operator Model) is used to solve the forward problem, i.e. the derivation of satellite sensor signals (radiances) by simulating the transfer of solar radiation through the atmosphere for given parameters. Additionally, MOMO calculates the spectral albedo at the atmospheric model layer boundaries. Inferring the optical properties from measured satellite radiances is called the inverse problem. This problem will be tackled by a polynomial approach where the cloud albedo and optical thickness are related to a polynomial function of the radiance to be measured. In order to improve the algorithm, the selection of the coefficients for polynomials depends on parameters that are specified a priori, either from external data or empirically derived from climatological data sets. This includes surface albedo as the most important parameter [MERIS ATBD].

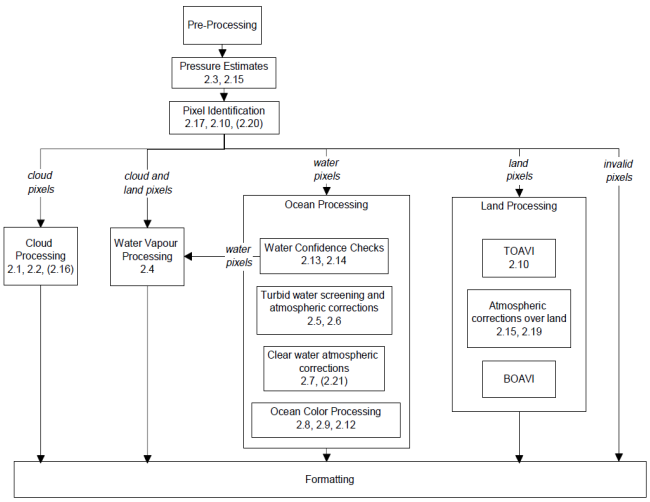

(a)

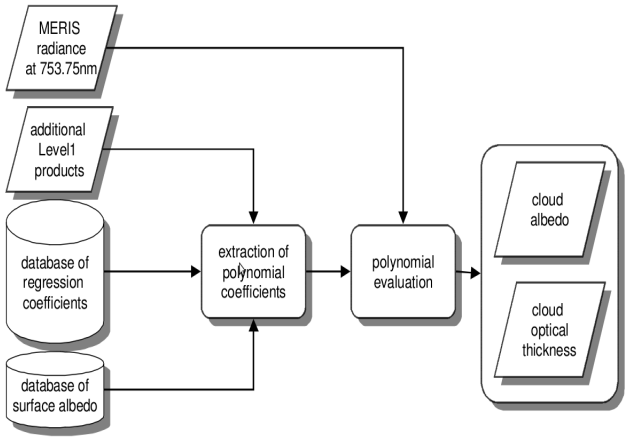

(b)

Figure 3.13: Depiction of MERIS data flow.

The most commonly used techniques for the remote sensing of atmospheric properties are based on Look Up Tables or simple regression methods. The sunlight reaching the cloud top, is backscattered and a part finally reaches the sensor on board a satellite. For a well mixed atmospheric gas like oxygen and a known vertical profile of the pressure and the temperature the penetrated air mass can be estimated by radiance measurements within an absorption band. For monochromatic light in a non-scattering atmosphere the relation between the amount of absorption and the penetrated air mass can be described by Lambert's law. However, this simple approach is not sufficient because it does neither include scattering of radiation inside and outside the cloud nor describes the absorption of non-monochromatic light correct. The impact of micro physical cloud properties, varying cloud optical thickness, surface albedo as well as the observation geometry on the radiances can be investigated by radiative transfer simulations only. The cloud top pressure retrieval algorithm dedicated for MERIS uses neural networks, since these are capable to represent complex multidimensional relationships[MERIS ATBD].

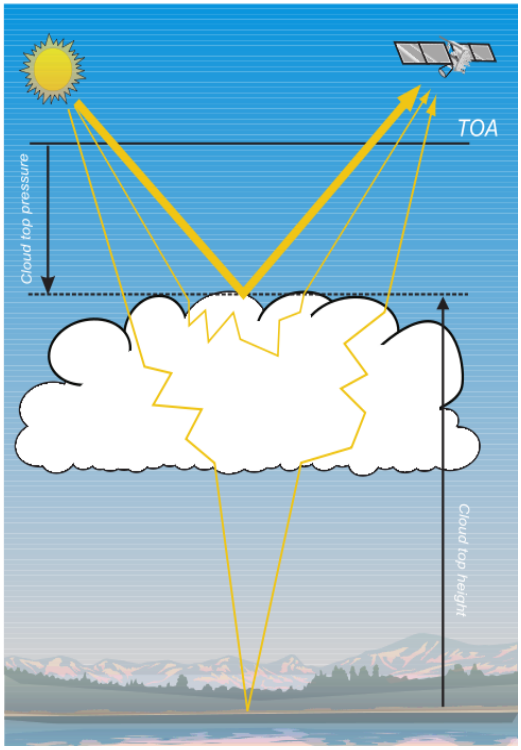

Figure 3.14: Illustration of the principle of the cloud top pressure detection using absorption of solar radiation due to well mixed atmospheric gases. Ancillary data (theoretical and measured) are then used in combination to estimate cloud's top height.

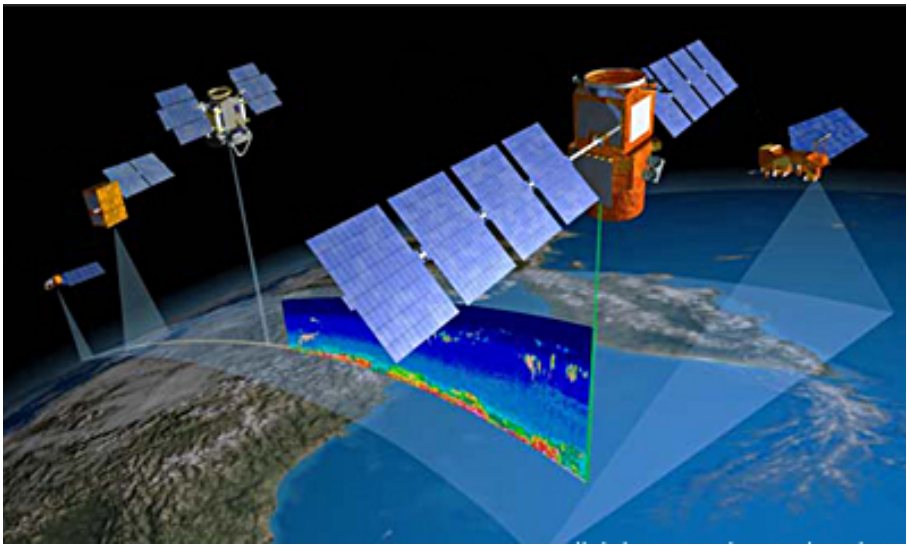

Figure 3.15: Artist conception of CALIPSO's measurements while flying along the *Afternoon train*.

3.2.2 CALIPSO

Overview

The NASA's Cloud Aerosol Lidar and Infrared Pathfinder Satellite Observations (CALIPSO) forms part of the A-train satellite constellation [Stephens et al. 2002]. A group of satellites which carry out standalone but complimentary atmospheric measurements.

The CALIPSO mission builds on the experience of LITE, which flew a three-wavelength lidar on the space shuttle in 1994 [Vaughan et al. 2004]. CALIPSO enhances measurement capabilities with a payload consisting of a two-wavelength polarization-sensitive lidar, and two passive imagers operating in the visible and infrared spectral regions. Data from these instruments are used to measure the vertical distributions of aerosols and clouds in the atmosphere, as well as optical and physical properties of aerosols and clouds.

CALIPSO's overall objective is to improve the representation of aerosols and clouds in models, including climate models, weather forecast models, and air quality models.

The CALIPSO lidar, CALIOP, provides global, vertically-resolved measurements of clouds/aerosol distribution and extinction coefficients, with an ability to perform

height resolved discrimination of aerosol into several types. Unlike the current generation of space-based remote sensing instruments, CALIOP can observe aerosol over bright surfaces and beneath thin clouds as well as in clear sky conditions. Cloud data from CALIOP are incorporated into the IIR retrieval algorithm to reduce uncertainties in the retrieval of cloud emissivity and particle size. It perfomrs a sun-synchronous orbit at altitude of 705 kilometers, with 98.2-degree inclination. It orbits Earth once every 99 minutes and repeats the same ground track every 16 days.

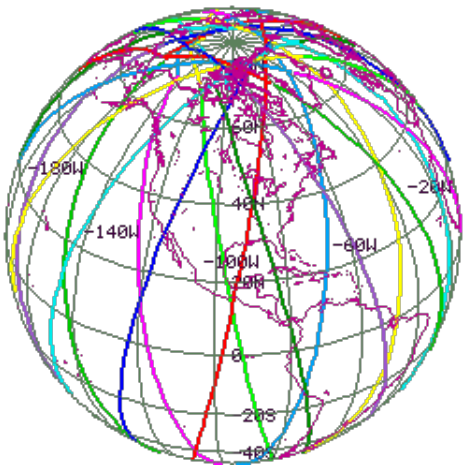

Figure 3.16: CALIPSO's ground tracks from one whole day of data acquisition.

CALIPSOS's main feature is to produce "PET scans" , with information concerning altitude and concentration of clouds and aerosols. It uses highly sophisticated algorithms to correctly interpreter the backscattered signal from each laser pulse. The vertical structure of the atmosphere is then saved to different data products for their further analysis.

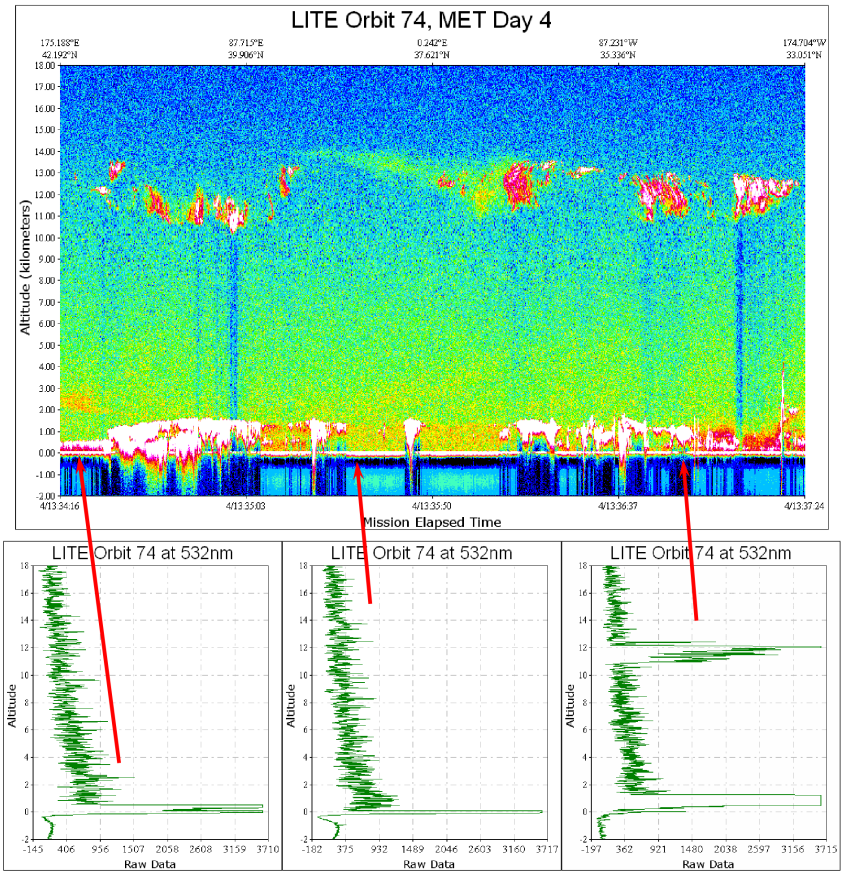

Figure 3.17: CALIOP measuring principle. The time domain backscattered signal is transformed into atmospheric features with distinct vertical structure.

The fundamental equation to be solved in these kind of studies is the *Lidar equation* which can be written as:

$$P(r) = \frac{1}{r^2} E_0 \xi \beta(r) T^2(r)$$

where:

- r is the range from the satellite to the sampled volume,
- $P(r)$ is the measured signal after background subtraction and artifact removal,
- E_0 is the average laser energy for the single-shot or composite profile,
- ξ is the lidar system parameter,

- $\beta(r)$ is the volume backscatter coefficient at range r,
- $$T(r) = e^{-\int_0^r \sigma(r')dr'}$$
  is the one-way transmittance (i.e., signal attenuation) from the lidar to the scattering volume at range r, and
- $\sigma(r)$ = volume extinction coefficient at range r.

Relevant CALIPSO's data products & basic algorithms: Cloud's extinction coefficient

CALIPSO's data[1] products are organized a follows:

1. Level 0: Reconstructed unprocessed instrument/payload data at full resolution; any and all communications artifacts (e.g. synchronization frames, communications headers) removed.
2. Level 1A: Reconstructed unprocessed instrument data at full resolution, time-referenced, and annotated with ancillary information, including radiometric and geometric calibration coefficients and georeferencing parameters (i.e., platform ephemeris) computed and appended, but not applied, to the Level 0 data.
3. Level 1B: Level 1A data processed to sensor geolocated and units.
4. Level 2: Derived geophysical variables at the similar resolution and location as the Level 1 source data.
5. Level 3: Geophysical variables are mapped on uniform space-time grids, usually with some completeness and consistency.
6. Level 4: Model output or results from analyses of lower level data, e.g., variables derived from multiple measurements.

We shall focus our attention in the Lidar Level 2 Cloud Profile data product. It contains cloud profile data and ancillary data. The cloud profile product is produced at 5 km horizontal resolution and is written in HDF. Also, the 1064 calibration scheme assumes that both the extinction and the backscatter from clouds are spectrally independent. Consistent with this assumption, extinction and backscatter profiles will be reported for clouds only at 532 nm. Additionally, it is important to note that the aerosol profile product extends upward to 30.1 km, while the cloud profile product ceases at 20.2.

The major categories of the cloud profile data product are:

[1]These data were obtained from the NASA Langley Research Center Atmospheric Science Data Center.

- Backscatter Profile Data
- Depolarization Profile Data
- Extinction Profile
- Ice Water Content
- Ancillary Profile Data

The retrieval of particulate extinction from measurements by space-borne elastic-backscatter lidars such as CALIOP faces a number of challenges not encountered in the analysis of measurements made by ground-based lidars. These difficulties are the result a combination of factors, including the large distances between the lidar and the targets of interest the high speed at which the lidar sweeps across the target space ($\sim 7km/s$), constraints placed on the pulse energy of the laser transmitter, the relatively low firing rate of the laser (20 Hz) relative to the velocity of the satellite, and vertical and horizontal variations in the composition of the layers being measured. Taken together, these factors can reduce the measurement signal-to-noise ratio (SNR) within clouds and aerosols to levels where the uncertainties in the retrieved data products become unacceptably high.

A key aspect of CALIPSO analysis system is that it uses an innovative nested multi-grid averaging scheme to process a composite lidar 'scene'. Scenes are segments of what are commonly referred to as CALIPSO curtain files, which, as illustrated in Figure 3.2.2, are two dimensional, height versus along-track distance, vertical swaths through the atmosphere. Through this approach, the processing system is able to identify and extract high SNR profile data from each scene and derive optical properties of clouds and aerosol layers. The CALIOP Level 2 processing system is composed of three modules, which have the general function of detecting layers, classifying these layers by type, and performing extinction retrievals. These three modules are the Selective Iterated BoundarY Locator (SIBYL) and Scene Classifier Algorithm (SCA), and Hybrid Extinction Retrieval Algorithms (HERA), respectively.

Profile Vertical Resolution

Altitude Region		Vertical Resolution, meters	Samples per Profile
Base, km	Top, km		
-0.5	8.2	60	145
8.2	20.2	60	200
Total			**345**

Figure 3.18: Lidar Level 2 Cloud Profile data product structure

Before the retrieval of extinction coefficients can be performed, clouds must be located and discriminated from aerosol, and water clouds must be discriminated

from ice clouds. In the Level 2 algorithms, the Selective Iterated BoundarY Locator (SIBYL) detects layers, the Scene Classification Algorithm (SCA) classifies these layers, and the Hybrid Extinction Retrieval Algorithms (HERA) perform extinction retrievals. Although the location of cloud and aerosol layers and the determination of cloud ice/water phase are necessary precursors to extinction retrieval, these data products are of interest in their own right.

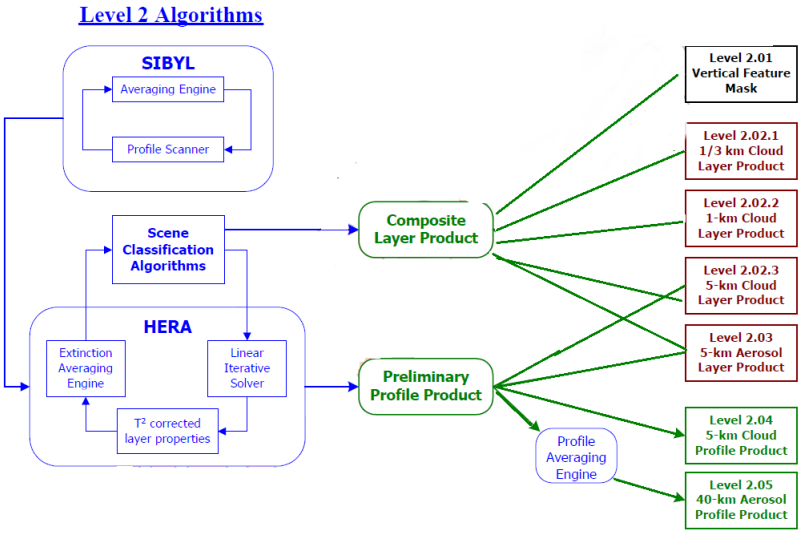

Figure 3.19: Production Pathway for Level 2 Cloud Profile data products.

Chapter 4

Earth's cloud coverage and its implications in exposure.

Cloud coverage, cloud top height and cloud optical thickness are some of the most relevant cloud properties with respect to EAS detection. We begin our discussion focusing on global observations of cloud's properties. This will prove useful to statistical discussions of space borne mission's exposure or duty cycle.

The International Space Station's Orbital properties

For the scope of the present work, this studies here presented would not be complete without an analysis using the ISS orbital characteristics and their consequences on JEM-EUSO's science. Therefore, we shall recall the ISS's orbital characteristics and what they imply.

The ISS performs an orbit with the following characteristics:

orbital period	92.19 minutes
inclination	51.64°.
average altitude (a.s.l.)	392.5 km
average orbit velocity	7.679 km/s
eccentricity	.0011968

For the correct simulation of the ISS orbit some definitions and conventions were taken, namely [J. Larson & James R. Wertz]:

Inclination is the angular distance between a satellite's orbital plane and the equator of its primary . An inclination of zero degrees indicates an orbit about the primary's equator in the same direction as the primary's rotation, a direction called prograde (or direct). An inclination of 90 degrees indicates a polar orbit. An inclination of 180 degrees indicates a retrograde equatorial orbit.

Periapsis is the point in an orbit closest to the primary. The opposite of periapsis, the farthest point in an orbit, is called apoapsis. Periapsis and apoapsis are usually modified to apply to the body being orbited, e.g. perigee and apogee for Earth. The argument of periapsis is the angular distance between the ascending node and the point of periapsis (see Figure 4.1). The time of periapsis passage is the time in which a satellite moves through its point of periapsis.

Nodes are the points where an orbit crosses a plane, such as a satellite crossing the Earth's equatorial plane. If the satellite crosses the plane going from south to north, the node is the ascending node; if moving from north to south, it is the descending node. The longitude of the ascending node is the node's celestial longitude. Celestial longitude is analogous to longitude on Earth and is measured in degrees counter-clockwise from zero with zero longitude being in the direction of the vernal equinox .

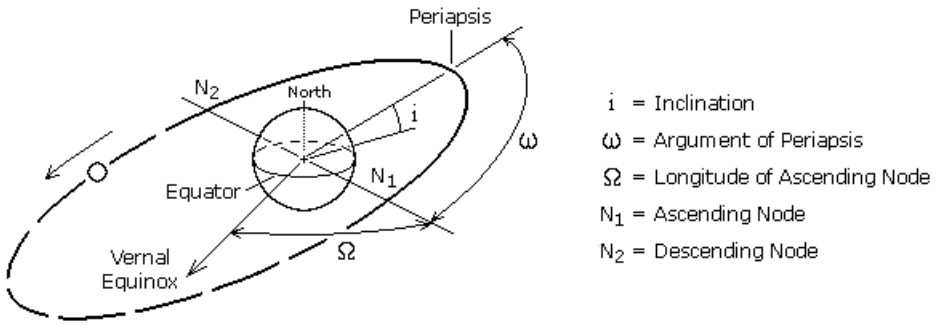

Figure 4.1: Orbital elements illustration. (modified from [Bruening])

We recall the solution to the equation for the path of a particle moving under the influence of a central force whose magnitude is $\propto \frac{1}{r^2}$ [Marion-Thorton]:

$$r = \frac{a(1-e^2)}{1+ecos(\nu)} \tag{4.1}$$

where:

- r is the distance between the particle and the force center.
- ν called the *true anomaly*; it is the angular distance between the particles position the periapsis point.
- a is the major semi-axis.

- e is the eccentricity.

The gravitational forces of the Sun and the Moon cause periodic variations in all of the orbital elements. Also the potential generated by the non-spherical Earth causes periodic variations in all the orbital elements. For a potential function of the Earth, we can find a satellite's acceleration by taking the gradient of the potential function. The most widely used form of the geopotential function depends on latitude and geopotential coefficients, J_n, called the zonal coefficients. However, for low Earth orbits such as the ISS's orbit, the dominant effects are secular variations in longitude of the ascending node and argument of perigee because of the Earth's oblateness. These are represented by the J_2 term in the geopotential expansion.

This rates of change can be numerically expressed as [Kozai 1969]:

$$\omega_{J_2} = -1.5nJ_2 \left(\frac{R_E cos(i)}{a(1-e^2)} \right)^2$$

$$\Omega_{J_2} = 0.75nJ_2 \left(\frac{R_E(4-5sin^2(i))}{a(1-e^2)} \right)^2$$

In this last expression: n is the mean motion in degrees/day, J_2 has the value 0.001082639, R_E is the Earth's equatorial radius, a is the semi-major axis in kilometers, i is the inclination, e is the eccentricity, and ω_{J_2} and Ω_{J_2} are in degrees/day. Atmospheric drag also plays an important role but this effect is compensated by maned missions that vary in purpose and strength. This can be individually accounted for, but from a general perspective they can't be statistically simulated.
With this brief analysis we were able to follow up the expected trajectory of the ISS. This was used to calculate the latitude "exposure" of the ISS(see Figure 4.2) .

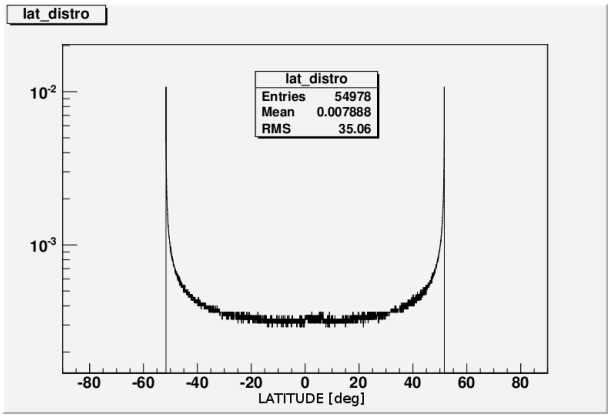

Figure 4.2: Latitude distribution of the ISS ($\frac{\Delta lat}{\Delta t}$).

4.1 Statistical studies

4.1.1 Cloud coverage effect in different scenarios

MERIS analysis

In the scope of this work, the biggest 2 dimensional dataset corresponds to MERIS (see Chapter 3). Therefore we made studies regarding daily cloud coverage in the whole of the Earth's surface. We intend to asses the effect of the Earth's cloud coverage. MERIS's spatial resolution is of 1040m ×1200m which is quite close to JEM-EUSO's pixel resolution. Bearing this in mind, we simulated shower profiles for different energies (19.8 <log(E/eV)< 21) and zenith angles ($30° < \theta < 80°$), and inserted them randomly inside a field of view (FoV) defined inside one of MERIS "cloud scenes". This was carried out for different latitude in latitude span of the ISS.

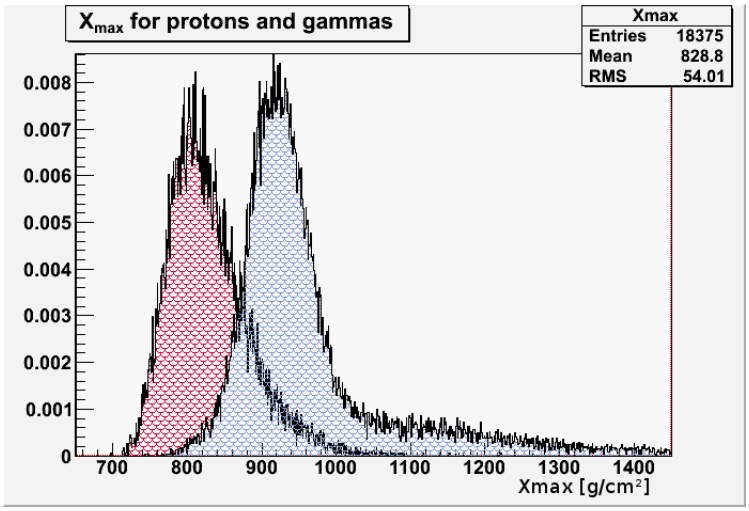

Figure 4.3: Histograms for X_max of our simulated showers. Protons are shown in red and gammas in blue.

We defined 3 criteria for different reconstruction scenarios. This are a first approach to the minimum conditions any EAS will need in order to be reconstructed. This conditions are summarized as follows:

- *Xmax condition*: Xmax above cloud top. (the minimum visible portion of the track was fixed by the MERIS resolution of 1 km).
- *Track condition*: Presence of a visible shower track inside the FoV. Track must be more than 5 of an 11 adjacent pixels centered on Xmax, so that a large

enough portion of the track is seen around Xmax. At least two cloud free pixels are located at any side of Xmax.

- *Time condition* A more realistic criteria. It is the same as the track condition but applied to temporal pixels, to GTU-bins of 2.5 μs

Results of this studies are shown in Fig. 4.5. Roughly speaking we concluded that a fraction of 0.3 of the total showers are not reconstructible due to the presence of thick (i.e. $\tau > 1$) clouds. This figure has to be understood as an unavoidable diminishing of the mission's duty cycle, regardless of its AM system capabilities.

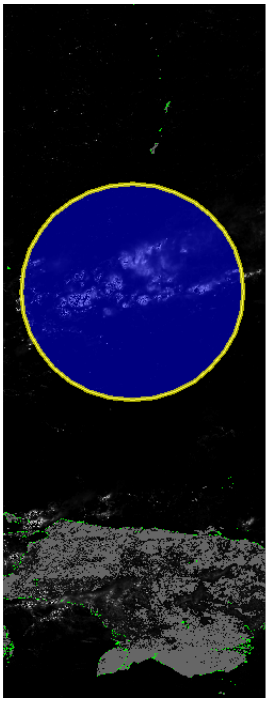

Figure 4.4: A JEM-EUSO's FoV superposed over a "cloudy portion" MERIS data near Papua New Guinea in the south Pacific ocean. In contrast there are almost no clouds outside the FoV for this example.

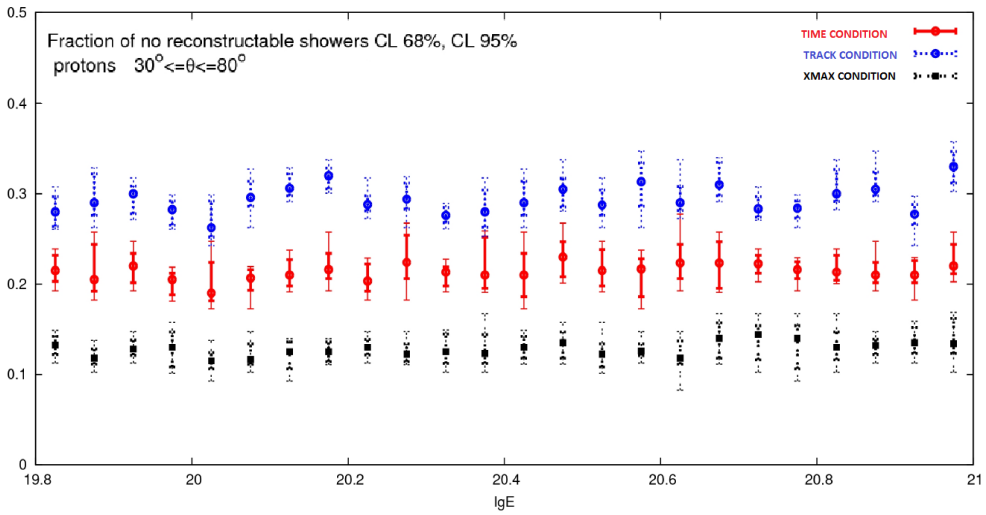

Figure 4.5: Fraction of lost events due to the presence of clouds

4.1.2 Clouds' τ distribution

Though the previous analysis aids in the overall coverage, MERIS data has a very coarse approximation to the cloud's vertical structure, i .e only the cloud's top pressure is reported. Cloud's top pressure is then transformed to height using an atmospheric model (the U.S. Standard). Besides there is no information available for optically thin clouds.

We now turn our attention to CALIPSO data. Since CALIPSO data has no equivalent swath coverage such as MERIS. We used 703 CALIPSO "curtain files" to overcome this swath reduction. This files contain cloud scenarios distributed throughout a whole year (2009). We will refer to this database of 703 files, as our CALIPSO's *one year data*.
We also used the ISS latitude distribution along this data. We used this distribution in order to sample portions of the Earth's surface that will be observable from a experiment flying on board the ISS.

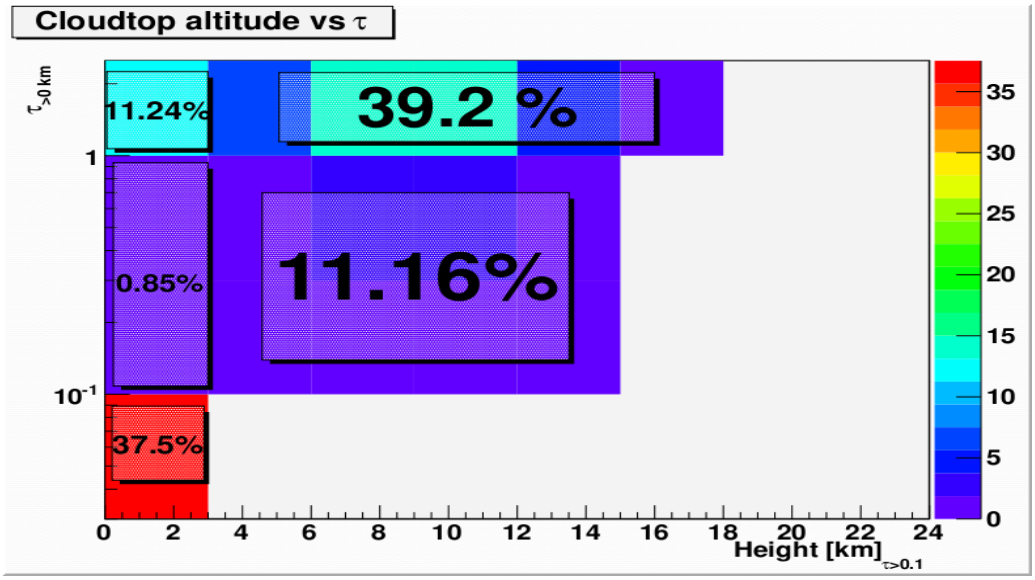

Figure 4.6: Earth coverage of clouds with different values of τ and their respective heights a.s.l in [km]

Before proceeding with the results hereby presented, the following definitions are in order:

- **Cloud's optical depth/thickness** $\tau = \int \alpha(x)dx$
  This is the main parameter we shall be discussing. The integral is taken for a given line of sight. It is performed upwards from some specified height up to to infinity, unless otherwise specified. In this formula $\alpha(x)$ is the extinction coefficient $[km^{-1}]$
- **Optically thick cloud**
  Any cloud whose vertical value of τ fulfills $1 > \tau$.
- **Optically thin cloud**
  Any cloud whose vertical value of τ fulfills $0.1 < \tau < 1$.
- **Cloud's top**
  The maximum value of altitude from where the value of vertically integrated τ fulfills $0.1 < \tau$.

Results from this study are shown in figure 4.6. We can highlight that low height (less than 3 km), clear sky zones and optically thin clouds represent $\sim 60\%$ of the sky. This figure could be wrongly interpreted as completely clear sky by an infrared survey,or possibly as a very low cloud. Hence underestimating the real value of the

energy of the EECR. This could jeopardize the scientific goals of the mission if no action is taken to tackle the problem. Fortunately missions as JEM-EUSO, rely on multiple monitoring techniques to avoid this issue. Nevertheless this techniques have to prove that they will be able to avoid the effects here quantified.

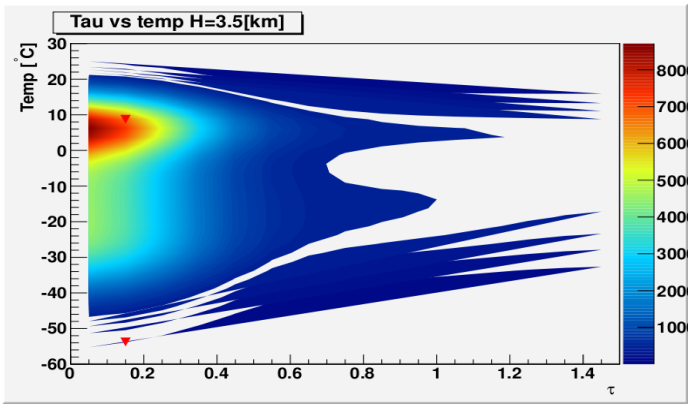

Figure 4.7: One of the many test carried out to establish a more clear connection between cloud temperature and optical thickness. Although no clear relationship can be inferred for this 2 variables, this kind of information would help fill in the "look up" tables needed for a a correct interpretation of the infrared camera data.

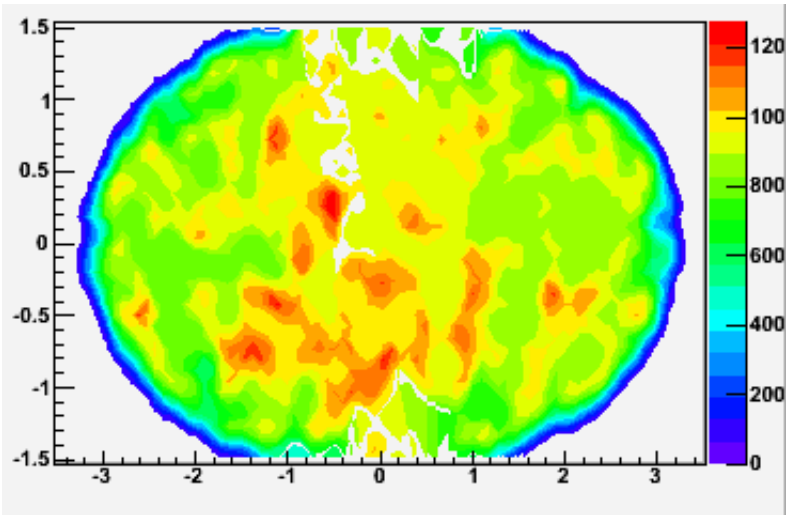

Figure 4.8: Aitoff projection of the sky . Color code indicates the value of X_{max} for γ-showers injected with an spectral index of 2.7.

4.1.3 Hadron and photon discrimination.

Extreme energy gammas are subject to photon splitting due to interactions with the Earth's magnetic field. This interaction is not present in proton showers. The detectable effect of this process is a change in the slant depth of EAS for gammas. Since the Earth's magnetic field is not homogeneous there are important geographical variations in the measured maximum depth (X_{max})(see Figure 4.8). This variations can lead to an erroneous conclusion about the EAS's primary. In other words there is a probability of confusing between the two primaries.

We inserted proton and gamma showers isotropically around the Earth's surface. Afterwards we estimated the probability of discerning between a proton(hadron) initiated shower and photon initiated shower. For this we used the expected value o X_{max} but with a density modulated by the ISS's longitude exposure. We carried out this such study for the whole globe, results are shown in figure 4.9. As it can be seen the South Atlantic Anomaly (SAA) appears as "source" for this confusion. This must be linked with the previous study of the ISS latitude exposure. As it can be seen the ISS spends roughly 50% of the time in these southern latitudes. Nevetheless, the SAA spans roughly from -90^{circ} to 40^{circ} in longitude, reducing the total amount of time in this region to 18%.

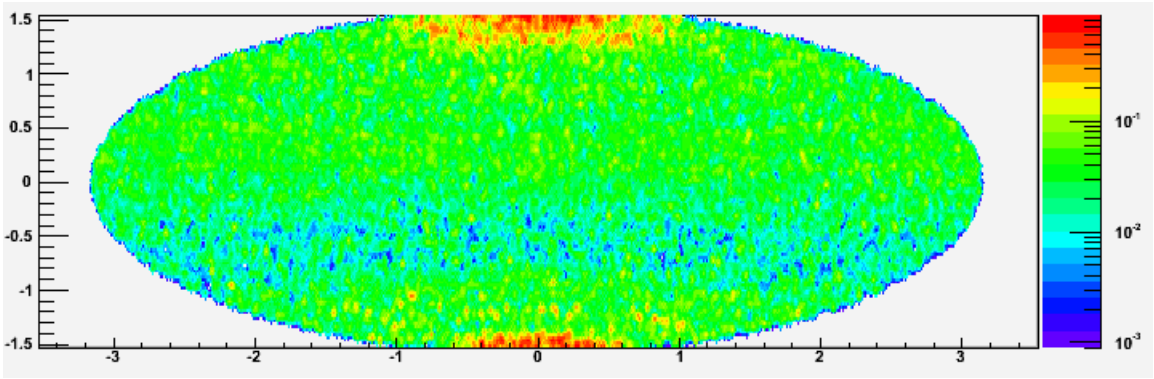

Figure 4.9: Aitoff projection of the sky . Color code indicates the probability to discern between a hadron initiated shower and a photon initiated shower.

Chapter 5

Clouds' vertical structure and its effects over EAS reconstruction

5.1 False-positive & false-negative detection simulation.

As a first approach we investigated what would be the effects in optical thickness determination due to the orbiting detector's natural displacement along its orbit. Our first approach was the must simple scenario. Let us assume that an EAS or a portion of it develops directly beneath the detector . The EAS would then be recorded by the detector, but it takes 1 second for the AM system to probe the EAS area. Therefore, probing a different portion of the atmosphere. The idea behind this measurement is depicted in figure 5.1. The possible cases can be resumed as follows:

	Real cloud present	Real cloud absent
Detected cloud	Cloud is "big enough"	Clouds are present in the lidar's *l.o.s.*
Undetected cloud	Cloud is "too small"	Mostly clear sky scenario

We concerned ourselves with the following question: how often would we retrieve fictitious informations due to this delay in the atmospheric probing? We used our *one year data* (see previous chapter) to make a statistical study. We simulated the passage of the ISS along its track with the atmospheric data in those files. Then for each ground pixel we retrieved the actual value of the vertically-integrated τ and compared this value with that of a randomly selected nearby pixel. This selection was made after displacing the ISS for one second (lag) and within a fixed uncertainty in the line of sight (δ). Our results are shown in figure 5.2

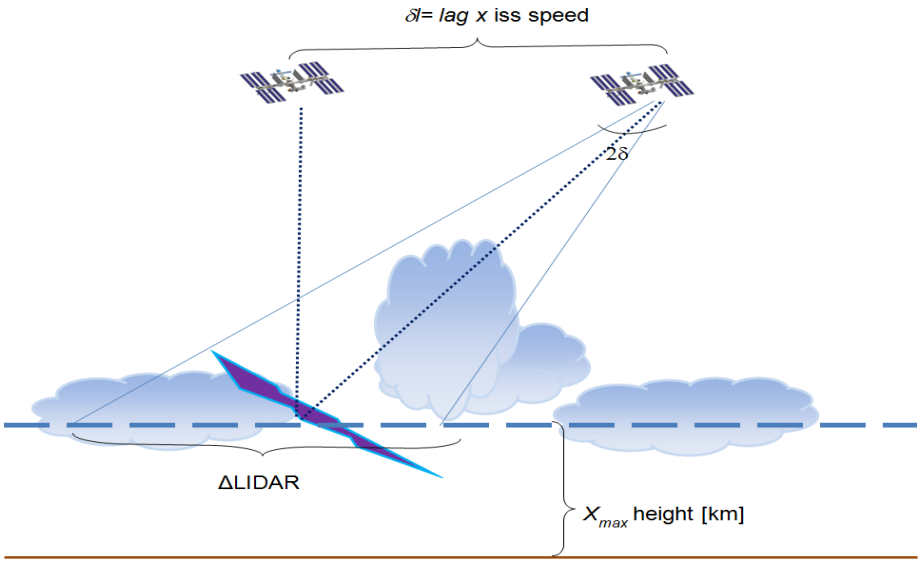

Figure 5.1: Depiction of the false positive false negative tests.

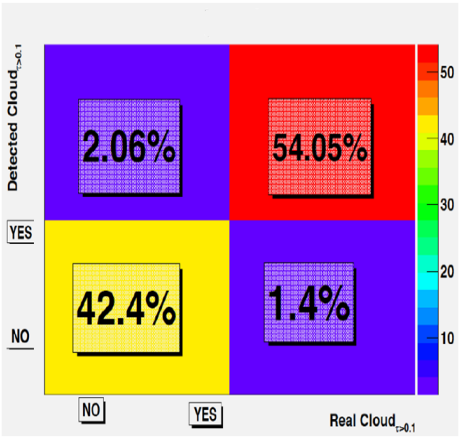

(a) $2\delta = 1°$

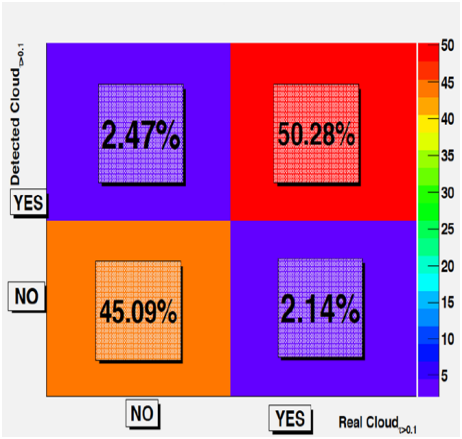

(b) $2\delta = 2°$

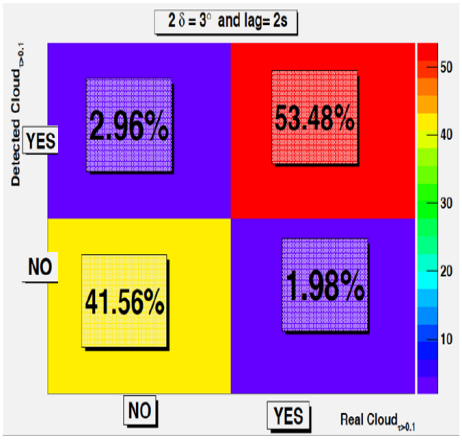

(c) $2\delta = 3°$, lag 3s

Figure 5.2: False positive false negative studies for different uncertainties (see text).

5.2 Cloud attenuation of the EAS.

One of the most important aims of the present work is to address the issue regarding the modifications of the interpreted EAS fluorescent signal of a detector flying on a low earth orbit.
Great effort was put into developing the necessary algorithms and programming code to promptly address the issue. Not only did we took special care in using the ISS latitude distribution but there was also a careful follow-up of the different lines of sight along any given simulated EAS.

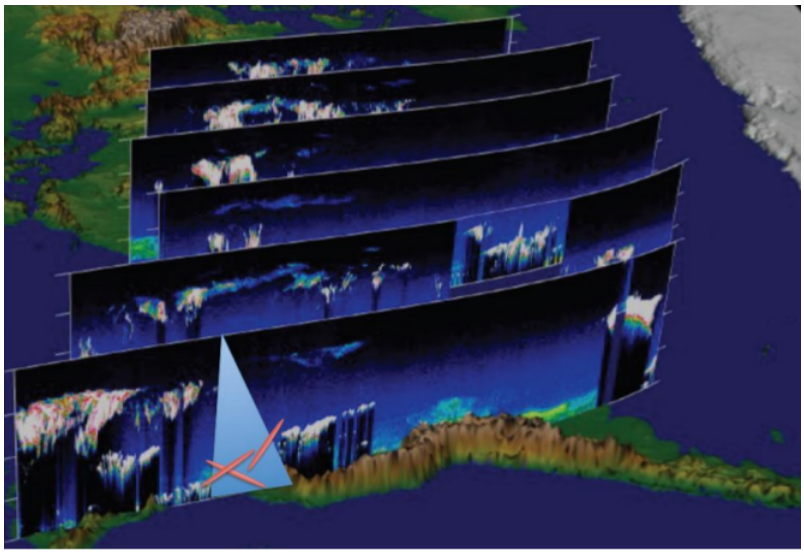

Figure 5.3: Depiction of our insertion of different showers inside CALIPSO's *curtain files.*

In order to explain the results we shall recall the way in which we proceeded to calculate the amount of photons that arrived at the detector's pupil.

1. We situated the detector on top of a ground spot that followed the ISS latitude distribution.

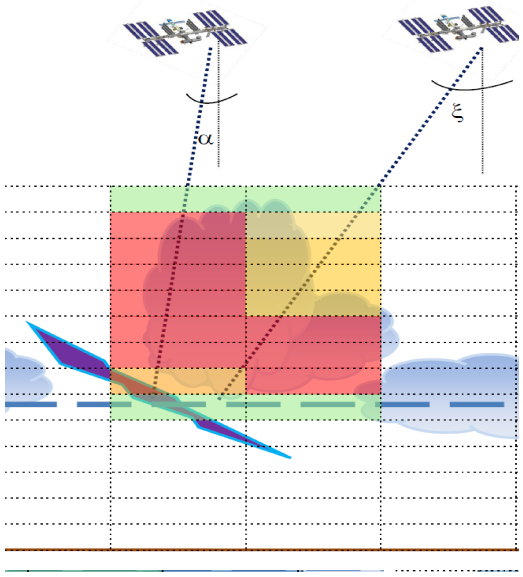

Figure 5.4: Depiction of τ calculation for different lines of sight. The cell color ilustrates the expected value of $\alpha(\vec{x})$. Purple trace represents the EAS.

2. We then inserted simulated showers inside a 60° FoV.(see figures 5.2 and 5.4).

3. We calculate the photon yield at each point of each inserted shower using the temperature T, and pressure P profiles (see figure 3) as input for [Nagano 2008]:

$$\epsilon = \frac{\left(\frac{\mathrm{d}E}{\mathrm{d}X}\right)_E}{\left(\frac{\mathrm{d}E}{\mathrm{d}X}\right)_{0.85MeV}} \frac{A\rho}{1+\rho B\sqrt{T}}$$

In this last expression ϵ is the photon yield $\frac{\mathrm{d}E}{\mathrm{d}X}$ is the energy deposition and A and B are experimentally assigned constants.

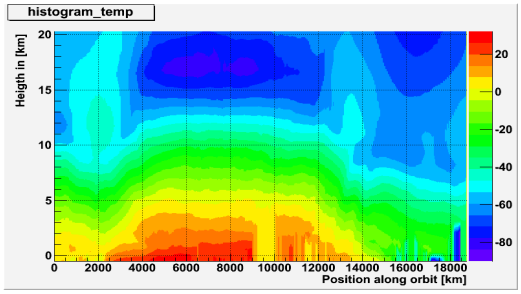

(a) Temperature profile for a CALIPSO sample orbit.

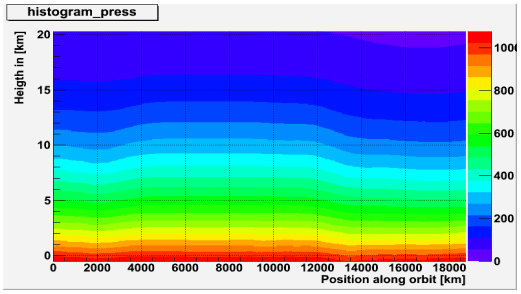

(b) Pressure profile same sample.

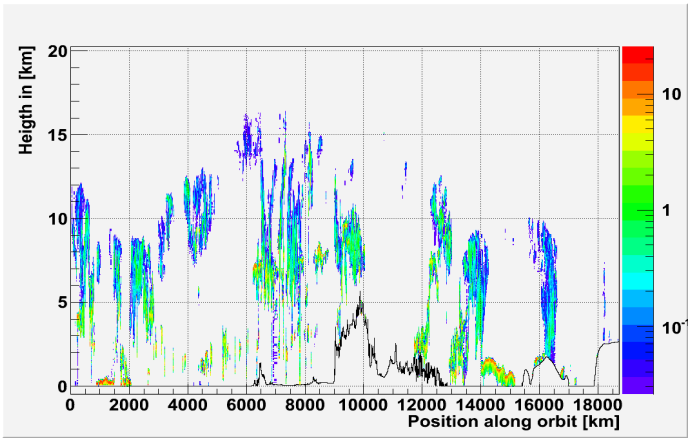

(c) Extinction coefficient for the same sample. Black line represents surface elevation.

4. We then propagate the produced fluorescent light up to the detector (following a simple ballisitic approach). Each point of the shower defines its specific line of sight, and we use the values of the extinction coefficient along this line of sight (see figure 5.4) .

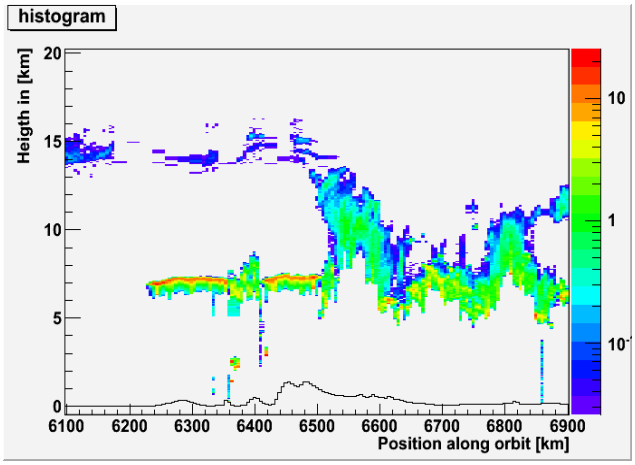

Figure 5.5: A "zoom out" of the example called the cloudy region(This "zoom out" can accommodate 2 FoV)

Examples of this procedure for different zenith angle in a "cloudy" region are shown in 5.6. All the showers in that figure correspond to an energy of 10^{20}eV.

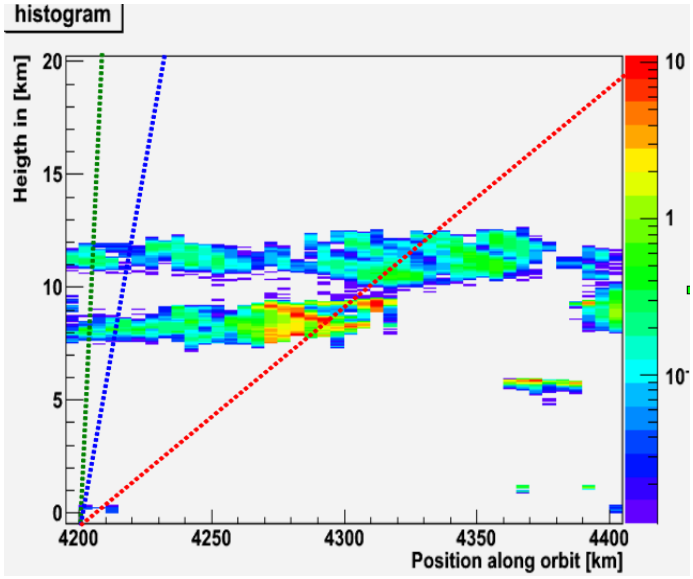

(a) *Cloudy* region, shower trajectories are shown as dashed lines.

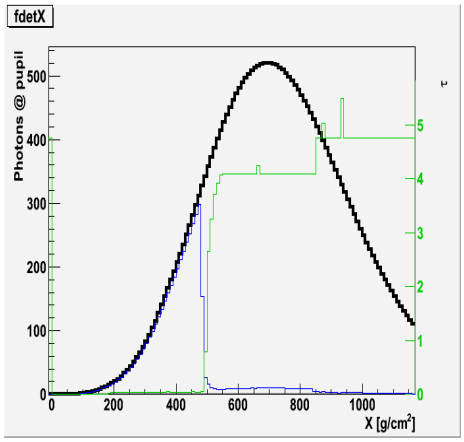

(b) $\theta = 30°$

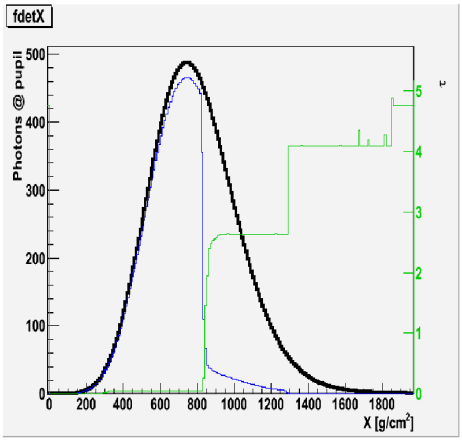

(c) $\theta = 60°$

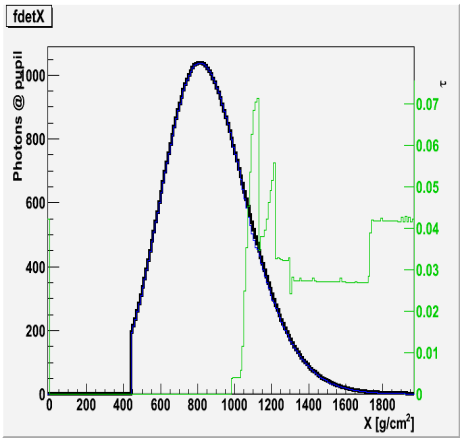

(d) $\theta = 85°$

Figure 5.6: Example "cloudy" region and its effects in shower reconstrucion. Black lines represent the expected unattenuated signal. Blue lines represent the actual detected signal, and green lines represent the value of τ integrated along the line of sight.

5.3 Thin Clouds & and altitudes uncertainties of τ determination.

With the whole scheme developed for following any specific line of sight for any given shower we then turned to a problem which is very specific to a lidar atmospheric probing: thin clouds and uncertainties in the extinction coefficient spatial determination.
It is almost certain that a infrared monitoring camera would be able to detect a great deal of the clouds present in the cloudy examples of the last section (although the correct determination of the optical thickness along the lines of sight is still a complicated task for such a camera).

Regarding the uncertainties in the extinction coefficient spatial determination we simulated this effect by randomly shifting the value of each column of the *curtai* above sea level. This concept is shown in figure 5.7 5.6

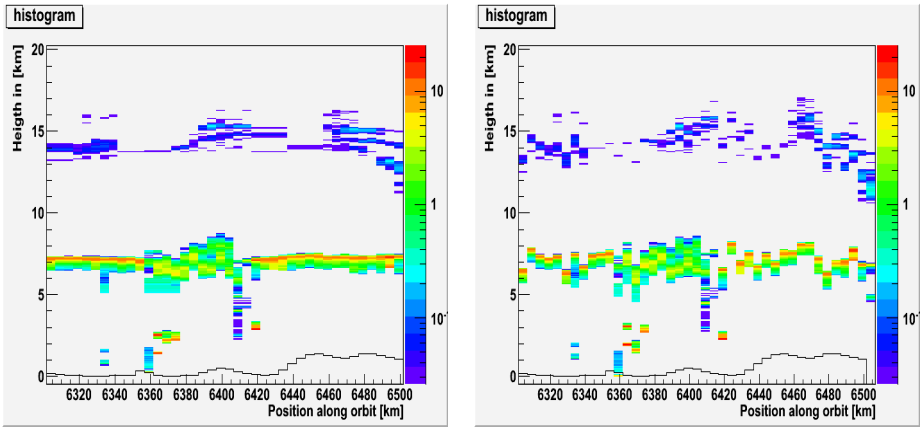

(a) Normal (b) Shifted

Figure 5.7: Uncertainty in the spatial determination of the extinction coefficent for a sample region.

To be able to study to some extent the effects of thin clouds, we defined the "thin cloud regions". This were regions that extended horizontally for one FoV and fulfilled that at least 50% of the vertical values of tau for the region were between 0.1 and 1. A example of such a region is shown in figure 5.3

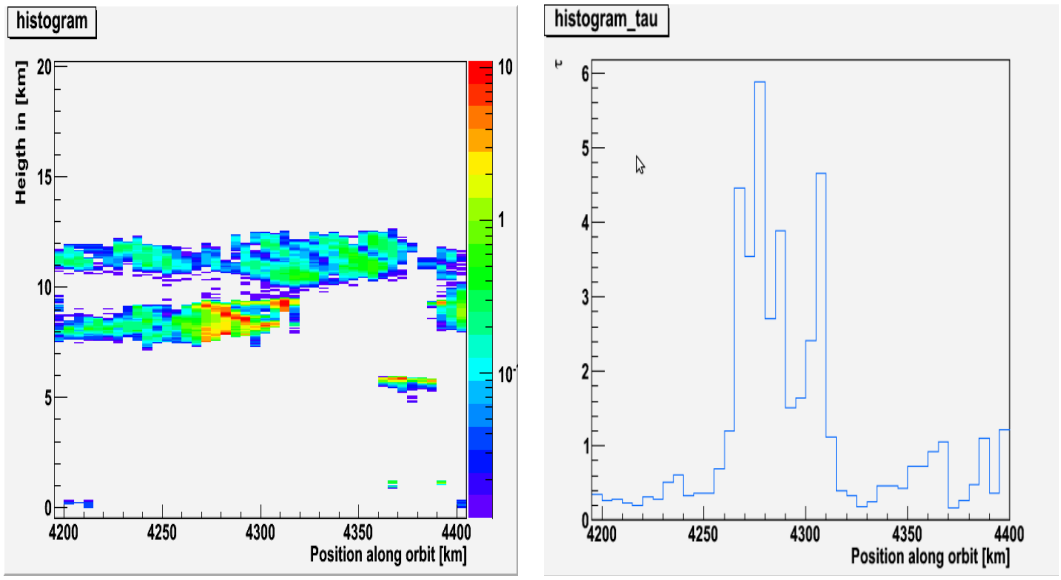

(a) Extinction coefficient α (b) Vertical optical thicknessτ

Figure 5.8: Example region fulfilling our *thin cloud region* criteria .

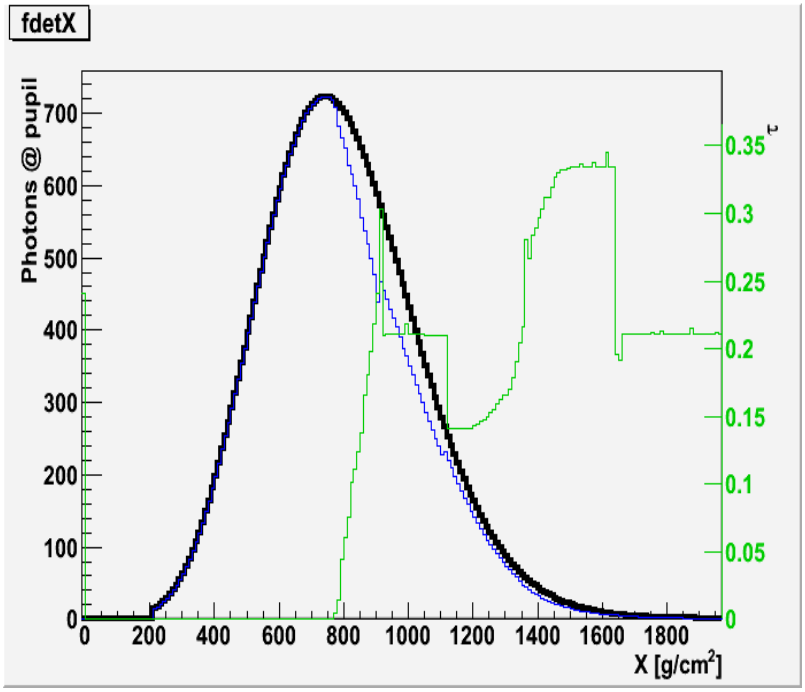

(a)

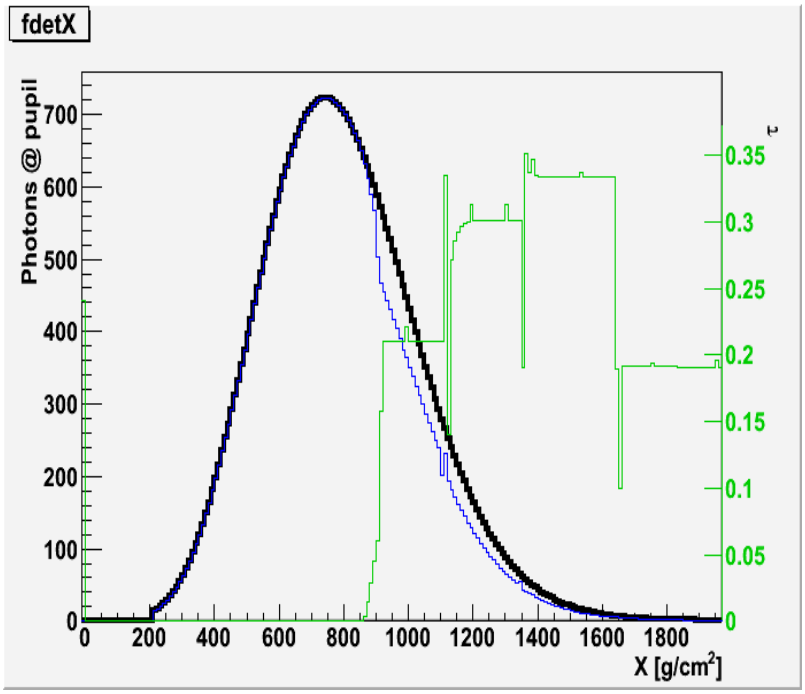

(b)

Figure 5.9: Example of the effect of shifting the values of $\alpha(\vec{x})$ in the number of photons arriving at JEM-EUSO's pupil, for a shower with $\theta = 75°$ and log(E/eV)=20, in a *thin cloud* region.

We conclude this study showing the statistic studies carried for this special thin cloud regions. There seems to be a manifest correlation in the magnitude of the induced errors, and the EAS's zenth angle.

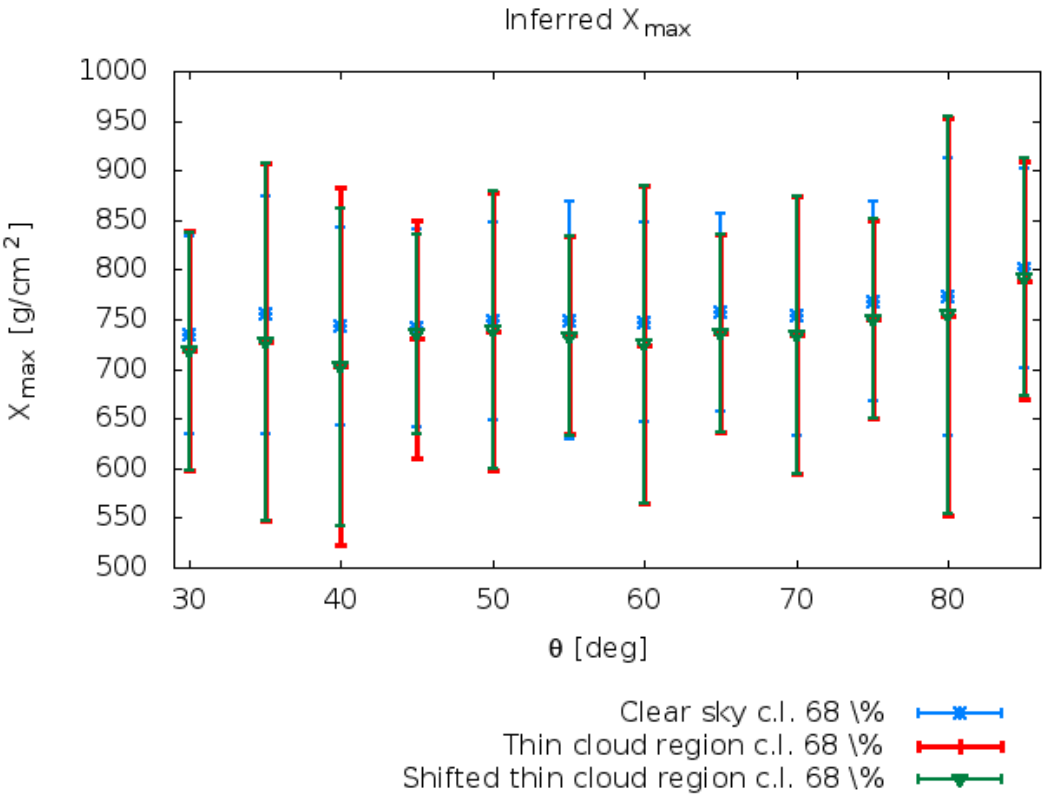

Figure 5.10: Reconstructed values of X_{max} for different cloud conditions(see text)

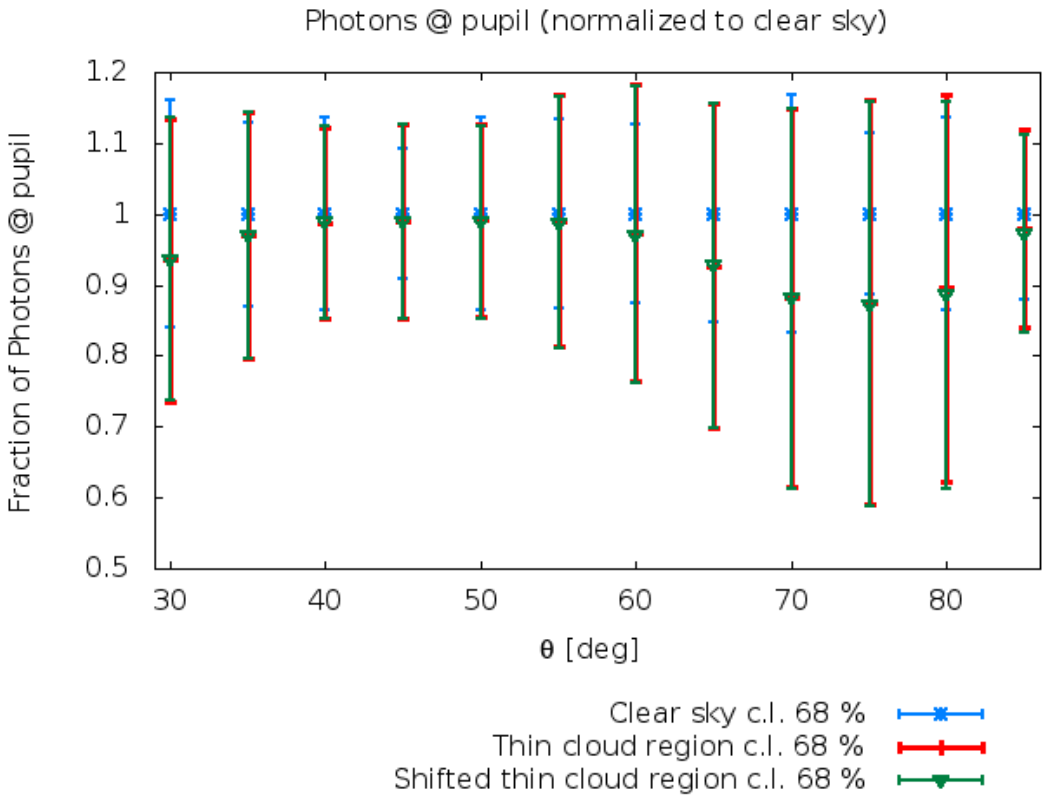

Figure 5.11: Amount of photons arriving at the detector's pupil (normalized to clear-sky condition) for different cloud conditions(see text)

Chapter 6

Contributions to the JEM-EUSO mission

6.1 CALIPSO data analysis and mission requirements constrains

Autocorrelation length

In order to asses which of the different approaches to JEM-EUSO's lidar should be taken, we studied the correlation lengths of the cloud's optical depth ($\tau = \int \alpha(x)dx$) for different heights. This study showed that cloud's optical properties decorrelate in length's in the order of a few km, whereas the FoV expands to hundreds of km. One of the proposed operational modes of the lidar subsystem is the so called *fixed scan mode*. In this mode the lidar subsystem would be set to point to fixed positions inside the FoV, in hopes that it could still retrieve significant information of the atmospheric conditions surrounding an EAS event occurring in another region of JEM-EUSO's Fov. This last study disfavored this operational mode, by quantitatively assessing the loss of optical information in short lengths (the order of a few kilometers). At the time this study was presented, there was the ideas that mostly only the optically thick clouds, and hence visible with the IR camera, would present this kind of correlations lengths. This made the fixed scan mode a sufficiently good approach; with its practical advantages over other modes (no movable parts, easier to calibrate, etc.).

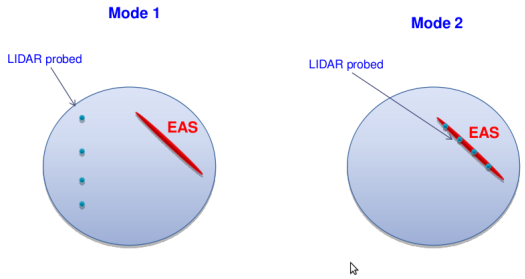

Figure 6.1: Illustration of the 2 different modes for operating the lidar. In mode 1 the lidar probing points are kept the same inside the FoV regardless of the EAS.

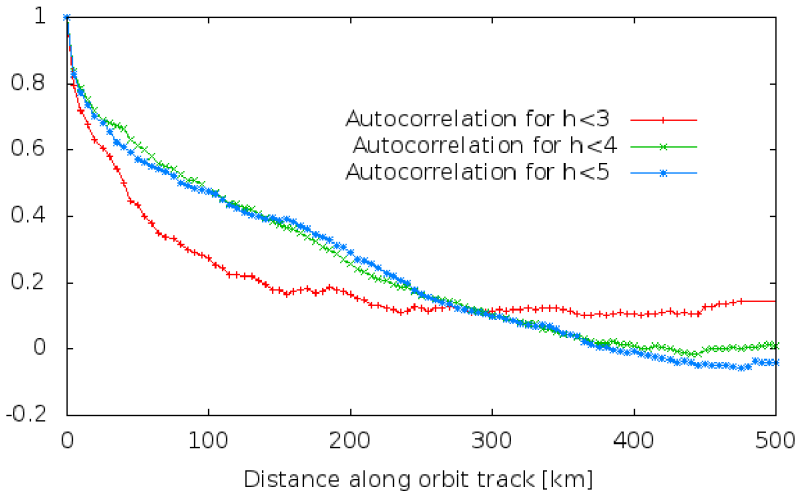

Figure 6.2: Autocorrelation of cloud's optical thickness as a function of distance, calculated upwardly from the ground upto different altitudes.

Attitude uncertainties and their implication in cloud structure assesment.

It was brought to our attention that, due to normal vibration modes in the ISS, there is an intrinsinc uncertainty in the actual portion of the atmosphere our lidar will be scoping(attitude verification). We carried out studies in which we simulated the unavoidable uncertainty due to this effect in the line of sight of JEM-EUSO's lidar (see Fig 6.3). This translates in an error affecting the measurement of τ for any candidate of event in the FoV. Different fluctuations in the line of sight are bound to produce false-positive and false-negative effect in our measurement(i.e. there will be times when we detect thin clouds($0.1 < \tau < 1$) although there were none present

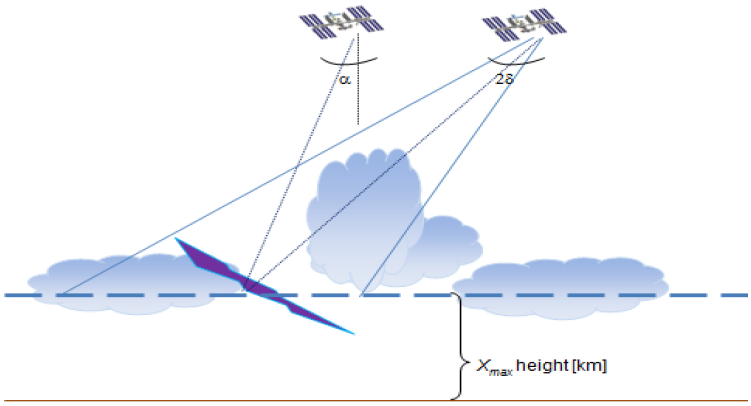

Figure 6.3: Depiction of the attitude uncertainty problem. The precision of actual line of sight of the lidar measurement is expected to have an error of $\pm 1.5°$.

and viceversa).

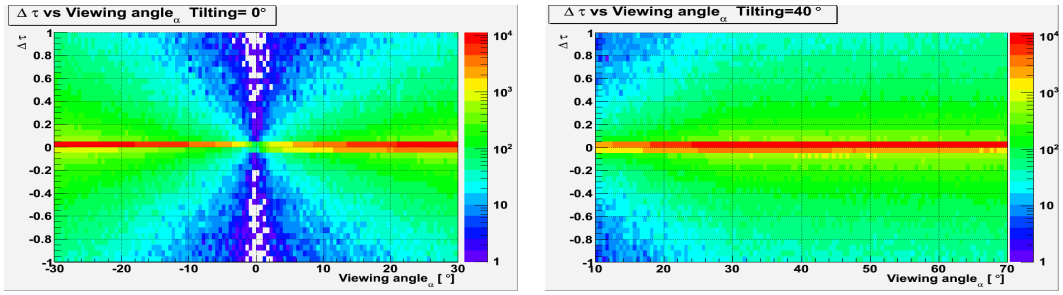

(a) (b)

Figure 6.4: Scattered plot of $\Delta\tau$ vs the actual viewing angle, for no tilting and tilting angle of 40°.

For any EAS candidate event in JEM-EUSO's FoV, there will be a lag (expected to be of ~ 1 second) between the detection and the lidar proving of the atmosphere surrounding the EAS. We carried a study in which we defined a line of sight from a previously selected point (at the typical height for X_{max} of a 60° shower) in an EAS upto the detector. This was taken as the *"real"* line of sight. We then defined another line of sight going from the same point in the EAS but to the ISS relative position after the assumed lag in time had passed. This new line of sight (namely the *"detected"* line of sight) was then perturbed as to simulate the fluctuations in

the attitude of the telescope. We calculated the value of the optical thickness for both lines of sight and compared. We did this for roughly 350 CALIPSO orbits. We concluded that $\sim 5\%$ of the events will be contaminated with a false-positive/false-negative scenario (same scheme as the one already discussed in chapter 5). We followed the ISS trajectory and inserted showers as depicted in figure 5.2, only this time the viewing angle could exceed the 30° as a consequence of operating in tilted mode.

This different lines of sight imply different values of τ which in turn translate to an uncertainty in the lidar's measurement of tau. This practically unavoidable error $\Delta\tau = \tau_{real} - \tau_{detected}$ increases in JEM-EUSO's "tilted" mode and has a standard deviation well over 0.15 (Fig 6.6). One of the former requirements imposed to JEM-EUSO's lidar was to measure τ with an SD$<$ 0.15, this analysis shows this requirement should be revisited.

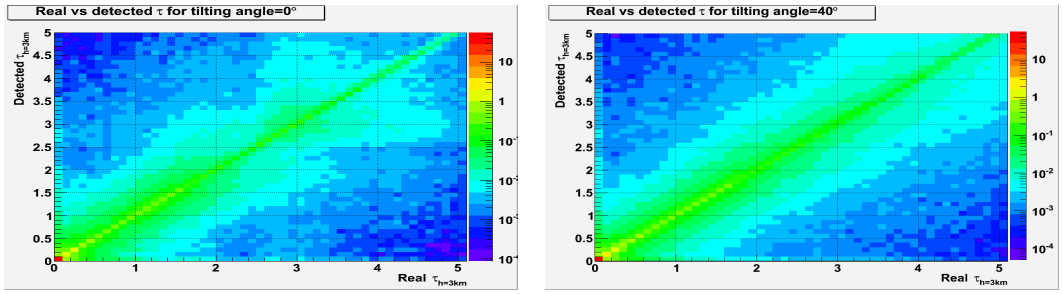

(a) (b)

Figure 6.5: Scattered plot of $\tau_{detected}$ vs τ_{real}, for no tilting and tilting angle of 40°. As it can be seen the tilted phase of the JEM-EUSO mission will increase the false positive scenario (see chapter 5).

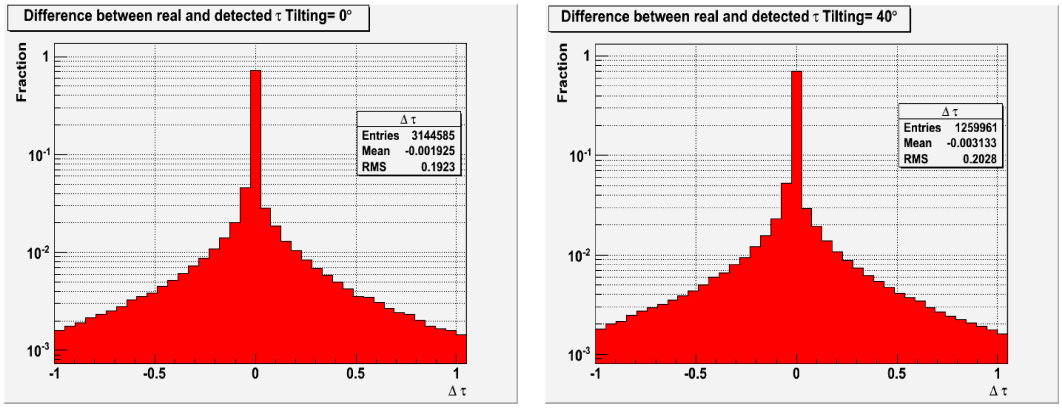

(a) (b)

Figure 6.6: Distribution of $\Delta\tau$ in (logarithmic scale) for no tilting and tilting angle of 40°.

Chapter 7

Outlook and Conclusions

7.1 Cloud effects in novel space born experiments

As discussed in chapters 1&2 the influence of clouds in space borne experiments has not been completely taken into account for studies of feasibility and performance of such detectors. As it has been discussed in the present work global cloud coverage will be responsible for a 30% loss of otherwise(cloud free) detectable showers.

The vertical structure of clouds may sometimes result deceitful in the estimation of the primaries' energy in perhaps 16% of the detected events (the thin clouds regions). This figure could be reduced in case the atmospheric sounding of the specific detector is capable of correctly reconstructing the atmospheric conditions that surrounded the aforesaid events.

The specifics of each mission's atmospheric probing will prove crucial for a correct interpretation of the scientific data. As discussed in chapter 5 the geometry of each event affects the uncertainties in a very specific way. Hence the necessity for angular precision is not only a requirement imposed by the need for reconstructing the incoming particle's trajectory, but to properly asses all of the relevant scientific features (primary's energy standing out the most).

As a continuation of the studies regarding vertical structure of clouds one could look at the effects of having showers developing above or through optically thin clouds. Then, it could be desirable to add a distinctive Cerenkov peak at certain lower altitude, i.e. showers that "impact" into an optically thick cloud. Doing this in such fashion, that the whole shower trajectory is reconstructible and a Cerenkov-marked impact point is detectable due to the cloud's presence. This could then be carried on

7.2 Main results in the JEM-EUSO mission's framework

One of the aims of the present thesis is to be able to contribute to the development of the on going effort from the JEM-EUSO mission. Though there are still many issues to address, the techniques developed in the present work may be used for further studies using satellite data. Currently there is a comprehensive amount of data and resources in the JEM-EUSO's wiki, available to the mission's collaborators. This resources have been developed while the research carried out for this present work, and can serve as starting point for people working in this kind of studies.

Finally we wish to highlight this work's main contributions to the development of the JEM-EUSO mission (at least from the author's point of view):

- Regarding the duty cycle, we have concluded that the currently accepted duty cycle of 20%, will be reduced by the presence of optically thick clouds ($\tau > 1$) by a factor of 0.7 .
- Regarding the LIDAR's operational mode, we conclude that the *fixed scan mode* won't be favored by the presence of clouds.
- Regarding the attitude's uncertainty. We conclude that under present conditions, there are mainly two viable options:
  - Either enabling the star tracking system to *feed* real time data to the lidar's pointing system in order to diminish the in the optical thickness' uncertainty by improving the accuracy of line of sight.
  - or enabling a faster lidar pointing sytem that could prove faster the area around the EAS. One possibility is the use of MEMS, but this kind of technology has not been used in space, and there is no concluding data about their life-time expectancy under the strain imposed by the powerful UV laser shots.

All in all, this has been one of the first efforts using lidar satellite data to study the cloud structure in JEM-EUSO's work frame. This is just one of many studies necessary for the JEM-EUSO mission. There is still plenty to do and to research in order to achieve an optimal design and performance of the AM system.

Appendix A

CALIPSO's Lidar Cloud Profile Record

Parameter	Data Type	Units	Nominal Range	Elem/ Rec	Bytes
Latitude	Float_32	deg	-90.0…90.0	3	12
Longitude	Float_32	deg	-180.0…180.0	3	12
Profile_Time[C]	Float_64	sec	4.204E8…7.389E8	3	24
Profile_UTC	Float_64	NoUnits	60,426.0…160,601.0	3	24
Day_Night_Flag	Int_8	NoUnits	0…1	1	1
Column_Optical_Depth_Cloud_532	Float_32	NoUnits	0.0…5.0[M]	1	4
Column_Optical_Depth_Cloud_Uncertainty_532	Float_32	NoUnits	0.0…99.99	1	4
Column_Optical_Depth_Aerosols_532	Float_32	NoUnits	0.0…3.0[M]	1	4
Column_Optical_Depth_Aerosols_Uncertainty_532	Float_32	NoUnits	0.0…99.99	1	4
Column_Optical_Depth_Stratospheric_532	Float_32	NoUnits	0.0…3.0[M]	1	4
Column_Optical_Depth_Stratospheric_Uncertainty_532	Float_32	NoUnits	0.0…99.99	1	4
Column_Optical_Depth_Aerosols_1064	Float_32	NoUnits	0.0…3.0[M]	1	4
Column_Optical_Depth_Aerosols_Uncertainty_1064	Float_32	NoUnits	0.0…99.99	1	4
Column_Optical_Depth_Stratospheric_1064	Float_32	NoUnits	0.0…3.0[M]	1	4
Column_Optical_Depth_Stratospheric_Uncertainty_1064	Float_32	NoUnits	0.0…99.99	1	4
Column_Feature_Fraction	Float_32	NoUnits	0.0…1.0	1	4
Column_Integrated_Attenuated_Backscatter_532	Float_32	sr^{-1}	0.0…2.0	1	4
Column_IAB_Cumulative_Probability	Float_32	NoUnits	0.0…1.0	1	4
Tropopause_Height	Float_32	km	4.0…22.0	1	4
Tropopause_Temperature	Float_32	°C	-100.0…-20.0	1	4
Temperature	Float_32	°C	-120.0…60.0	345	1,380
Pressure	Float_32	hPa	1.0…1086.0	345	1,380
Molecular_Number_Density	Float_32	m^{-3}	$8x10^{22}$…$5x10^{25}$	345	1,380
Relative_Humidity	Float_32	%	0.0…150.0	345	1,380
Surface_Elevation_Statistics	Float_32	km	-1.0…9.0	4	16
Surface_Winds	Float_32	ms^{-1}	-80.0…80.0	2	8
Samples_Averaged	Int_16	NoUnits	0…480	345	690
Aerosol_Layer_Fraction	UInt_8	NoUnits	0…30	345	345
Cloud_Layer_Fraction	UInt_8	NoUnits	0…30	345	345
Atmospheric_Volume_Description	UInt_16	NoUnits	1…49,146	345x2	1,380
Extinction_QC_Flag_532	UInt_16	NoUnits	0…32,768	345x2	1,380
CAD_Score	Int_8	NoUnits	-101…105	345x2	690
Total_Backscatter_Coefficient_532	Float_32	sr^{-1} km^{-1}	0.0…1.5	345	1,380
Total_Backscatter_Coefficient_Uncertainty_532	Float_32	sr^{-1} km^{-1}	0.0…99.99	345	1,380
Perpendicular_Backscatter_Coefficient_532	Float_32	sr^{-1} km^{-1}	0.0…0.35	345	1,380
Perpendicular_Backscatter_Coefficient_Uncertainty_532	Float_32	sr^{-1} km^{-1}	0.0…99.99	345	1,380
Particulate_Depolarization_Ratio_Profile_532	Float_32	NoUnits	0.0…1.0	345	1,380
Particulate_Depolarization_Ratio_Uncertainty_532	Float_32	NoUnits	0.0…99.99	345	1,380
Extinction_Coefficient_532	Float_32	km^{-1}	0.0…12.0	345	1,380
Extinction_Coefficient_Uncertainty_532	Float_32	km^{-1}	0.0…99.99	345	1,380
Cloud_Multiple_Scattering_Profile_532	Float_32	NoUnits	0.5…1.0	345	1,380
Ice_Water_Content_Profile	Float_32	$g\ m^{-3}$	0.0…0.54	345	1,380
Ice_Water_Content_Profile_Uncertainty	Float_32	$g\ m^{-3}$	0.0…99.99	345	1,380

Appendix B

HDF and CALIPSO data

All of the CALIPSO data comes in HDF format. There are various ways of accessing this kind of data.Currently the most common one is using hdfview and hdp. Although data is free to download, registration is needed in order to gain access to the data. There is also some other data ordering tools for the data, nevertheless most of this ordering tools are too much weather-research oriented for our purposes. For each hdf file $\sim$ 4200 profiles are reported, (the horizontal resolution is 5km); nevertheless, it must be kept in mind that this number changes for each file. For the present work a specific function that writes any scientific dataset (SDS) available in a HDF file to a simple ASCII file. In order to work with the HDF format in a systematical way, this function was used to create temporary files from which one could read the relevant information.

```
#ifndef hdf_root_h
#define hdf_root_h

#include <cmath>
#include <cstdlib>
#include "TROOT.h"
using namespace std;

void hdp_to_file( const string & sds, const string & outfilename,const  string & infilename){
      char  instruction[145];
      string line; //this is a dummy string  in which to appende the next filename to process
      line=".! hdp dumpsds  -n  ";
      line.append(sds);
      string str;
      str = "  -d -o  ";
      str.append(outfilename);
      line.append(str);
      line.append(" ");
      line.append(infilename);
      sprintf(instruction,"%s",line.c_str());
      cout<< instruction << endl; //Instruction an the array of character
      gROOT->ProcessLine(instruction);
}


#endif
```

Appendix C

Header Files in C++

C.1 Line of sight determination

The following function fills in the values for the *optical-depth-vector* along any given line of sight, for a 2D matrix containing the value of the extinction coeffciente in each cell:

```
#ifndef tau_line_of_sight_h
#define tau_line_of_sight_h

#include <cmath>
#include <cstdlib>
#include <iostream>
#include <fstream>
#include <string>
#include <iomanip>
#include <sstream>
#include <vector>
//ROOT header files
#include "TH2D.h"
#include "TStyle.h"
#include "TCanvas.h"
#include "TFile.h"
using namespace std;



//   All  the  distances are  taken in km!!
//angles in radians

void   tau_line_of_sight_pos( TH2D* matrix,const double beta,const double hor_cero,const double  ver_cero,vector<double>& alt_v

int dumi=0;
double dumd=0;
const double pi=4.*atan(1.0);
double tau=0,D=0,sumhor=0,sumver=0,sumD=0;
const double cosB=cos(beta), sinB=abs(sin(beta)),tanB=tan(beta);
const double cotanB=1./tanB;
double Dmax=(20.2-ver_cero)/sinB;
```

```
double hor=0.,ver=0.;
double xi=atan(.06/5.);
double sign=cosB/abs(cosB);
  sumhor=hor_cero;
sumver=ver_cero;
dumi=matrix->FindBin(hor_cero,ver_cero);
double alpha=matrix->GetBinContent(dumi);
dumi=0;
///  first cell!
if(beta<=xi || beta>pi-xi){
  alt_vec.push_back(sumver);
  D=5./abs(cosB);
  sumhor+=5.*sign;
  sumver+=D*sinB;
  sumD+=D;
  dumi=matrix->FindBin(sumhor,sumver);
  alpha=matrix->GetBinContent(dumi);
  tau+= D*alpha;
  tau_vec.push_back(D*alpha);

  ver=D*sinB;
  hor=0.;


}
else{
  alt_vec.push_back(sumver);
  D=0.06/sinB;
  sumhor+=D*cosB;
  sumver+=0.06;
  sumD+=D;
  dumi=matrix->FindBin(sumhor,sumver);
  alpha=matrix->GetBinContent(dumi);
  tau+= D*alpha;
  tau_vec.push_back(D*alpha);

  ver=0.;
  hor=D*abs(cosB);
}


  while(sumver<20.14){
//  from below
  if( ver==0. ){
    if( (5.-hor)*abs(tanB)<0.06 ){ //case1
      alt_vec.push_back(sumver);
      D=(5.-hor)/abs(cosB);

      sumhor+=D*cosB;
      sumver+=D*sinB;
      sumD+=D;
      dumi=matrix->FindBin(sumhor,sumver);
      alpha=matrix->GetBinContent(dumi);
      tau+= D*alpha;
      tau_vec.push_back(D*alpha);
```

```
      hor=0. ;
      ver=D*sinB;

    }
    else{ //case 2
      alt_vec.push_back(sumver);
      D=0.06/sinB;
            sumhor+=D*cosB;
      sumver+=0.06;
      sumD+=D;
      dumi=matrix->FindBin(sumhor,sumver);
      alpha=matrix->GetBinContent(dumi);
      tau+= D*alpha;
      tau_vec.push_back(D*alpha);

      hor=hor+D*abs(cosB);
      ver= 0.;
    }
  }


//      from the side
else{
    if((.06-ver)*abs(cotanB) > 5. ){ //3 case
      alt_vec.push_back(sumver);
      D=5./abs(cosB);
      sumhor+=5.*sign;
      sumver+=D*sinB;
      sumD+=D;
      dumi=matrix->FindBin(sumhor,sumver);
      alpha=matrix->GetBinContent(dumi);
      tau+= D*alpha;
      tau_vec.push_back(D*alpha);
      hor=0.;
      ver=ver+D*sinB;


    }
    else{
      alt_vec.push_back(sumver);
      D=(0.06-ver)/sinB;
      sumhor+=D*cosB;
      sumver+=D*sinB;
      sumD+=D;
      dumi=matrix->FindBin(sumhor,sumver);
      alpha=matrix->GetBinContent(dumi);
      tau+= D*alpha;
      tau_vec.push_back(D*alpha);
      hor=D*abs(cosB);
      ver=0.;
    }

  }
}
```

```
}


#endif
```

C.2 Tau calculations

The following functions were written to obtain relevant information about the optical-depth-vector calculated in the previous section.

```
#ifndef calipso_tau_utils_h
#define calipso_tau_utils_h
#include <cmath>
#include <cstdlib>
#include <iostream>
#include <fstream>
#include <string>
#include <iomanip>
#include <sstream>
#include <vector>

using namespace std;


double height_downto_tau(vector<double>& tau_vec,vector<double>& alt_vec,double tau_cut) {

  int prueb=0;
  double dumd=0.;
  int dumi=0;
  for(int k=tau_vec.size()-1; k> -1;k--){
    dumd+=tau_vec[k];
    if(dumd>tau_cut && prueb != 1){
      dumi=k;
      prueb=1;
    }
  }
  if(prueb==0){return 0.;}
  else{return alt_vec[dumi];}

}

double  tau_between_heights(vector<double>& tau_vec,vector<double>& alt_vec,double h_low, double h_high) {
 int prueb=0;
 double dumd=0.;
 int dumi_low=0;
 int dumi_high=alt_vec.size()-1;
 for(int k=0;k<alt_vec.size() ;k++){
    if(alt_vec[k]>h_low && prueb != 1){
    dumi_low=k;
    prueb=1;
    }
 }
 prueb=0;
```

```
 for(int k=alt_vec.size()-1;k>-1 ;k--){
    if(alt_vec[k]<h_high && prueb != 1){
    dumi_high=k;
    prueb=1;
    }
 }

  for(int k=dumi_low;k<dumi_high+1;k++){dumd+=tau_vec[k];}
  return dumd;
}



double height_upto_tau(vector<double>& tau_vec,vector<double>& alt_vec,double h_low,double tau_cut) {
  int prueb=0;
 double dumd=0.;
 int dumi_low=0;
 int dumi;
 for(int k=0;k<alt_vec.size() ;k++){
    if(alt_vec[k]>h_low && prueb != 1){
    dumi_low=k;
    prueb=1;
    }
 }
 prueb=0;
 for(int k=dumi_low;k<tau_vec.size() ;k++){
   dumd+=tau_vec[k];
   if(dumd>tau_cut && prueb != 1){
     dumi=k-1;
     prueb=1;
   }
 }
  if(prueb==0){return 0.;}
  else{return alt_vec[dumi];}
}
#endif
```

Bibliography

[Abbasi,Abu-Zayyad,Amann 2004] Abbasi, R.U.; Abu-Zayyad, T.; Amann, J.F.; et al., *Study of Small-Scale Anisotropy of Ultra-High-Energy Cosmic Rays Observed in Stereo By the High Resolution Fly's Eye Detector* 2004, Astroparticle Physics, 610:L73-L76 August 1

[Abbasi,Abu-Zayyad 2004 (2)] Abassi, R.U.; Abu-Zayyad, T.; et al., *Search for Point Sources of Ultra-High Energy Cosmic Rays Above* $4.0 \times 10^{19} eV$ *Using a Maximum Likelihood Ratio Test* Astroparticle Physics, 23 Dec. 2004

[Abbasi et al. 2004] Abassi, R.U.; Abu-Zayyad, T.; et al. *A Search for Arrival Direction Clustering in the HiRes-I Monocular Data Above 1019.5 eV*, Astroparticle Physics, 27 May 2004

[Ahrens 2000] C.Donald Ahrens, *Essentials of Meteorology: An Invitation to the Atmosphere*, Brooks Cole, USA (2000).

[Auger 1939] Pierre Auger, P. Ehrenfest, R. Maze, J. Daudin, and Robley A. Fréon. *Extensive Cosmic-Ray Showers*Rev. Mod. Phys. 11, pp 288–291 (1939).

[Auger Collaboration] Pierre Auger Observatory *Pierre Auger Observatory Design Report*, `http://www.auger.org/index.html`.

[Berezinsky et al. 1990] V. Berezinsky , S. Bulanov, V. Dogiel, V. Ginzburg and V. Ptuskin, *Astrophysics of Cosmic Rays*, North-Holland Publishing Company(1990):

[Bergmann 2007] Bergmann, T. and others,*One-dimensional hybrid approach to extensive air shower simulation* Astropart. Phys. Vol. 26, pp 420-432, astro-ph/0606564, 2007.

[Biermann & Sigl 2001] Peter L. Biermann, Günter Sigl, *Introduction to Cosmic Rays*:Physics and Astrophysics of Ultra High Energy Cosmic Rays. M. Lemoine/ G. Sigl(ed.) (2001).

[Bird et al. 1995] D.J. Bird , et al. : Astrophys. J. **441**, 144 (1995)

[Bird et al. 1998] Bird et. al. *Study of Broad Scale Anisotropy of Cosmic Ray Arrival Directions from* $2 \times 10^{17} eV$ *to* $10^{20} eV$ *from Fly's Eye Data* arXiv:astro-ph/9806096v1

[Bossard et al. 2001] G. Bossard, H. J. Drescher, N. N. Kalmykov, S. Ostapchenko, A. I. Pavlov, T. Pierog, E. A. Vishnevskaya, and K. Werner, Phys. Rev. D63, 054030 (2001).

[Bunner 1967] A.N. Bunner,*Cosmic Ray Detection by Atmospheric Fluorescence* PhD Tesis, Cornell University, Ithaca,NY, USA, (1967).

[CALIPSO ATBD] David M. Winker, Chris A. Hostetler, Mark A. Vaughan, Ali H. Omar, *CALIOP Algorithm Theoretical Basis Document* PC-SCI-202 Part 1,2006.

[CALIPSO *web page*] `http://www.nasa.gov/mission\_pages/calipso/main/`

[Fermi 1949] E. Fermi, *On the Origin of the Cosmic Radiation*, Physical Review 75, pp. 1169-1174, 1949

[Gaisser 1990] T. K. Gaisser, *Cosmic rays and particle physics*, Cambridge Univ. Press, Cambridge, 1990.

[Gaisser 2002] J. Alvarez-Muniz, R. Engel, T. K. Gaisser, J. A. Ortiz, and T. Stanev,*One-dimensional Hybrid Approach to Extensive Air Shower Simulation* Phys. Rev. D66, 033011 (2002)

[Garino et al. 2011] F. Garino, A. Guzman, M. Bertaina, C. Cassardo, R. Cremonini, C. De Donato, G. MedinaTanco, K. Shinozaki *Cloud Coverage and its Implications for Cosmic Ray Observation from Space*,32nd's proceedings ICRC Beijing (2011).

[Garipov 2005] G.K. Garipov, B.A. Khrenov, M.I. Panasyuk, V.I. Tulupov, A.V. Shirokov, I.V. Yashin, H. Salazar, *UV radiation from the atmosphere: Results of the MSU TATIANA satellite measurments* Astroparticle Physics 24 (2005) pp 400 408.

[Greisen 1966] K.Greisen *End to the Cosmic-Ray Spectrum?*, Physical Review Letters 16 (17): 748–750, (1966).

[Hess 1912] V. F. Hess: Phys. Z. **13**, 1084 (1912).

[Hillas 1984] A. M. Hillas, Ann. Rev. Astron. Astrophys. 22, 425 (1984).

[HiRes 2004] Abbasi, R.U.; Abu-Zayyad, T.; et al., *Observation of the Ankle and Evidence for a High-Energy Break in the Cosmic Ray Spectrum* Astroparticle Physics, 17 Jan. 2004

[Homola 2009] Piotr Homola for the Pierre Auger Collaboration, *Ultra-high energy photon studies with the Pierre Auger Observatory*,31^{st} International Cosmic Ray Conference, Łódź 2009

[Hongbin et al. 2010] Hongbin et al. 2010 J.Geophys. Research, 2010, 115, D00H30

[Ingle 1988] J. D. J. Ingle and S. R. Crouch, *Spectrochemical Analysis*, Prentice Hall, New Jersey (1988)

[ISCCP] `http://isccp.giss.nasa.gov/cloudtypes.html`

[JEM-EUSO Collaboration] JEM-EUSO Collaboration *JEM-EUSO Design Report* `http://jemeuso.riken.jp/en/index.html`, 2009.

[Jui et al. 2006] Charles C. H. Jui et al, *Results from the HiRes experiment* 2006 J. Phys.: Conf. Ser. 47 59-67 .

[Keilhauer 2001] B.A. Keilhauer,*Investigation of Atmospheric Effects on th Development of Extensive Air Showers and their Detection with the Pierre Auger Observatory* PhD Tesis, Universität Karlsruhe,Karlsruhe , Deutschland , (2001).

[Kohlhörster 1913] W. Kohlhörsterörster: Phys. Z. **14**, 1153 (1913).

[Kozai 1969] Kozai, Y., *Revised Values for Coefficients of Zonal Spherical Harmonics in the Geopotential*, SAO Special Report #295 (1969).

[Landau et al. 1953] L. Landau *The Collected Papers of L.D. Landau*, pp 586-589. Pergamon Press 1965.

[J. Larson & James R. Wertz] J. Larson & James R. Wertz (editors)*Space Mission Analysis and Design*, 2nd Ed.; Wiley , Microcosm Inc., 1992.

[Marion-Thorton] Stephen T. Thornton, Jerry B. Marion *Classical Dynamics of particles and systems*, Fifth Edition, Brooks Cole, USA (2004).

[Medina-Tanco 1999] G. Medina-Tanco *Ultra high-energy comic rays: probing the local Universe*,"Topics in cosmic-ray astrophysics" ed. M. A. DuVernois, Nova Scientific: New York, (1999).

[Medina Tanco 2001] G. Medina Tanco *Ultra-high energy cosmic rays: from GeV to ZeV.*Physics and Astrophysics of Ultra High Energy Cosmic Rays. M. Lemoine/ G. Sigl(ed.) (2001).

[Medina-Tanco et al. 2009] Medina-Tanco G. et al. for the JEM-EUSO Collaboration, *JEM-EUSO Science Objectives*,Proc. 31st ICRC, 2009.

[Medina-Tanco 2009] Medina-Tanco G. et al. for the JEM-EUSO Collaboration, *Studying individual UHECR sources with high statistics*,Proc. 31st ICRC, 2009.

[MERIS ATBD] *MERIS Level 2 Algorithms Theoretical Basis Document* Issue 4, European Space Agency, (2000).

[MERIS PH] *MERIS Product Handbook* Issue 2.1, European Space Agency, 2006.

[MERIS *web page*] `http://envisat.esa.int/instruments/meris/`

[Nagano & Watson 2000] M. Nagano, A.Watson. Review of Modern Physics Vol 72, 689 (2000).

[Naumov et al. 2010] C. Berat , S. Bottai , D. De Marco, S. Moreggia , D. Naumov, M. Pallavicini, R. Pesce , A. Petrolini , A. Stutz , E. Taddei , A. Thea, *Full simulation of space-based extensive air showers detectors with ESAF* Astroparticle Physics 33 (2010) 221–247.

[PAO 2004] Pierre Auger Collaboration, *Properties and performance of the prototype instrument for the Pierre Auger Observatory*Nuclear Instruments and Methods A523 (2004), 50.

[PAO 2007] Pierre Auger Collaboration,*Upper limit on the cosmic-ray photon fraction at EeV energies from the Pierre Auger Observatory* Astroparticle Physics 31 (2009), 399.

[PAO Anisotropy 2007] Pierre Auger Collaboration, *Anisotropy studies around the galactic centre at EeV energies with the Auger Observatory*,Astroparticle Physics 27 (2007), 244.

[PAO 2009] Pierre Auger Collaboration,*Limit on the diffuse flux of ultrahigh energy tau neutrinos with the surface detector of the Pierre Auger Observatory* Physical Review D79 (2009), 102001.

[Penndorf 1955] R. Penndorf, *Tables of the Refractive Index for Standard Air and the Rayleigh Scattering Coefficient for the Spectral Region between 0.2 and 20.0 μm and Their Application to Atmospheric Optics*, Journal of the Optical Society Of America Volume 47, Number 2, (1955).

[Pierog & Heck 2011] D. Heck and T. Pierog,*Extensive Air Shower Simulation with CORSIKA: A User's Guide Version 6.980* Karlsruher Institut für Technologie , 2011.

[Pierre Auger Collaboration 2007] Pierre Auger Collaboration, *Correlation of the highest energy cosmic rays with nearby extragalactic objects*,Science 318 (2007), 939.

[Pierre Auger Collaboration 2008] Pierre Auger Collaboration, *Observation of the Suppression of the Flux of Cosmic Rays above* $4\times10^{19}eV$,Physical Review Letters 101 (2008), 061101.

[Pierre Auger Collaboration 2008] Pierre Auger Collaboration, *Correlation of the highest-energy cosmic rays with the positions of nearby active galactic nuclei*, Astroparticle Physics 29 (2008), 188.

[Ryu, Kang & Biermann 1998] Ryu, D., Kang, H., Biermann, P. L.*Cosmic magnetic fields in large scale filaments and sheets* 1998, A A, 335, 19

[Saunders et al.] W.Saunders, W.J.Sutherland, S.J.Maddox, O.Keeble, S.J.Oliver, M.Rowan-Robinson, R.G.McMahon, G.P.Efstathiou, H.Tadros, S.D.M.White, C.S.Frenk, A. Carraminana, M.R.S.Hawkins,*The PSCz Catalogue*,Mon.Not.Roy.Astron.Soc. 317 (2000) 55 `arXiv:astro-ph/0001117v2`

[Schüssler et al. 2009] F. Schüssler, Pierre Auger Collaboration, *Measurement of the cosmic ray energy spectrum above 1018 eV with the Pierre Auger Observatory*, 31^{st} International Cosmic Ray Conference Proceedings, 2009.

[Sciutto 1997] S. J. Sciutto, *AIRES: A minimum document*, Auger technical note GAP-97-029 (1997).

[Stephens et al. 2002] Stephens, G. L.,et al. *The CloudSat mission and the A-TRAIN: A new dimension of space-based observations of clouds and precipitation* . Bull. Amer. Meteor. Soc., 83, pp 1771–1790 (2002).

[Supanitsky 2007] Alberto D. Supanitsky,*Detectores de superfice y la composición Química de los Rayos Cósmicos* PhD Tesis, Universidad de Buenos Aires,Bs.As., Argentina, (2007).

[Takahashi 2009] Y. Takahashi, New Journal of Physics, Vol. 11, N. 065009, 2009.

[Takeda et al. 1999] M. Takeda et al. , *Small-Scale Anisotropy of Cosmic Rays Above* $10^{19}eV$ *Observed with the Akeno Giant Air Shower Array*, Astrophys. J. 522 (1999) 225-237

[Takeda et al. 1998] M.Takeda, N.Hayashida, K.Honda, N.Inoue, K.Kadota, F.Kakimoto, K.Kamata, S.Kawaguchi, Y.Kawasaki, N.Kawasumi, E.Kusano, Y.Matsubara, K.Murakami, M.Nagano, D.Nishikawa, H.Ohoka, S.Osone, N.Sakaki, M.Sasaki, K.Shinozaki, N.Souma, M.Teshima, R.Torii, I.Tsushima,

Y.Uchihori, T.Yamamoto, S.Yoshida and H.Yoshii *Recent results from the AGASA experiment*, Proc. of 19th Texas Symposium (Paris) 1998.

[Telescope Array 2009] J.N. Matthews, C.C.H. Jui , F. Kakimoto, S.Ogio, H. Sagawa, S.B. Thomas for the Telescope Array Collaboration, *Overview of the Telescope Array Experiment*, 31^{st} International Cosmic Ray Conference, Łódź 2009

[Tiffenberg 2009] Javier Tiffenberg for the Pierre Auger Collaboration, *Limits on the diffuse flux of ultra high energy neutrinos set using the Pierre Auger Observatory*,31^{st} International Cosmic Ray Conference, Łódź 2009

[van de Hulst 1957] H.C. van de Hulst, *Light Scattering by small particles*,Dover Publications Inc. New York (1957).

[Vaughan et al. 2004] Vaughan, M., S. Young, D. Winker, K. Powell, A. Omar, Z. Liu, Y. Hu, and C. Hostetler,*Fully automated analysis of space-based lidar data: An overview of the CALIPSO retrieval algorithms and data products. Laser Radar Techniquesfor Atmospheric Sensing*, U. N. Singh, Ed., International Society for Optical Engineering (SPIE Proceedings, Vol. 5575), 16–30, (2004).

[Wahlberg 2009] Hernan Wahlberg,Pierre Auger Collaboration, *Study of the nuclear mass composition of UHECR with the surface detectors of the Pierre Auger Observatory* , 31^{st} International Cosmic Ray Conference Proceedings, 2009.

[Waquet et al. 2009] F. Waquet, J. Riedi, L. C. Labonnote, P. Goloub, *Aerosol Remote Sensing over Clouds Using A-Train Observations* , Journal Of The Atmospheric Sciences Vol 66 (2009).

[Wieler 1982] Weiler, T. J. Phys. Rev. Lett., 49, 234, 1982

[Yoshida et al. 1995] S. Yoshida et al. , *The cosmic ray energy spectrum above* $3 \times 10^{18} eV$ *measured by the Akeno Giant Air Shower Array*, Astroparticle Physics 3 (1995) 105-123

[Zatsepin & Ku'smin 1966] G.T. Zatsepin, V.A. Kuz'min, *Upper Limit of the Spectrum of Cosmic Rays*, Journal of Experimental and Theoretical Physics Letters 4: 78–80 (1966).